ACCURACY OF HEC-RAS TO CALCULATE FLOW DEPTHS AND TOTAL ENERGY LOSS WITH AND WITHOUT BENDWAY WEIRS IN A MEANDER BEND

Prepared for

U.S. Department of the Interior
Bureau of Reclamation
Albuquerque Area Office
555 Broadway N.E., Suite 100
Albuquerque, New Mexico 87102-2352

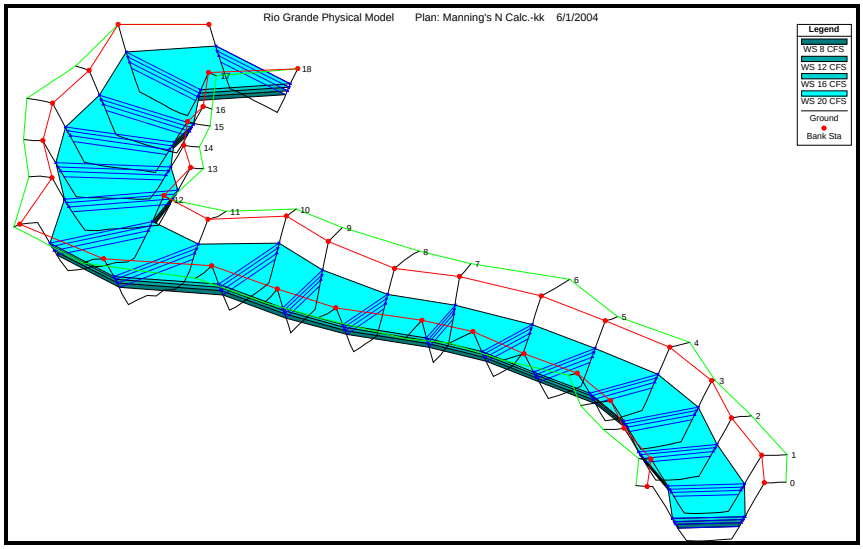

December 2005

Colorado State University
Daryl B. Simons Building *at the*
Engineering Research Center
Fort Collins, Colorado 80523

ACCURACY OF HEC-RAS TO CALCULATE FLOW DEPTHS AND TOTAL ENERGY LOSS WITH AND WITHOUT BENDWAY WEIRS IN A MEANDER BEND

Prepared for

U.S. Department of the Interior
Bureau of Reclamation
Albuquerque Area Office
555 Broadway N.E., Suite 100
Albuquerque, New Mexico 87102-2352

Prepared by

Kristin E. Kasper, Christopher I. Thornton,
Steven R. Abt, Michael D. Robeson,
and Chester C. Watson

December 2005

Colorado State University
Daryl B. Simons Building *at the*
Engineering Research Center
Fort Collins, Colorado 80523

EXECUTIVE SUMMARY

River systems are interconnected waterways that often change to reach a state of dynamic equilibrium. Dynamic equilibrium is a fragile balance between flow conditions, sediment transport, and environmental habitat in a river system. To study river systems in detail, complex hydraulic models have been developed. Hydraulic models calculate flow depths and energy loss through a river system and are defined as 1-, 2-, or 3-dimensional (1-D, 2-D, or 3-D, respectively) models. Differences between each model type depend on assumptions used to build the model. A 1-D model assumes the primary component of a 3-D velocity profile is along the x-coordinate axis. Therefore, the velocity components along the y- and z-coordinate axes are assumed insignificant.

In 1-D analysis, Hydrologic Engineering Center's River Analysis System (HEC-RAS) is a common hydraulic model used to study flow depths and total energy loss along a study reach of a river system. HEC-RAS is a 1-D model that performs calculations for steady or unsteady flow in gradually-varied or rapidly-varied flow analysis. Even though HEC-RAS is a 1-D hydraulic model, it is commonly used to model flow patterns where the velocity along the y- or z-coordinate axes are significant. For instance, HEC-RAS is used to study meander bends. Meander bends are undulating segments in a river system where the dominant direction of velocity is not necessarily along the x-coordinate axis. An added level of complexity develops when bank-stabilization features such as bendway weirs are added to a HEC-RAS model. Bendway weirs are bank-stabilization features

built of local rock material. Bendway weirs are constructed along the outer bank of a meander bend in order to reduce bank erosion by directing high velocities along the outer bank to the center of the channel. While protecting the stream bank, bendway weirs support viable aquatic habitats and riparian vegetation along a meander bend.

Since HEC-RAS is often used to model 3-D velocity profiles with and without bendway weirs, research needs to be completed to determine the accuracy of HEC-RAS. Included in this study was an analysis to determine the accuracy of HEC-RAS to model flow depths and total energy loss along a meander bend with or without bendway weirs and a methodology to best estimate total energy loss given HEC-RAS output.

A study was conducted using HEC-RAS to research hydraulic characteristics of meander bends in the physical model with and without bendway weirs. Objectives of this research were to: 1) determine feasibility of HEC-RAS to sufficiently calculate flow depths and total energy loss through meander bends without bendway weirs; 2) determine feasibility of HEC-RAS to sufficiently calculate flow depths and total energy loss through meander bends with bendway weirs; and 3) outline appropriate methodology in order to use HEC-RAS to calculate flow depths and total energy loss through a meander bend with and without bendway weirs.

TABLE OF CONTENTS

LIST OF FIGURES

LIST OF TABLES

LIST OF SYMBOLS AND ABBREVIATIONS

Symbols

A = cross-sectional area normal to the direction of flow (ft^2)

A_1 = cross-sectional area normal to the direction of flow at the downstream cross section (ft^2)

A_2 = cross-sectional area normal to the direction of flow at the upstream cross section (ft^2)

α = kinetic energy correction coefficient

α_1 = kinetic energy correction coefficient at the downstream cross section

α_2 = kinetic energy correction coefficient at the upstream cross section

b = channel width (ft)

BW = base width of channel (L)

C = coefficient of loss

C_c = coefficient of contraction

C_e = coefficient of expansion

ρ = density of water (M/L^3)

Δh = difference in pressure of fluid flowing (ft)

Δx = distance along the centerline of the channel between cross sections (ft)

EGL_{CALC} = energy grade line (ft/ft)

Φ = unit conversion (Eng = 1.486 and SI = 1.000)

f_c = coefficient of curve resistance

Fr = Froude number

g = acceleration of gravity (ft/s^2)

h_b = minor loss due to bend (ft)

h_{BEND} = energy loss due to bend (ft)

$\bar{h}_{BEND}$ = cross-sectional average minor loss due to meander bend (ft)

$\bar{h}_{BEND-TOTAL}$ = average minor loss due to the meander bend through the bend (ft)

h_c = minor loss due to channel contraction at a cross section (ft)

h_e = minor loss due to channel expansion at a cross section (ft)

h_f = energy loss due to friction (ft)

h_{Sf} = average friction loss (ft)

$h_{Sf\,8cfs}$ = average friction loss at a discharge of 8 cfs in the physical model

$h_{Sf\,12cfs}$ = average friction loss at a discharge of 12 cfs in the physical model

$h_{Sf\,16cfs}$ = average friction loss at a discharge of 16 cfs in the physical model

$\bar{h}_{Sf}$ = cross-sectional average, average friction loss (ft)

$\bar{h}_{Sf-TOTAL}$ = average friction loss through the meander bend (ft)

h_t = total energy loss between adjacent cross sections (ft)

h_T = total energy loss through a meander bend (ft)

$\bar{h}_t$ = cross-sectional average total energy loss (ft)

$\bar{h}_T$ = average total energy loss through a meander bend (ft)

H = total energy at each cross section (ft)

$H_{8\,cfs}$ = total energy at each cross section when the discharge is 8 cfs in the physical model (ft)

$H_{12\,cfs}$ = total energy at each cross section when the discharge is 12 cfs in the physical model (ft)

$H_{16\ cfs}$ = total energy at each cross section when the discharge is 16 cfs in the physical model (ft)

H_1 = total energy at the downstream cross section (ft)

H_2 = total energy at the upstream cross section (ft)

H_D = hydraulic depth (ft)

θ = deviation angle of the curve

θ_w = orientation angle

K = channel conveyance (ft)

K_1 = channel conveyance at the downstream cross section (ft)

K_2 = channel conveyance at the upstream cross section (ft)

K_b = coefficient of curve resistance

L_{arc} = length of arc from center of the bendway weir to center of the bendway weir along the design flow water surface (ft)

L_b = length of channel bend along center line (L)

L_{cw} = length of crest along bendway weir (ft)

L_r = bendway-weir length ratio (ft)

L_w = total length of bendway weir (ft)

μ = dynamic viscosity of water (M-T/L^2)

n = roughness coefficient

$n_{\ 8\ cfs}$ = roughness coefficient at a discharge of 8 cfs in the physical model

$n_{\ 12\ cfs}$ = roughness coefficient at a discharge of 12 cfs in the physical model

$n_{\ 16\ cfs}$ = roughness coefficient at a discharge of 16 cfs in the physical model

n_{EFF} = effective roughness coefficient

P = wetted perimeter (ft)

π = dimensionless term

Q = discharge (cfs)

Q_1 = discharge at the downstream cross section (cfs)

Q_2 = discharge at the upstream cross section (cfs)

r = inner radius (ft)

r_c = radius of curvature (ft)

R = hydraulic radius (ft)

Re = Reynold's number

S = spacing ratio

S_o = bed slope (ft/ft)

S_f = friction slope (ft/ft)

$S_{f\,MANNING}$ = friction slope calculated using a version of Manning's equation (ft/ft)

$\overline{S}_f$ = average friction slope between two adjacent cross sections (ft/ft)

$\overline{S}_{f-CONV}$ = average friction slope using the average conveyance method (ft/ft)

Σ = summation

$\Sigma\Delta°$ = summation of deflection angles

TW = top width of channel (ft)

$\overline{TW}$ = cross-sectional averaged top width (ft)

υ = kinematic viscosity of a fluid (ft^2/s)

$\overline{v}$ = average velocity at a cross section (ft/s)

$\overline{v}_{8cfs}$ = average velocity at a cross section when the discharge is 8 cfs in the physical model (ft/s)

$\overline{v}_{12cfs}$ = average velocity at a cross section when the discharge is 12 cfs in the physical model (ft/s)

$\overline{v}_{16cfs}$ = average velocity at a cross section when the discharge is 16 cfs in the physical model (ft/s)

$\bar{v}_1$ = average velocity at the downstream cross section (ft/s)

$\bar{v}_2$ = average velocity at the upstream cross section (ft/s)

w = top width of a cross section along the water surface (ft)

W_{bw} = base width of bendway weir (ft)

W_{cw} = crest width of bendway weir (ft)

WSE = water-surface elevation along the cross section (ft)

WSE_2 = water-surface elevation at the upstream cross section (ft)

XS_{TOTAL} = number of significant cross section used in analysis

y = flow depth at a cross section (ft)

$\bar{y}$ = cross-sectional average flow depth (ft)

y_{PG} = flow depth at Piezometer D using a track mounted point gage (ft)

$y_{8\ cfs}$ = flow depth at a discharge of 8 cfs in the physical model (ft)

$y_{12\ cfs}$ = flow depth at a discharge of 12 cfs in the physical model (ft)

$y_{16\ cfs}$ = flow depth at a discharge of 16 cfs in the physical model (ft)

y_1 = flow depth at the downstream cross section (ft)

y_2 = flow depth at the upstream cross section (ft)

$\bar{y}_{8cfs}$ = cross-sectional average flow depth at a discharge of 8 cfs in the physical model (ft)

$\bar{y}_{12cfs}$ = cross-sectional average flow depth at a discharge of 12 cfs in the physical model (ft)

$\bar{y}_{16cfs}$ = cross-sectional average flow depth at a discharge of 16 cfs in the physical model (ft)

z = bed elevation at a cross section (ft)

z_1 = bed elevation at the downstream cross section (ft)

z_2 = bed elevation at the upstream cross section (ft)

z_D = surveyed bed elevation at Piezometer D (ft)

Abbreviations

°	degree(s)
%	percent
®	registered trademark
1-D	1-dimensional
2-D	2-dimensional
3-D	3-dimensional
cfs	cubic feet per second
EGL	energy grade line
Eng	English
D/S	downstream
ft	foot or feet
ft/ft	feet per foot
ft/s	feet per second
ft/s^2	feet per second squared
ft^2	squared feet
HEC-RAS	Hydrologic Engineering Center's River Analysis System
in.	inch(es)
SI	Systeme Internationale d'Unites (International System of Units)
U/S	upstream

USACE	United States Army Corps of Engineers
USBR	United States Bureau of Reclamation
USGS	United States Geological Survey
x, y, z	coordinate axes
XS	cross section(s)

CHAPTER 1 INTRODUCTION

1.1 GENERAL BACKGROUND

River systems are interconnected waterways that often change to reach a state of dynamic equilibrium. Dynamic equilibrium is a fragile balance between flow conditions, sediment transport, and environmental habitat in a river system. To study river systems in detail, complex hydraulic models have been developed. Hydraulic models calculate flow depths and energy loss through a river system and are defined as 1-, 2-, or 3-dimensional (1-D, 2-D, or 3-D, respectively) models. Differences between each model type depend on assumptions used to build the model. A 1-D model assumes the primary component of a 3-D velocity profile is along the x-coordinate axis. Therefore, the velocity components along the y- and z-coordinate axes are assumed insignificant. Positive velocity components along the y- and z-coordinate axes refer to lateral flow to the left bank looking downstream and the upward vertical direction, respectively, while the positive velocity component along the x-coordinate axis refers to the flow direction. In 2-D and 3-D hydraulic models, the 1-dimensional assumption for the y- and z-coordinate axes does not hold true.

In 1-D analysis, Hydrologic Engineering Center's River Analysis System (HEC-RAS) is a common hydraulic model used to study flow depths and total energy loss along a study reach of a river system. HEC-RAS is a 1-D model that performs calculations for

steady or unsteady flow in gradually-varied or rapidly-varied flow analysis. Even though HEC-RAS is a 1-D hydraulic model, it is commonly used to model flow patterns where the velocity along the y- or z-coordinate axes are significant. For instance, HEC-RAS is used to study meander bends. Meander bends are undulating segments in a river system where the dominant direction of velocity is not necessarily along the x-coordinate axis. An added level of complexity develops when bank-stabilization features such as bendway weirs are added to a HEC-RAS model. Bendway weirs are bank-stabilization features built of local rock material. Bendway weirs are constructed along the outer bank of a meander bend in order to reduce bank erosion by directing high velocities along the outer bank to the center of the channel. While protecting the stream bank, bendway weirs support viable aquatic habitats and riparian vegetation along a meander bend.

Since HEC-RAS is often used to model 3-D velocity profiles with and without bendway weirs, research needs to be completed to determine the accuracy of HEC-RAS. Included in this study was an analysis to determine the accuracy of HEC-RAS to model flow depths and total energy loss along a meander bend with or without bendway weirs and a methodology to best estimate total energy loss given HEC-RAS output.

1.2 PROJECT BACKGROUND

Managed by the United States Bureau of Reclamation (USBR), the Middle Rio Grande project has been the primary focus for channel maintenance in central New Mexico. The study reach is a 29-mile stretch of the Rio Grande extending from the Cochiti Dam to Bernalillo, New Mexico. In an attempt to deter bank erosion, channel migration, and habitat degradation, the USBR desires to construct bendway weirs along

the outer bank of meander bends in the Middle Rio Grande. In order to design an effective bendway weir for an individual meander bend, a physical model of the Middle Rio Grande was built in the Hydromachinery Laboratory at the Engineering Research Center, Colorado State University. The physical model of the Middle Rio Grande was designed at a 1:12 Froude scale and contains undistorted meander bends representative of meander bends in the Middle Rio Grande. In order to study flow depths and total energy loss along the physical model, a HEC-RAS model was built to numerically represent the physical model.

1.3 RESEARCH OBJECTIVES AND SCOPE

A study was conducted using HEC-RAS to research hydraulic characteristics of meander bends in the physical model with and without bendway weirs. Objectives of this research were to:

1. Determine feasibility of HEC-RAS to sufficiently calculate flow depths and total energy loss through meander bends without bendway weirs.
2. Determine feasibility of HEC-RAS to sufficiently calculate flow depths and total energy loss through meander bends with bendway weirs.
3. Outline appropriate methodology in order to use HEC-RAS to calculate flow depths and total energy loss through a meander bend with and without bendway weirs.

To achieve these objectives, the following scope of research was defined:

1. Conduct a literature review pertaining to fundamental equations used in hydraulic analysis.

2. Conduct a literature review obtaining reference material on previous HEC-RAS studies involving meander bends.
3. Conduct a literature review to understand principles and methodology used in HEC-RAS.
4. Conduct a literature review to note meander bend characteristics and flow patterns.
5. Conduct a literature review obtaining reference material on calculating minor loss due to meander bends.
6. Collect data required to build HEC-RAS models.
7. Collect all necessary physical model measurements to determine accuracy of HEC-RAS models.
8. Build HEC-RAS models that represent the physical model with and without bendway weirs.
9. Analyze various HEC-RAS models to meet Objectives 1 through 3.
10. Present methodology, if feasible, to accurately calculate flow depths and total energy loss through meander bends with or without bendway weirs in HEC-RAS.

CHAPTER 2 LITERATURE REVIEW

2.1 HEC-RAS

HEC-RAS is one of the most widespread models used to calculate water-surface profiles and energy grade lines in 1-D, steady-state, gradually-varied flow analysis. In 1-D, steady-state, gradually-varied flow analysis, the following assumptions are made:

1. Dominant velocity is in the flow direction;
2. Hydraulic characteristics of flow remain constant for the time interval under consideration; and
3. Streamlines are practically parallel and, therefore, hydrostatic pressure distribution prevails over channel section (Chow, 1959).

Equations illustrating the stated assumptions are discussed in Section 2.2.

2.2 FUNDAMENTAL HYDRAULIC EQUATIONS

Fundamental hydraulic equations that govern 1-D, steady-state, gradually-varied flow analysis include the continuity equation, energy equation, and flow resistance equation. These equations, in addition to the Froude number and other important hydraulic concepts, are noted in the succeeding sections.

2.2.1 Continuity Equation

The continuity equation describes a discharge as constant and continuous over the period of time in consideration (Chow, 1959). The concept of continuity is shown in Equation 2.1:

$$Q = \bar{v}_1 A_1 = \bar{v}_2 A_2 \qquad \textbf{Equation 2.1}$$

where:

A_1 = cross-sectional area normal to the direction of flow at the downstream cross section (ft^2);

A_2 = cross-sectional area normal to the direction of flow at the upstream cross section (ft^2);

Q = discharge (cfs);

$\bar{v}_1$ = average velocity at the downstream cross section (ft/s); and

$\bar{v}_2$ = average velocity at the upstream cross section (ft/s).

Using the continuity equation, the average velocity is expressed in terms of discharge and cross-sectional area, which is shown in Equation 2.2:

$$\bar{v} = \frac{Q}{A} \qquad \textbf{Equation 2.2}$$

where:

A = cross-sectional area normal to the direction of flow (ft^2);

Q = discharge (cfs); and

$\bar{v}$ = average velocity (ft/s).

2.2.2 Energy Equation

Total energy at any point along an open-channel system can be defined as total head in feet of water (Chow, 1959). Total head of water is calculated using the energy equation. The energy equation is used to calculate the total head of water as the summation of the bed elevation, average flow depth, and the velocity head at a cross section, which is illustrated in Equation 2.3:

$$H = z + y + \frac{\alpha \bar{v}^2}{2g} \qquad \textbf{Equation 2.3}$$

where:

α = kinetic energy correction coefficient;

g = acceleration of gravity (ft/s^2);

H = total head of water (ft);

$\bar{v}$ = average velocity at a cross section (ft/s);

y = flow depth at a cross section (ft); and

z = bed elevation at a cross section (ft).

The kinetic energy correction coefficient is multiplied by the velocity head to better estimate the velocity head at a cross section. True velocity head at a cross section is generally higher than the estimated velocity head using the average velocity at a cross section. Kinetic energy correction coefficient aids in correcting the difference where values typically range between 1.03 and 1.36 for fairly straight, prismatic channels (Chow, 1959).

2.2.3 Flow Resistance Equation

The flow resistance equation uses a form of Manning's equation to define an equation that applies average roughness to the wetted perimeter of a cross section (United States Army Corps of Engineers (USACE), 2001a). The flow resistance equation is shown in Equation 2.4 based on a form of Manning's equation:

$$Q = KS_f^{1/2} \qquad \textbf{Equation 2.4}$$

where:

K = channel conveyance (ft);

Q = discharge (cfs); and

S_f = friction slope (ft/ft).

Conveyance at a cross section is obtained using Equation 2.5:

$$K = \frac{\Phi}{n} AR^{2/3} = \frac{\Phi}{n} A\left(\frac{A}{P}\right)^{2/3} \qquad \textbf{Equation 2.5}$$

where:

A = cross-sectional area normal to the direction of flow (ft^2);

Φ = unit conversion (Eng = 1.486 and SI = 1.000);

K = channel conveyance (ft);

n = roughness coefficient;

P = wetted perimeter (ft); and

R = hydraulic radius (ft).

Cross-sectional area and wetted perimeter are a function of channel geometry. If the cross section is rectangular, then Equation 2.6 and Equation 2.7 apply for cross-sectional area and wetted perimeter, respectively:

$$A = yw \qquad \textbf{Equation 2.6}$$

$$P = 2y + w \qquad \textbf{Equation 2.7}$$

where:

A = cross-sectional area normal to the direction of flow (ft^2);

P = wetted perimeter (ft);

w = top width of a cross section along the water surface (ft); and

y = flow depth at a cross section (ft).

Figure 2.1 illustrates the variables used in Equation 2.6 and Equation 2.7 for a rectangular cross section.

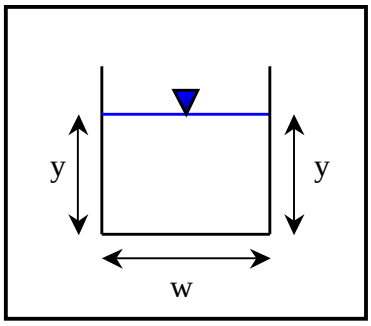

Figure 2.1. Variables Used to Calculate *A* and *P*

2.2.4 Energy Loss in an Open-channel System

Energy loss in an open channel system is defined as energy loss along a channel reach due to friction, contractions, expansions, eddies, spiral, and secondary currents. In 1-D, steady-state, gradually-varied flow analysis, energy loss is assumed to be due to friction, contraction, and expansion loss.

2.2.4.1 Friction Loss

Friction loss is termed as energy loss along a channel reach due to roughness of the channel boundary. Friction loss is calculated by multiplying average friction slope by the distance along the channel. Equation 2.8 illustrates the friction loss equation:

$$h_f = \overline{S}_f \Delta x \qquad \textbf{Equation 2.8}$$

where:

h_f = energy loss due to friction (ft);

$\overline{S}_f$ = average friction slope between two adjacent cross sections (ft/ft); and

Δx = incremental channel length (ft).

Average friction slope is calculated by rearranging Equation 2.4. Equation 2.9 presents the equation for average friction slope:

$$S_f = \left(\frac{Q}{K}\right)^2 \qquad \textbf{Equation 2.9}$$

where:

K = channel conveyance (ft);

Q = discharge (cfs); and

S_f = friction slope (ft/ft).

A statistical technique known as the average conveyance method is used to calculate the average friction slope between adjacent cross sections. The average conveyance method is illustrated by Equation 2.10:

$$\overline{S}_f = \left(\frac{Q_1 + Q_2}{K_1 + K_2}\right)^2 \qquad \textbf{Equation 2.10}$$

where:

K_1 = channel conveyance at the downstream cross section (ft);

K_2 = channel conveyance at the upstream cross section (ft);

Q_1 = discharge at the downstream cross section (cfs);

Q_2 = discharge at the upstream cross section (cfs); and

$\overline{S}_f$ = average friction slope between two adjacent cross sections (ft/ft).

Average conveyance method is the default method in HEC-RAS to calculate average friction slope (USACE, 2001a).

2.2.4.2 Minor Loss

Expansion and contraction losses are collectively known as minor loss along a reach in a 1-D, steady-state, gradually-varied flow analysis. Expansion and contraction minor loss is related to the energy loss due to changes in cross-sectional shape along the reach. For instance, when water flows downstream, a reach may expand or contract. As the reach expands or contracts, energy loss occurs along a study reach. Figure 2.2 illustrates a planform view of a contraction reach and an expansion reach.

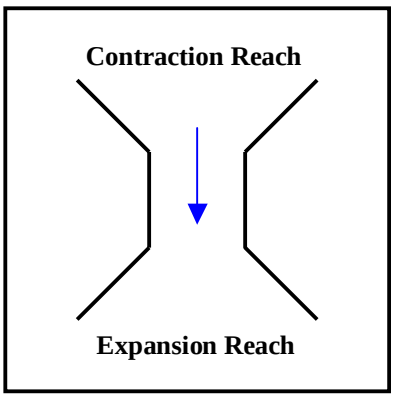

Figure 2.2. Planform View of a Contraction Reach and Expansion Reach

Energy losses due to expansion and contractions along a reach are accounted for through appropriate coefficients. Once an appropriate coefficient is determined, the coefficient is multiplied by the velocity head in order to calculate the energy loss. Equation 2.11 and Equation 2.12 present equations for calculating minor loss due to expansions or contractions, respectively:

$$h_e = C_e\left(\frac{\alpha_2 \bar{v}_2^2}{2g} - \frac{\alpha_1 \bar{v}_1^2}{2g}\right) \qquad \textbf{Equation 2.11}$$

where:

α_1 = kinetic energy correction coefficient at the downstream cross section;

α_2 = kinetic energy correction coefficient at the upstream cross section;

C_e = coefficient of expansion;

g = acceleration of gravity (ft/s^2);

h_e = minor loss due to channel expansion at a cross section (ft);

$\bar{v}_1$ = average velocity at the downstream cross section (ft/s); and

$\bar{v}_2$ = average velocity at the upstream cross section (ft/s).

$$h_c = C_c\left(\frac{\alpha_2 \bar{v}_2^2}{2g} - \frac{\alpha_1 \bar{v}_1^2}{2g}\right) \qquad \textbf{Equation 2.12}$$

where:

α_1 = kinetic energy correction coefficient at the downstream cross section;

α_2 = kinetic energy correction coefficient at the upstream cross section;

C_c = coefficient of contraction;

g = acceleration of gravity (ft/s^2);

h_c = minor loss due to channel contraction at a cross section (ft);

$\bar{v}_1$ = average velocity at the downstream cross section (ft/s); and

$\bar{v}_2$ = average velocity at the upstream cross section (ft/s).

Typical values for the coefficients of expansion and contraction in a subcritical flow regime are given in Table 2.1, which was published by the USACE in the *HEC-RAS River Analysis System Users Manual Version 3.0* (USACE, 2001b).

Table 2.1. Contraction and Expansion Coefficients (USACE, 2001b)

Subcritical Flow Contraction and Expansion Coefficients	Contraction	Expansion
No Transition Loss Computed	0.00	0.00
Gradual Transitions	0.10	0.30
Typical Bridge Sections	0.30	0.50
Abrupt Transitions	0.60	0.80

2.2.5 Froude Number

In 1-D, steady-state, gradually-varied flow analysis, it is important to note the effect of gravity on the state of the flow. Effect of gravity on the state of flow is represented by a ratio of inertial forces to gravitational forces (Chow, 1959). The ratio of inertial forces to gravitational forces has been termed Froude number and is presented in Equation 2.13:

$$Fr = \frac{\bar{v}}{\sqrt{gH_D}} \qquad \textbf{Equation 2.13}$$

where:

Fr = Froude number;

g = acceleration of gravity (ft/s^2);

H_D = hydraulic depth (ft); and

$\bar{v}$ = average velocity at a cross section (ft/s).

Hydraulic depth is defined in Equation 2.14:

$$H_D = \frac{A}{w} \qquad \textbf{Equation 2.14}$$

where:

A = cross-sectional area normal to the direction of flow (ft^2);

H_D = hydraulic depth (ft); and

w = top width of a cross section along the water surface (ft).

For rectangular cross sections, hydraulic depth is assumed equal to flow depth. When the Froude number is equal to one, the flow is termed critical flow. Critical flow is the condition where elementary waves can no longer propagate upstream (Bitner, 2003). If the Froude number is greater than one, the flow is termed supercritical flow. Supercritical flow is characterized by high velocities where inertial forces become dominant at a cross section. If the Froude number is less than one, then the flow is termed subcritical flow. Subcritical flow is characterized by low velocities and is dominated by gravitational forces (Chow, 1959).

2.3 STANDARD STEP METHOD

Based on the concept of conservation of energy, the standard step method uses fundamental hydraulic equations to iteratively calculate water-surface profiles and energy grade lines. Conservation of energy states that "within some problem domain, the amount of energy remains constant and energy is neither created nor destroyed. Energy can be converted from one form to another but the total energy within the domain remains fixed" (Benson, 2004). Iteratively, the standard step method applies conservation of energy using the energy equation to calculate water-surface elevations

and energy grade lines along the reach. For the purpose of the standard step, the energy equation is written as:

$$y_2 + z_2 + \frac{\alpha_2 \bar{v}_2^{\,2}}{2g} = y_1 + z_1 + \frac{\alpha_1 \bar{v}_1^{\,2}}{2g} + h_t \qquad \textbf{Equation 2.15}$$

where:

α_1 = kinetic energy coefficient at the downstream cross section;

α_2 = kinetic energy coefficient at the upstream cross section;

g = acceleration of gravity (ft/s^2);

h_t = total energy loss between adjacent cross sections (ft);

$\bar{v}_1$ = average velocity at the downstream cross section (ft/s);

$\bar{v}_2$ = average velocity at the upstream cross section (ft/s);

y_1 = flow depth at the downstream cross section (ft);

y_2 = flow depth at the upstream cross section (ft);

z_1 = bed elevation at the downstream cross section (ft); and

z_2 = bed elevation at the upstream cross section (ft);

Total energy loss is equal to Equation 2.16 between adjacent cross sections:

$$h_t = h_f + h_e + h_c \qquad \textbf{Equation 2.16}$$

where:

h_c = minor loss due to channel contraction (ft);

h_e = minor loss due to channel expansion (ft);

h_f = energy loss due to friction (ft); and

h_t = total energy loss between adjacent cross sections (ft).

Figure 2.3 illustrates the backwater computation between adjacent cross sections using the energy equation where Q denotes discharge, EGL denotes energy grade line, and XS denotes cross section.

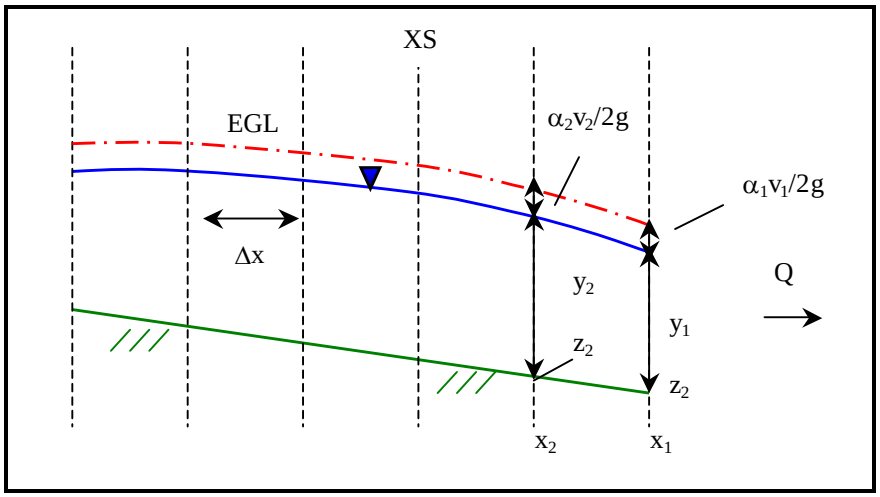

Figure 2.3. Standard Step Method

2.3.1 Standard Step Method Algorithm

The standard step method is one of the coded algorithms in HEC-RAS. If the flow is subcritical, HEC-RAS iteratively calculates a water-surface profile and energy grade line beginning with the most downstream cross section. If the flow is supercritical, HEC-RAS calculates a water-surface profile and energy grade line beginning with the most upstream cross section. An outline of the standard step method used in HEC-RAS is obtained from the *HEC-RAS River Analysis System Hydraulic Reference Manual* and is stated below (USACE, 2001a):

1. Assume a water-surface elevation at an upstream cross section (or downstream cross section if a supercritical profile is being calculated).

2. Based on the assumed water-surface elevation, determine the corresponding *K* and *v*.

3. With values from Step 2, compute $\overline{S}_f$ and solve Equation 2.16 for h_t. $\overline{S}_f$ is calculated using the average conveyance method, the default method in HEC-RAS.

4. With values from Step 2 and Step 3, solve Equation 2.15 for water-surface elevation at the upstream cross section. The water-surface elevation at the upstream cross section is obtained by rearranging Equation 2.15 to Equation 2.17:

$$WSE_2 = y_2 + z_2 = y_1 + z_1 + \left(\frac{\alpha_1 \overline{v}_1^2}{2g} - \frac{\alpha_2 \overline{v}_2^2}{2g} \right) + h_t \qquad \textbf{Equation 2.17}$$

where:

α_1 = kinetic energy coefficient at downstream cross section;

α_2 = kinetic energy coefficient at upstream cross section;

g = acceleration of gravity (ft/s^2);

h_t = total energy loss between adjacent cross sections (ft);

$\overline{v}_1$ = average velocity at downstream cross section (ft/s);

$\overline{v}_2$ = average velocity at upstream cross section (ft/s);

WSE_2 = water-surface elevation at the upstream cross section (ft);

y_1 = flow depth at downstream cross section (ft);

y_2 = flow depth at upstream cross section (ft);

z_1 = bed elevation at downstream cross section (ft); and

z_2 = bed elevation at upstream cross section (ft).

5. Compare the computed value of the water-surface elevation at the upstream cross section with the value assumed in Step 1, repeat Step 1 through Step 5 until the values agree to within 0.01 ft, or a user-defined tolerance.

In order to start the iterative procedure, a known boundary condition is entered by the user. A boundary condition must be established at the most downstream cross section for a subcritical flow profile and at the most upstream cross section for a supercritical flow profile. Four options are presented in HEC-RAS to establish one boundary condition. The four boundary condition options include the following:

1. known water-surface elevation;
2. critical depth;
3. normal depth; and
4. rating curve.

Critical depth is defined as the flow depth when $Fr = 1$. Normal depth is defined as the depth corresponding to uniform flow (Chow, 1959). Normal depth is calculated after the user enters the bed slope downstream of the study reach. The bed slope is equal to the energy slope for normal depth and, therefore, used in the flow resistance equation to calculate normal depth (USACE, 2001a).

2.4 HEC-RAS FORMAT

A brief discussion is needed to define terminology in HEC-RAS for a steady-state, gradually-varied flow analysis. In this analysis, HEC-RAS Version 3.1.2 was used. A project refers to the HEC-RAS model and encompasses ns, geometry data files, and steady flow files for a particular river system (USACE, 2001b). A project is broken

down into various plans. Each plan represents a "specific set of geometric data and flow data" (USACE, 2001a). Channel geometry data such as survey information, channel lengths, Manning's *n*-values, contraction coefficients, and expansion coefficients are entered into a geometry file. Discharges and boundary conditions are entered into a steady flow file. Once the appropriate information is entered in the geometry file and steady flow file, the defined plan is run in a steady flow analysis. A diagram illustrating the HEC-RAS outline is shown in Figure 2.4.

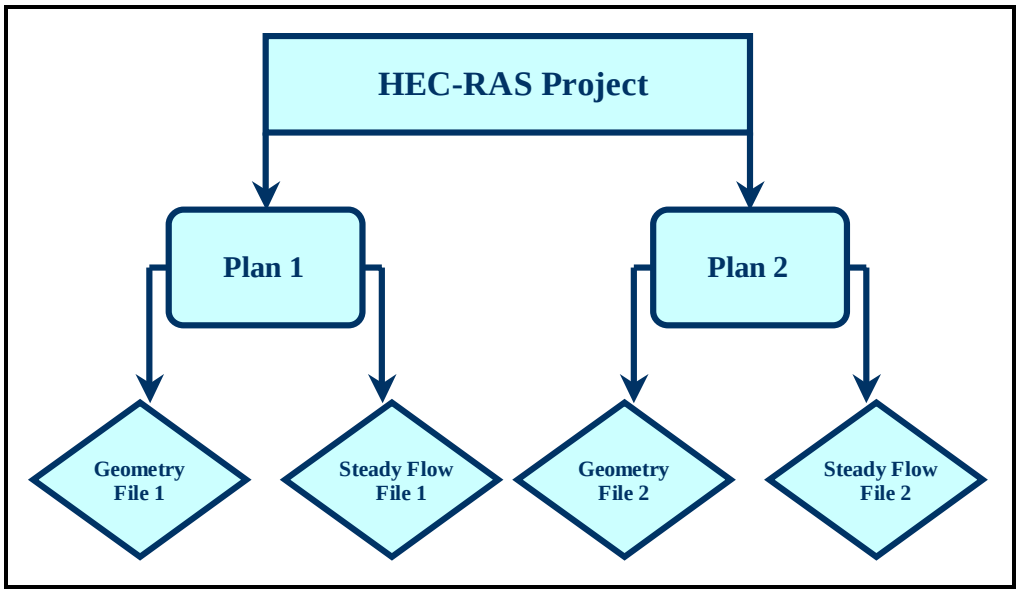

Figure 2.4. HEC-RAS Format

2.5 PREVIOUS STUDIES ON CALCULATING WATER-SURFACE ELEVATIONS IN MEANDER BENDS WITH BENDWAY WEIRS

Previous studies have been completed that used HEC-RAS to calculate water-surface elevations in meander bends incorporating bendway weirs. One study was completed by Breck (2000) at Montana State University. Breck used HEC-RAS Version

2.2 for the purpose of modeling water-surface profiles over **a single bendway weir**. This study was completed for the Highwood Creek watershed, which is located in Central Montana, east of Great Falls. Figure 2.5 locates Highwood Creek in the vicinity of the project site. As Figure 2.5 illustrates, the valley gradient is relatively flat in the vicinity of the project site and sediment deposits tend to be coarse. Flat valley gradient and coarse sediment deposits fill existing channels and force the stream to move laterally. In order to restrict the channel from lateral movement, stream restoration, and bank-stabilization techniques were initiated in the spring of 1996.

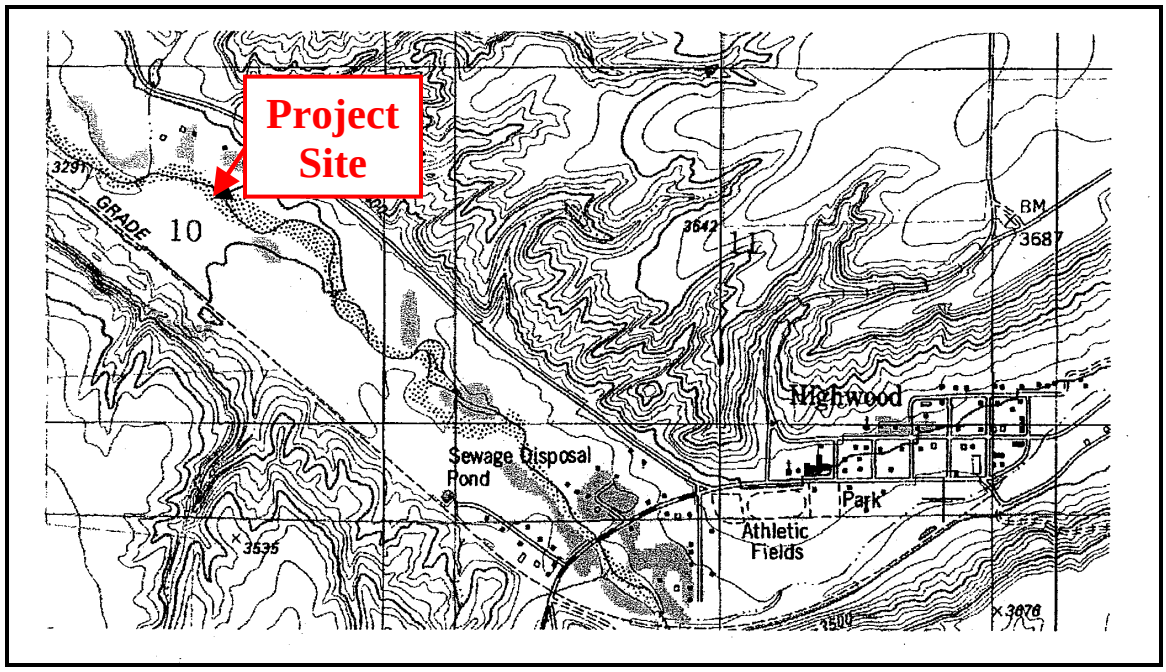

Figure 2.5. Highland Park Map (adapted from Breck (2000))

The project reach was fairly prismatic, approximately 200 ft in length. Five bendway weirs and a vortex weir were constructed along the reach. A vortex weir is a U- or V-shaped, instream rock structure typically composed of native material (Rosgen, 1996).

In order to build a HEC-RAS model for Highwood Creek, the following data were collected in the field:

1. Flow rate measurements using two methods:
    a. current meter; and
    b. United States Geological Survey (USGS) Database.
2. Manning's *n*-values:
    a. derived from roughness coefficient tables outlined in *Open-Channel Hydraulics* (Chow, 1959).
3. Topographical survey using a total station surveying device which surveyed:
    a. cross section upstream of reach;
    b. cross section downstream of reach; and
    c. water-surface elevations at upstream and downstream cross section.

In addition to the surveyed cross sections upstream and downstream of the study reach, survey data needed to be collected at the bendway weir. Two methods were presented by Breck to survey the bendway weir. Method 1 established five cross sections spaced equally, starting upstream and ending downstream of the bendway weir. Figure 2.6 illustrates the marked cross sections (XS) along the study reach. XS2 through XS6 illustrate the cross-section spacing across the bendway weir. Water-surface elevations were also collected at these cross sections. Unlike Method 1, Method 2 used "one cross section starting at the downstream end of the weir, perpendicular to the study reach, with points being taken along the main body of the structure and continuing perpendicular to the channel at the upstream end." Cross sections were also surveyed upstream and downstream of the bendway weir. Method 2 was used for the ease of collecting data but

the method was not used in the analysis since the survey did not provide enough detail to accurately calculate water-surface elevations across a bendway weir.

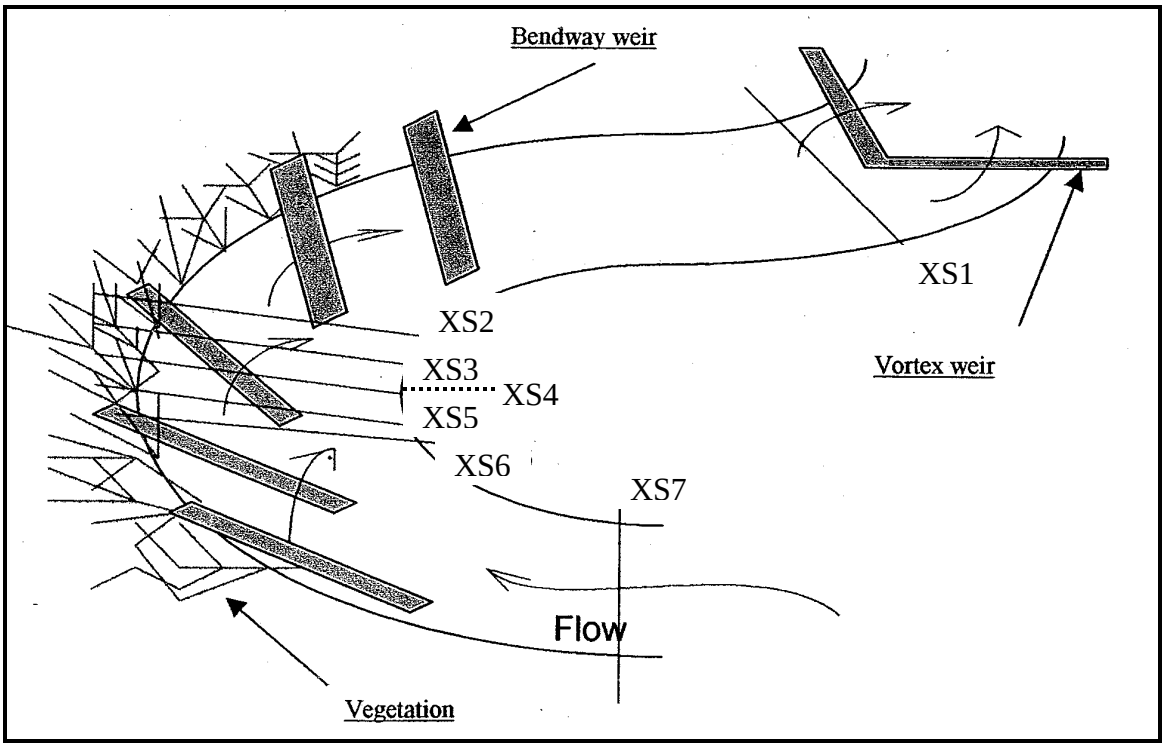

Figure 2.6. Study Reach Survey (adapted from Breck (2000))

From the field data, multiple HEC-RAS models were built in order to determine what methodology produced the most accurate output of water-surface elevations. Seven models, defined as "Options," were built in HEC-RAS and each model is outlined in Table 2.2. Each option assumed Manning's *n* was determined from field data and, therefore, further calibration of Manning's *n* was not required as part of the HEC-RAS analysis.

Table 2.2. Model Option Descriptions (Breck, 2000)

Model Option	Description
1	Survey Method 1 with interpolated cross sections between Station 2 and Station 6; ineffective flow lines on the outside of bendway weir.
2	Survey Method 1 with interpolated cross sections between Station 2 and Station 6; blocked obstructions replace bendway-weir profile in cross-section survey.
3	Survey Method 1 without additional options.
4	Survey Method 2 without additional options.
5	Survey Method 2 with one ineffective flow area.
6	Survey Method 2 with one blocked obstruction.
7	Partial blocked obstruction with ineffective flow areas.

Results of water-surface elevations and flow depths calculated by HEC-RAS confirmed that Option 1 and Option 2 were the most accurate HEC-RAS models. Breck summarized the accuracy of Option 1 and Option 2, and these results are shown in Table 2.3. From these results, Breck noted that the difference between Option 1 and Option 2 is not significant, but by adding additional flow rates over various weir dimensions might determine the superior option. Breck (2000) also noted that Option 1 and Option 2 might show more accurate water-surface elevations if further calibration of Manning's *n* was added to the scope of the analysis.

Table 2.3. Option 1 and Option 2 Accuracy (Breck, 2000)

Option	Option 1 Model Flow Depth (ft)	Option 2 Model Flow Depth (ft)	Observed Depth (ft)	Absolute Error (ft)	Absolute Error (ft)
1	0.95	1.09	1.05	0.100	0.040
2	1.01	1.08	1.04	0.030	0.040
1	0.81	0.81	0.92	0.110	0.110
2	0.86	0.86	0.95	0.090	0.090
1	0.87	0.86	0.98	0.110	0.120
2	0.92	0.91	1.00	0.080	0.090
1	0.93	0.92	1.06	0.130	0.140
2	0.98	0.97	1.08	0.100	0.110
1	0.88	0.88	0.92	0.040	0.040
2	0.94	0.94	0.95	0.010	0.010
			Average Absolute Error	**0.080**	**0.079**

2.6 NATURE OF FLOW IN MEANDER BENDS

Unlike straight channels where streamlines are uniform and parallel, meander bends create streamlines that are curvilinear and interwoven. Curvilinear and interwoven streamlines result in spiral currents and secondary currents (Chow, 1959). Spiral currents refer to movement of water particles along a helical path in the general direction of flow (Chow, 1959). In general, when water moves downstream, a channel curve to the right causes a counterclockwise spiral while a channel curve to the left causes a clockwise spiral. Secondary currents refer to velocity components parallel to the cross section. Spiral currents and secondary currents created in a meander bend are the result of the three factors stated by Chow (1959) in *Open-Channel Hydraulics*:

1. friction on the channel walls;
2. centrifugal force; and
3. vertical velocity distribution which exists in the approach channel.

Centrifugal forces cause the phenomenon in meander bends known as superelevation. Superelevation is the difference in water-surface elevation between the outside bank and inside bank along a cross section. Figure 2.7 illustrates superelevation along with the pressure distribution in a meander bend cross section, which creates spiral currents and secondary currents. Development of spiral currents and secondary currents is an additional source of minor losses due to meander bends.

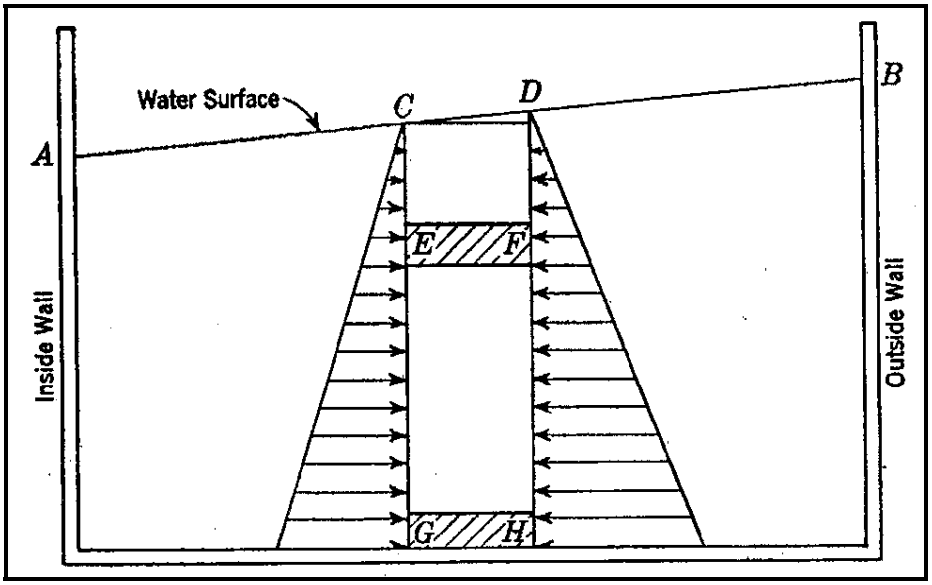

Figure 2.7. Pressure Distribution in a Meander Bend (Mockmore, 1944)

2.7 PREVIOUS STUDIES ON CALCULATING MINOR LOSSES DUE TO MEANDER BENDS

Various studies have been completed to estimate minor loss due to meander bends. Six methods to calculate minor loss due to meander bends are introduced in this section.

2.7.1 Yarnell and Woodward Method

Yarnell and Woodward (1936) stated in the bulletin, *Flow of Water Around 180-Degree Bends*, that minor losses due to bends could be calculated by Equation 2.18:

$$h_{BEND} = C * \frac{w}{r} * \frac{\bar{v}^2}{2g} \qquad \textbf{Equation 2.18}$$

where:

C = coefficient of loss;

g = acceleration of gravity (ft/s^2);

h_{BEND} = energy loss due to bend (ft);

r = inner radius (ft);

$\bar{v}$ = average velocity at a cross section (ft/s); and

w = width of channel (ft).

Assuming the channel is rectangular, Table 2.4 contains the list of channel dimensions and representative *C*-values. Yarnell and Woodward point out that coefficients shown in Table 2.4 only apply to the channel dimensions and bend radii stated for the coefficient.

Table 2.4. Yarnell and Woodward *C*-values

C	Channel Dimensions		Inner Radius (in.)
	Length (in.)	Width (in.)	
0.18	10	10	
0.23	5	10	5
0.23	5	10	10

2.7.2 Scobey Method

Chow (1959) reported in his book, *Open-Channel Hydraulics*, a method to calculate minor loss due to meander bends by Scobey in 1933. Scobey stated that minor losses in bends are taken into account by increasing *n*-values by 0.001 for each 20 degree of curvature in 100 ft of channel, but it is uncertain that *n* increases more than 0.002 to 0.003. Scobey's method was developed on the basis of flume tests.

2.7.3 Shukry Method

Chow (1959) reported in his book, *Open-Channel Hydraulics*, a method to calculate minor loss due to meander bends by Shukry in 1950. Shukry used a rectangular, steel flume to demonstrate that minor losses due to flow resistance in bends can be expressed as a coefficient multiplied by the velocity head at a cross section. Equation 2.19 illustrates this expression:

$$h_b = f_c * \frac{\bar{v}^2}{2g} \qquad \textbf{Equation 2.19}$$

where:

f_c = coefficient of curve resistance;

g = acceleration of gravity (ft/s^2);

h_b = minor loss due to the bend (ft); and

$\bar{v}$ = average velocity at a cross section (ft/s).

Shukry identified four significant parameters in order to classify flow in a bend. These parameters are shown in the following list:

1. r_c/b
2. y/b
3. $\theta/180$
4. Re

where:

b = channel width (ft);

r_c = radius of curvature (ft);

Re = Reynold's number;

θ = deviation angle of the curve; and

y = flow depth (ft).

Reynold's number is expressed by the following equation:

$$\mathrm{Re} = \frac{\bar{v}R}{\upsilon} \qquad \textbf{Equation 2.20}$$

where:

R = hydraulic radius (ft);

Re = Reynold's number;

υ = kinematic viscosity of a fluid (ft^2/s); and

$\bar{v}$ = average velocity at a cross section (ft/s).

Reynold's number ranged from 10,000 to 80,000 in Shukry's experiments.

2.7.4 Yen and Howe Method

Brater and King (1976) reported in their book, *Handbook of Hydraulics*, a method to calculate minor loss due to meander bends by Yen and Howe in 1942. Yen and Howe reported that minor loss due to meander bends is calculated by multiplying a coefficient by the velocity head at a cross section. Equation 2.21 presents the formula to calculate minor loss due to meander bend:

$$h_b = K_b * \frac{\bar{v}^2}{2g} \qquad \textbf{Equation 2.21}$$

where:

g = acceleration of gravity (ft/s^2);

h_b = minor loss due to bend (ft);

K_b = coefficient of curve resistance; and

$\bar{v}$ = average velocity at a cross section (ft/s).

K_b is equal to 0.38 for a 90° bend having a channel width of 11 in. and a radius of curvature of 5 ft.

2.7.5 Tilp and Scrivner Method

Brater and King (1976) reported in their book, *Handbook of Hydraulics*, a method to calculate minor loss due to meander bends by Tilp and Scrivner in 1964. Tilp and Scrivner suggested that minor losses due to bends could be estimated from the following equation:

$$h_b = 0.001 * (\Sigma\Delta^\circ) * \frac{\bar{v}^2}{2g} \qquad \textbf{Equation 2.22}$$

where:

g = acceleration of gravity (ft/s^2);

h_b = minor loss due to bend (ft);

$\Sigma\Delta°$ = summation of deflection angles; and

$\bar{v}$ = average velocity at a cross section (ft/s).

Tilp and Scrivner developed this equation based on large, concrete-lined canals.

2.7.6 Lansford Method

Robertson introduced an equation by Lansford in the *American Society of Civil Engineers Paper No. 2217* (Mockmore, 1944). Lansford reported that difference in pressure of fluid flowing in a bend could be expressed by Equation 2.23:

$$\Delta h = \frac{2b}{r_c} * \frac{\bar{v}^2}{2g} \qquad \textbf{Equation 2.23}$$

where:

b = channel width (ft);

Δh = difference in pressure of fluid flowing (ft);

g = acceleration of gravity (ft/s^2);

r_c = radius of curvature (ft); and

$\bar{v}$ = average velocity at a cross section (ft/s).

This relationship is due to centrifugal forces of water acting on a channel bend and was developed for closed conduit bends.

2.7.7 Summary

Limitations were required to calculate minor loss due to meander bend in each method stated in Section 2.7. For instance, the Yarnell and Woodward method noted that the coefficient of loss required to calculate energy loss due to the bend in Equation 2.18 only applied to design flumes with dimensions specified in Table 2.4. Table 2.4 indicated that the maximum channel length and channel width was 10 in. The Shukry method used Equation 2.19 to calculate minor loss due to the bend using a coefficient of curve resistance. Coefficient of curve resistance was developed for a rectangular, steel flume with Reynold's numbers ranging from 10,000 to 80,000. The Yen and Howe method noted that minor loss due to the bend is calculated in Equation 2.21 using a coefficient of curve resistance. Coefficient of curve resistance is limited to a design flume with a 90° bend, 11-in. channel width, and 5-ft radius of curvature.

Constraints required to calculated the minor loss due to meander bend limited the applicability of each method. A method needs to be developed in order to calculate minor loss due to meander bend in open-channel systems for an array of bend angles, channel widths, and channel lengths.

CHAPTER 3 DATA COLLECTION

3.1 INTRODUCTION

In order to develop a HEC-RAS model for bendway-weir analysis, survey data were collected and a testing program was conducted to collect flow-depth measurements with and without bendway weirs. The testing program was divided into two parts: base-line testing and bendway-weir testing. A base-line testing program was conducted in order to build a HEC-RAS model without bendway weirs. A bendway-weir testing program was conducted to build a HEC-RAS model for one bendway-weir configuration. Bendway-weir configurations consisted of a set weir length, weir height, weir spacing, and orientation angle for a known meander bend geometry. All tests were conducted in a 1:12 Froude scale, rigid, concrete boundary, physical hydraulic model constructed in the Hydromachinery Laboratory at the Engineering Research Center, Colorado State University. Figure 3.1 shows the location of the Hydromachinery Laboratory at the Engineering Research Center.

Figure 3.1. Location of Hydromachinery Laboratory at the Engineering Research Center

3.2 MODEL DESCRIPTION

An undistorted 1:12 Froude scale, rigid, concrete boundary, physical hydraulic model was constructed to represent meander bends in a 29-mile study reach of the Middle Rio Grande. Figure 3.2 locates the 29-mile study reach in New Mexico. Based on planform data collected along the 29-mile reach of the Middle Rio Grande, two representative meander bends were constructed and separated by a transition section. Geometry characteristics of the Middle Rio Grande and the physical model are shown in Table 3.1 and Table 3.2, respectively. **Type I** identifies the upstream bend in the physical model and **Type III** identifies the downstream bend in the physical model. Cross-sectional geometry was trapezoidal with 1:3 side slopes. The Type I and Type III bends were connected through the transition section in order to adjust the physical model geometry from a top width of 19.2 ft to 15.0 ft. Both meander bends were designed at a bed slope of 0.000863 ft/ft.

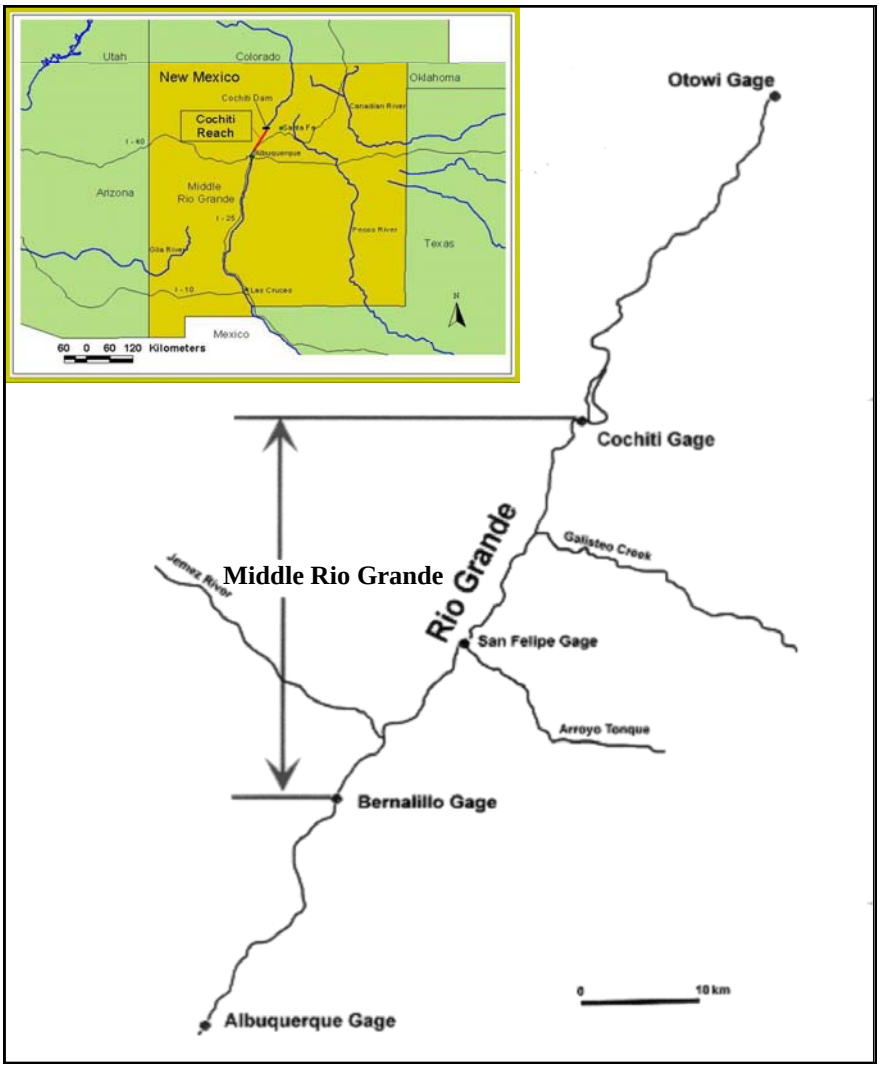

Figure 3.2. Map Locating the Middle Rio Grande (Darrow, 2004)

Table 3.1. Middle Rio Grande Geometry Characteristics (Heintz, 2002)

Type	Top Width (ft)	Radius of Curvature (ft)	Orientation Angle	Relative Curvature	Channel Length (ft)
1	230	465	125	2.02	1014
3	180	790	73	4.39	1002

Table 3.2. Physical Model Geometry Characteristics (Heintz, 2002)

Type	Top Width (ft)	Radius of Curvature (ft)	Orientation Angle	Relative Curvature	Channel Length (ft)
1	19	39	125	2.02	85
3	15	66	73	4.39	84

Eighteen cross sections were marked along the physical model. A planform view of the physical model with the eighteen marked cross sections is shown in Figure 3.3. For this analysis, an additional cross section, XS0, was included to obtain survey data and flow-depth measurements at a cross section before entering the Type I bend. A full description of the physical model is found in *Investigation of Bendway Weir Spacing* by Heintz (2002).

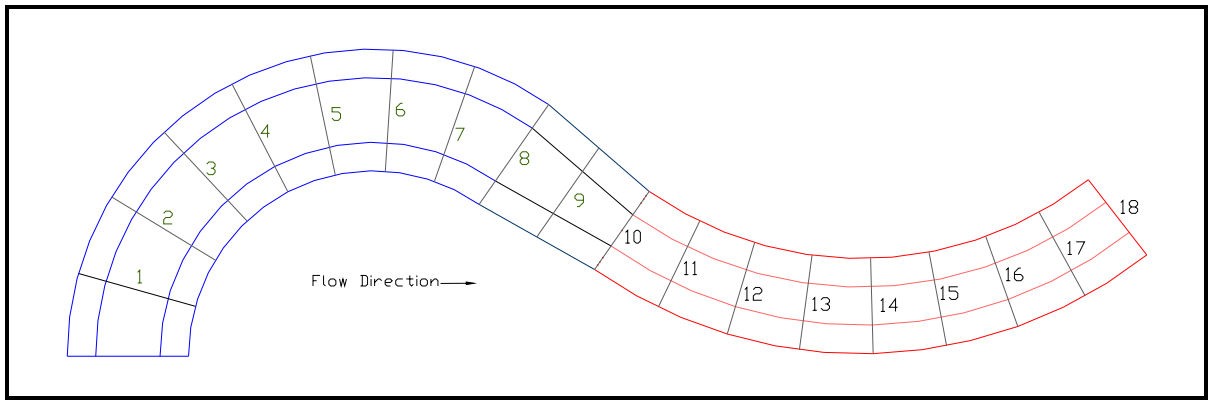

Figure 3.3. Physical Model Plan View With Defined Cross Sections (Heintz, 2002)

3.3 CROSS-SECTION DATA

In order to build a HEC-RAS model, cross-section data needed to be collected throughout the physical model. Cross-section data were collected through two types of surveying in order to obtain the best set of cross-section data. Survey data of the physical model was collected through total station and standard level instrumentation. Survey

data were collected at the nineteen cross sections. Shots included the upstream side of each piezometer, at the toe on the left and right banks, at the top of bank of the left and right banks, and against the side of the model for the overbank shot of the left and right banks. Figure 3.4 illustrates a typical cross section in the Type I and Type III bends. Rod placement for shots taken at piezometers is illustrated in Figure 3.5 and Figure 3.6.

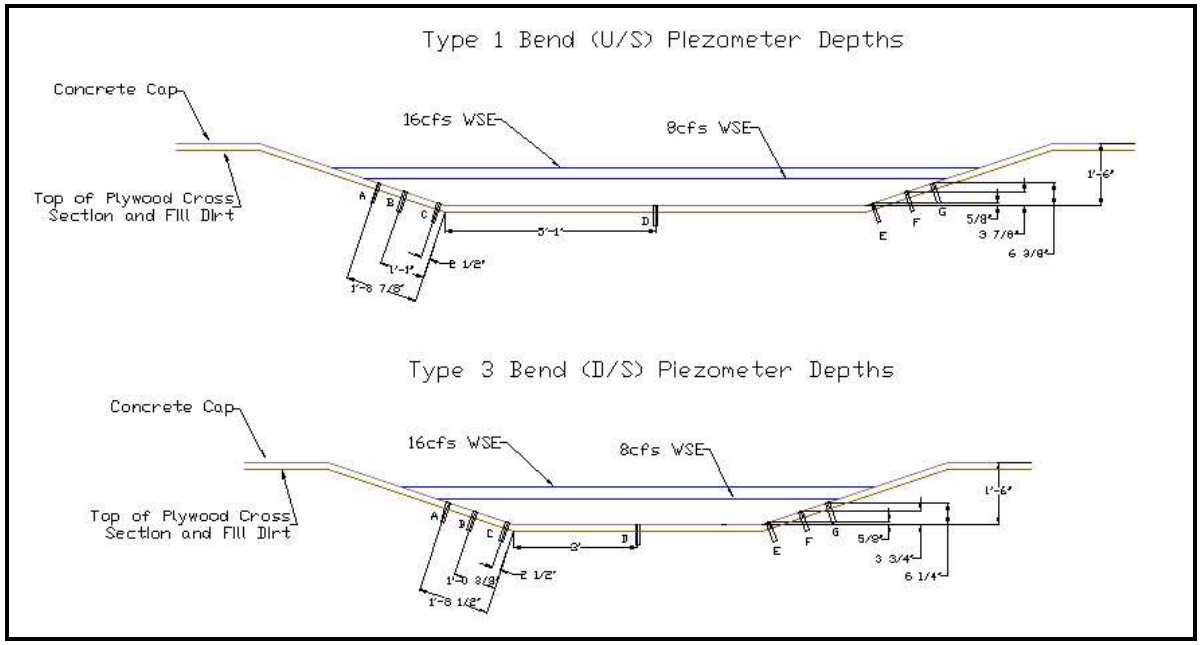

Figure 3.4. Piezometer Location Along Cross Sections in the Type I and Type III Bends (Heintz, 2002)

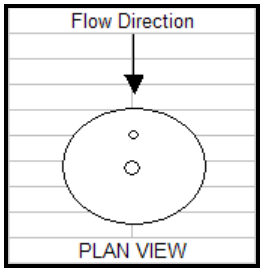

Figure 3.5. Rod Placement in Planform View

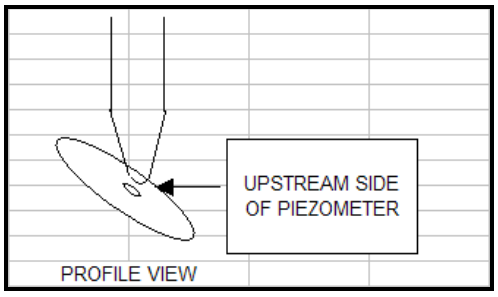

Figure 3.6. Rod Placement in Profile View

Once the cross-section data were collected using the total station and the standard level, cross-section data were compared in order to determined the best set of cross-section data for the analysis. Figure 3.7 presents the graph of survey data collected at XS5 using total station and standard level instrumentation. As Figure 3.7 indicates, the difference between the total station and standard level survey was minimal and, therefore, the total station survey was used in the analysis. Appendix A contains the survey data shot at each cross section using the total station instrumentation.

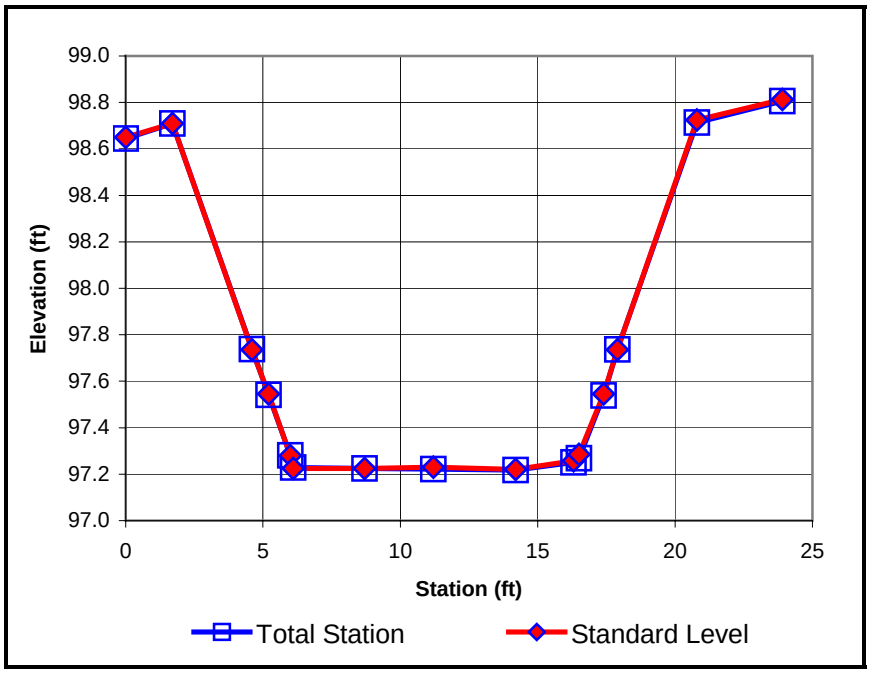

Figure 3.7. Total Station and Standard Level Survey Comparison at XS5

3.4 FLOW CONDITIONS

Discharges found in the Middle Rio Grande that were simulated in the physical model were 4,000, 6,000, and 8,000 cfs. These flow rates corresponded to design discharges of 8, 12, and 16 cfs in the physical model.

In order to determine the correct tailwater depth that simulates normal flow-depth conditions throughout the model, a stop log system was calibrated at the downstream end of the Type III bend. Detail related to the calibration method is found in *Investigation of Bendway Weir Spacing* by Heintz (2002).

3.5 TESTING PROGRAM

Flow-depth measurements were collected along the physical model with and without bendway weirs. Base-line testing program refers to flow depths measured in the physical model without weirs. Bendway-weir testing program refers to flow depths measured in the physical model with bendway weirs.

During the base-line testing program, flow depths were measured along the center of the channel without bendway weirs. Figure 3.8 is a photograph of the physical model without bendway weirs.

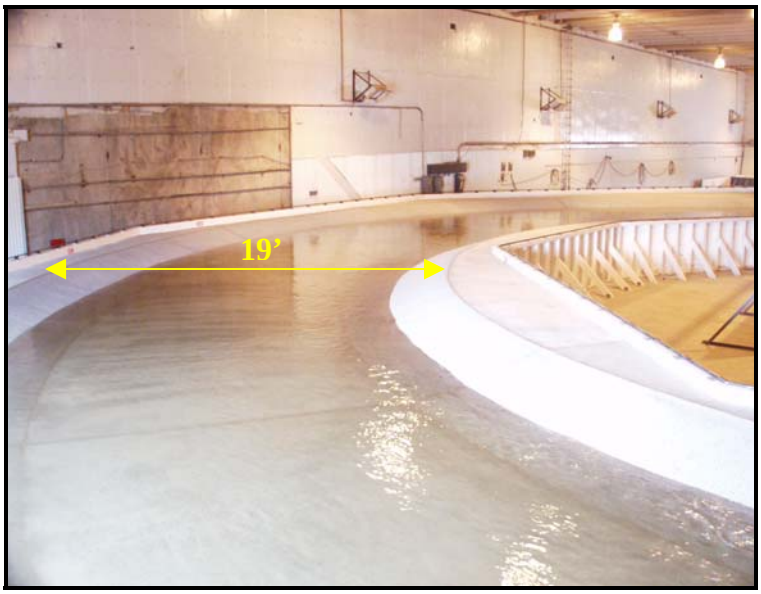

Figure 3.8. Physical Model Without Bendway Weirs (adapted from Heintz (2002))

The bendway-weir testing program measured flow depths along the center of the channel with one bendway-weir configuration. Figure 3.9 is a photograph of the physical model with bendway weirs. Bendway weirs are uniformly dimensioned in each bend. Geometry characteristics defining weirs placed in the physical model are illustrated in Figure 3.10. Weir dimensions are defined as follows:

1. L_{cw} = length of crest along bendway weir (ft);
2. L_w = total length of bendway weir (ft);
3. W_{bw} = base width of bendway weir (ft); and
4. W_{cw} = crest width of bendway weir (ft).

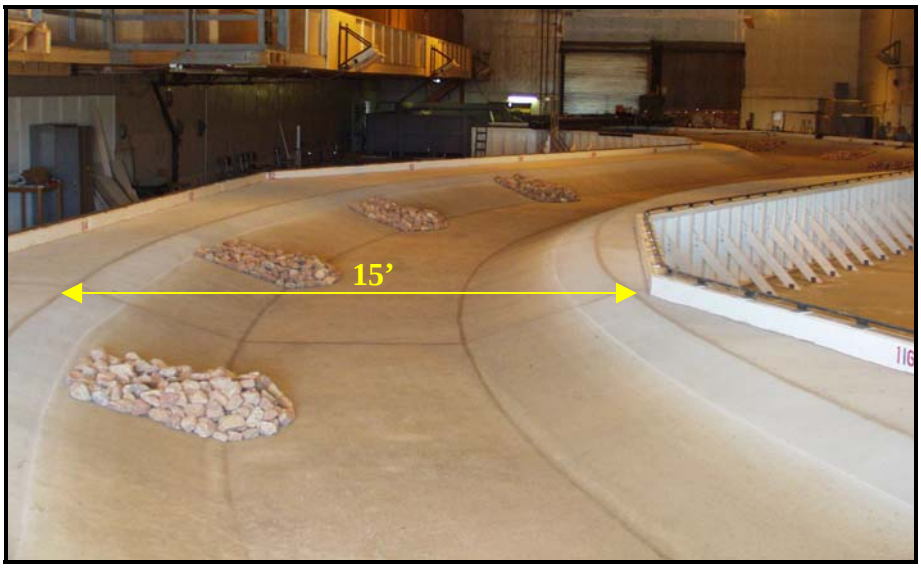

Figure 3.9. Physical Model With Bendway Weirs (adapted from Heintz (2002))

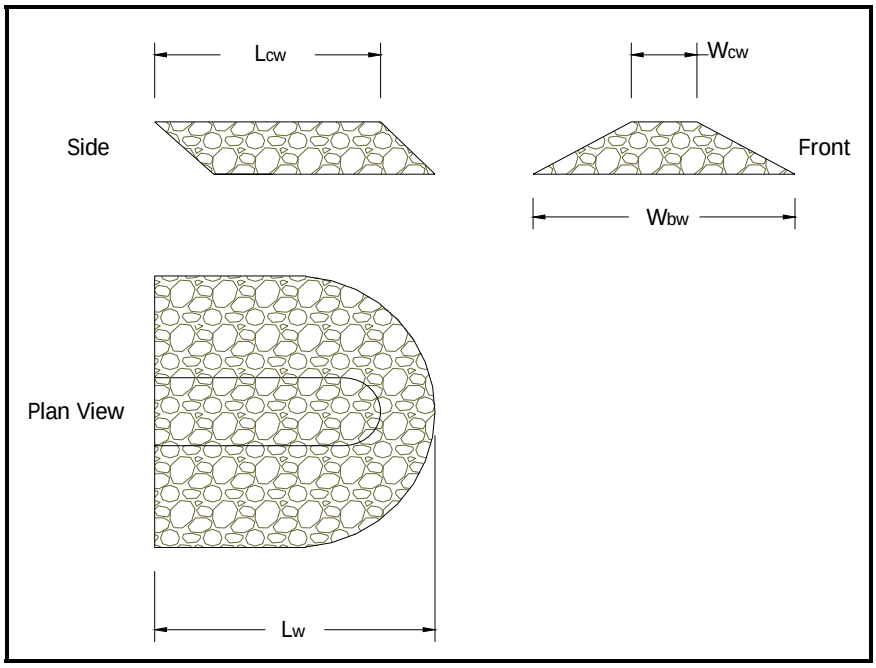

Figure 3.10. Bendway-weir Dimensions (Heintz, 2002)

Weirs are also spaced uniformly along each bend. Weirs are spaced according to the spacing ratio, which is defined by “measuring the arc length between the weirs at the

design water line along the bank" (Heintz, 2002). Spacing ratio is calculated using Equation 3.1:

$$S = \frac{r\theta_w}{L_r TW} \qquad \textbf{Equation 3.1}$$

where:

L_r = bendway-weir length ratio (ft);

r = radius of curvature (ft);

S = spacing ratio;

θ_w = orientation angle; and

TW = top width of channel (ft).

L_r is defined by Equation 3.2:

$$L_r = \frac{L_w}{TW} \qquad \textbf{Equation 3.2}$$

where:

L_r = bendway-weir length ratio;

L_w = total length of bendway weir (ft); and

TW = top width of channel along cross section (ft).

Each variable required in the calculation of spacing ratio and bendway-weir length ratio is presented in Figure 3.11. As Figure 3.11 illustrates, the orientation angle is measured from the centerline of the weir and, therefore, angles less than 90° orient the bendway weir upstream and angles greater than 90° orient the bendway weir downstream.

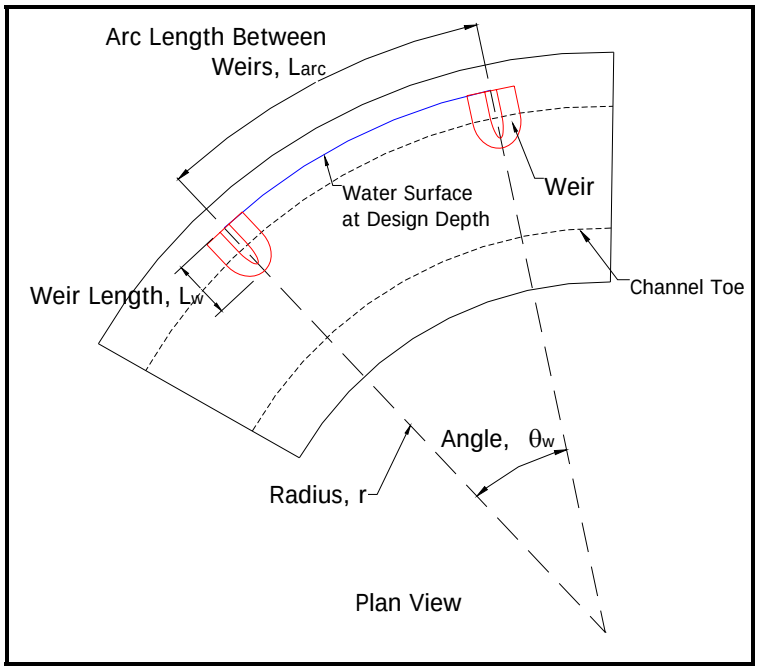

Figure 3.11. Spacing Ratio Schematic (Heintz, 2002)

In this analysis, bendway-weir configurations in the Type I and Type III bends are characterized using the dimensions, spacing ratio, and orientation angle shown in Table 3.3. As Table 3.3 presents, the Type I bend contains five bendway weirs with a spacing ratio of 4.10 and the Type III bend contains three bendway weirs with a spacing ratio of the 7.62. A planform view of the Type I and Type III bends with the bendway-weir configuration is shown in Figure 3.12.

Table 3.3. Bendway-weir Characteristics

Bend	L_{cw} (ft)	L_w (ft)	W_{cw} (ft)	W_{bw} (ft)	L_{arc} (ft)	S	Number of Weirs
1	4.29	5.06	1	4	20.03	4.1	5
3	2.96	3.74	1	4	28.53	7.62	3

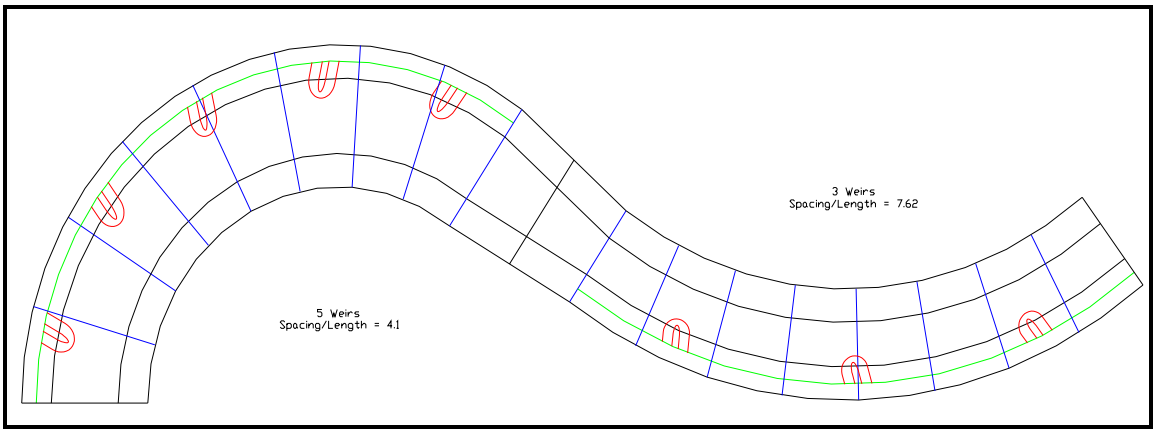

Figure 3.12. Planform View of Bendway-weir Configuration (Heintz, 2002)

3.5.1 Flow-depth Measurements

Flow-depth measurements were collected during the base-line and bendway-weir testing program. Flow-depth measurements were measured to the thousandth place using a track-mounted point gage. The track-mounted point gage was installed along a data-collection cart designed to collect data at any point along a cross section. In the base-line testing program, flow-depth measurements were collected along the center of the channel at all nineteen cross sections. Flow-depth measurements collected during the base-line test are shown in Table 3.4. Flow-depth measurements recorded at 8 cfs were collected on February 24, 2004 and flow-depth measurements recorded at 12 cfs and 16 cfs were collected on June 6, 2004.

Table 3.4. Base-line Testing Program Flow-depth Measurements

XS*	$y_{8\ cfs}$ (ft)	$y_{12\ cfs}$ (ft)	$y_{16\ cfs}$ (ft)
0 (U/S)	0.610	0.824	0.937
1	0.591	0.801	0.920
2	0.604	0.811	0.927
3	0.607	0.808	0.919
4	0.605	0.813	0.923
5	0.591	0.799	0.912
6	0.593	0.811	0.925
7	0.612	0.813	0.930
8	0.602	0.831	0.934
9	0.606	0.822	0.933
10	0.593	0.800	0.906
11	0.587	0.802	0.906
12	0.583	0.802	0.901
13	0.589	0.797	0.901
14	0.589	0.809	0.911
15	0.578	0.807	0.902
16	0.608	0.829	0.924
17	0.604	0.830	0.926
18 (D/S)	0.616	0.838	0.932

*U/S – upstream; D/S – downstream

In the bendway-weir testing program, flow-depth measurements were collected along the center of the channel for XS1 through XS17. Flow-depth measurements collected with the track-mounted point gage during the bendway-weir testing program are shown in Table 3.5. Flow-depth measurements recorded at 8 cfs were collected on June 14, 2004 and flow-depth measurements recorded at discharges of 12 cfs and 16 cfs were collected on June 15, 2004 and June 23, 2004, respectively. Appendix B contains all data sheets for the base-line testing program and the bendway-weir testing program.

Table 3.5. Bendway-weir Testing Program Flow-depth Measurements

XS	$y_{8\ cfs}$ (ft)	$y_{12\ cfs}$ (ft)	$y_{16\ cfs}$ (ft)
0 (U/S)			
1	0.700	0.890	1.008
2	0.700	0.905	1.020
3	0.698	0.886	1.000
4	0.705	0.892	1.015
5	0.689	0.886	0.995
6	0.696	0.887	1.010
7	0.687	0.901	1.012
8	0.686	0.889	0.999
9	0.740	0.920	1.021
10	0.699	0.914	1.007
11	0.698	0.912	1.010
12	0.610	0.820	0.910
13	0.632	0.858	0.930
14	0.605	0.833	0.899
15	0.594	0.831	0.891
16	0.632	0.865	0.899
17	0.570	0.810	0.884
18 (D/S)			

CHAPTER 4 BASE-LINE ANALYSIS

4.1 INTRODUCTION

Base-line analysis involved building a HEC-RAS model that matched the flow depth in the physical model with **NO** bendway weirs. Specific options in HEC-RAS were used to build the model. The HEC-RAS options used to build the base-line model were:

1. Manning's *n*;
2. contraction coefficient; and
3. expansion coefficient.

By adjusting Manning's *n*, and the contraction, and expansion coefficients, the goal of matching the physical model flow depths with HEC-RAS could be achieved. Once the goal was achieved, the base-line model was used as the foundation model for bendway-weir analysis.

4.2 BASE-LINE MODEL – ORIGINAL TEST

The Original Test was the first attempt to build a model in HEC-RAS. The goal of the Original Test was to numerically model flow depths in the physical model with no bendway weirs.

4.2.1 Original Test Input Parameters

In order to build the HEC-RAS model, total station survey data were added to a HEC-RAS geometry file along with information about channel lengths, and left and right overbank lengths between cross sections. Once the survey data and information regarding the distance between cross sections was added to the geometry file, edits were made to Manning's *n*. Manning's *n* was set to a value of 0.015 at all cross sections in the concrete, rigid boundary model. Manning's *n*-values were found in the *River Analysis System Hydraulic Reference Manual* for HEC-RAS Version 3.0 (USACE, 2001a). No changes were made to the default values of the contraction and expansion coefficients. Default values of contraction and expansion coefficients were set to 0.1 and 0.3, respectively. Once survey data were entered into the HEC-RAS geometry file, discharge data were entered into the HEC-RAS steady flow file. Discharges of interest were 8 cfs, 12 cfs, and 16 cfs. Along with the discharge data, a downstream boundary condition was entered in the steady flow file since the flow regime was assumed to be subcritical. The project goal of creating a HEC-RAS model that matched flow depths in the physical model controlled the decision to use a known water-surface elevation as the downstream boundary condition. Known water-surface elevations were established to match the water-surface elevation at XS18. Table 4.1 presents known water-surface elevations used in HEC-RAS.

Table 4.1. Known Water-surface Elevations (*WSE*)

Q (cfs)	*WSE* (ft)
8	97.706
12	97.928
16	98.022

4.2.2 Original Test Results

Original Test results used HEC-RAS output for computed water-surface elevations at all cross sections marked along the physical model. The water-surface elevations were used to calculate the flow depth at each cross section. Equation 4.1 presents the equation used to estimate flow depths along the center of the channel:

$$y = WSE - z_D \qquad \textbf{Equation 4.1}$$

where:

WSE = water-surface elevation along the cross section (ft);

y = flow depth (ft); and

z_D = surveyed bed elevation at Piezometer D (ft).

Flow-depth estimates are calculated using Equation 4.1 even though HEC-RAS contains an output option of Maximum Channel Depth. Maximum Channel Depth would be a valid estimate of flow depth if the minimum cross-section elevation always occurred at Piezometer D. In the physical model, this was not always the case and, therefore, flow-depth estimates needed to be calculated using Equation 4.1. Table 4.2 presents the flow-depth results for the Original Test of the base-line model. Flow depths estimated by HEC-RAS in Table 4.2 were compared to the physical model flow-depth measurements along the Type I and Type III meander bends. Figure 4.1 compares flow-depth measurements from HEC-RAS computations to flow-depth measurements along the physical model. These values were further evaluated by observing the difference between average flow depths calculated in HEC-RAS to average flow-depth measurements in the physical model for the Type I and Type III bends. For each discharge, Table 4.3 displays the average flow depth in the Type I and Type III bends for

a discharge of 8 cfs, 12 cfs, and 16 cfs. As shown in Table 4.3 and Figure 4.1, flow depths computed in HEC-RAS at 8 cfs overestimated flow depths in the physical model by 0.0114 ft in the Type I bend and by 0.0127 ft in the Type III bend. Modifications needed to be made to HEC-RAS in order to better estimate flow-depth measurements in the physical model.

Table 4.2. Base-line Original Test Flow-depth Measurements

XS	$y_{8\ cfs}$ (ft)	$y_{12\ cfs}$ (ft)	$y_{16\ cfs}$ (ft)
0 (U/S)	0.591	0.788	0.903
1	0.598	0.796	0.910
2	0.615	0.813	0.928
3	0.611	0.810	0.924
4	0.618	0.817	0.931
5	0.605	0.805	0.918
6	0.612	0.812	0.925
7	0.619	0.820	0.933
8	0.626	0.828	0.940
9	0.621	0.823	0.931
10	0.597	0.800	0.903
11	0.609	0.813	0.914
12	0.599	0.806	0.907
13	0.599	0.808	0.908
14	0.601	0.812	0.911
15	0.591	0.805	0.903
16	0.614	0.831	0.927
17	0.614	0.833	0.928
18 (D/S)	0.616	0.838	0.932

Table 4.3. Difference in Average Flow Depth Between HEC-RAS Output and Physical Model During the Original Test

Bend	$y_{8\ cfs}$ (ft)	$y_{12\ cfs}$ (ft)	$y_{16\ cfs}$ (ft)
Type I (U/S) Bend	0.0114	0.0017	0.0019
Type III (D/S) Bend	0.0127	0.0047	0.0039

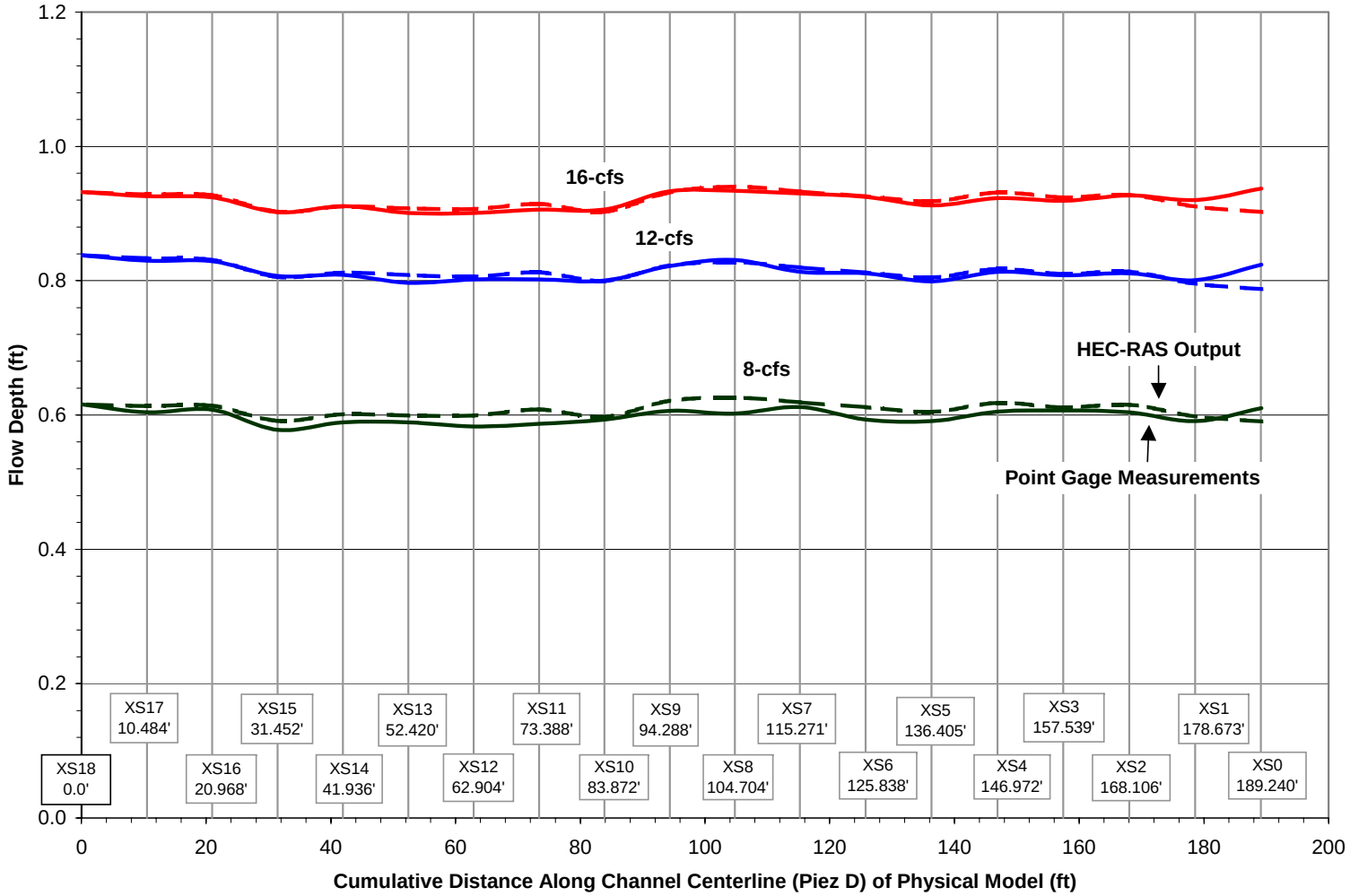

Figure 4.1. Comparison of Flow Depth Measured Along Physical Model and Flow Depth Estimated During the Original Test

4.3 MODIFIED TEST OF THE BASE-LINE MODEL

The Modified Test was the second attempt to build a HEC-RAS model that matched flow depths similar to the physical model. The Modified Test used the Original Test plan as a foundation for the HEC-RAS analysis.

4.3.1 Modified Test Input Parameters

Similar to the Original Test, the Modified Test geometry information such as cross-section data, channel length, and overbank length data remained the same. Unlike the Original Test, the Modified Test Manning's *n*-values were set to 0.013 and the contraction coefficients were set to 0.6 in the transition section of the model. The transition section was identified by XS9 and XS10. Table 4.4 presents the HEC-RAS expansion and contraction coefficient input table with the adjusted values.

Table 4.4. HEC-RAS Contraction and Expansion Coefficients Used During the Modified Test

XS	C_c	C_e
0 (U/S)	0.1	0.3
1	0.1	0.3
2	0.1	0.3
3	0.1	0.3
4	0.1	0.3
5	0.1	0.3
6	0.1	0.3
7	0.1	0.3
8	0.1	0.3
9	**0.6**	0.3
10	**0.6**	0.3
11	0.1	0.3
12	0.1	0.3
13	0.1	0.3
14	0.1	0.3
15	0.1	0.3
16	0.1	0.3
17	0.1	0.3
18 (D/S)	0.1	0.3

In the steady flow file, no adjustments were made. The simulated flow rates remained 8 cfs, 12 cfs, and 16 cfs and the downstream boundary condition was a known water-surface elevation. Known water-surface elevations were presented in Table 4.1.

4.3.2 Modified Test Results

Modified Test results used HEC-RAS output of computed water-surface elevations to calculate flow depths at all cross sections marked along the physical model. Water-surface elevations were evaluated with Equation 4.1; Table 4.5 presents the flow-depth results. Flow depths estimated in Table 4.5 were compared to physical model flow-depth measurements along the Type I and Type III meander bends. Figure 4.2 presents a comparison of flow depths calculated through HEC-RAS computation to flow-depth measurements along the physical model. These values were further evaluated by observing the difference between average flow depths estimated from HEC-RAS to average flow-depth measurements in the physical model for the Type I and Type III bends. Results are presented in Table 4.6. Based on calculations presented in Table 4.6, flow depths estimated by HEC-RAS during the Modified Test were more accurate than flow depths estimated during the Original Test. For example, at 16 cfs, the difference in average flow depth estimated from HEC-RAS and measured in the physical model during the Modified Test was 0.56% in the Type I bend and 0.43% in the Type III bend.

Table 4.5. Modified Test Flow-depth Measurements

XS	$y_{8\ cfs}$ (ft)	$y_{12\ cfs}$ (ft)	$y_{16\ cfs}$ (ft)
0 (U/S)	0.578	0.778	0.896
1	0.586	0.787	0.905
2	0.604	0.805	0.923
3	0.601	0.803	0.920
4	0.609	0.811	0.928
5	0.596	0.799	0.916
6	0.604	0.807	0.924
7	0.612	0.815	0.932
8	0.619	0.823	0.940
9	0.615	0.819	0.932
10	0.581	0.787	0.889
11	0.594	0.801	0.902
12	0.586	0.796	0.896
13	0.588	0.800	0.899
14	0.591	0.805	0.903
15	0.584	0.800	0.897
16	0.610	0.828	0.924
17	0.611	0.832	0.927
18 (D/S)	0.616	0.838	0.932

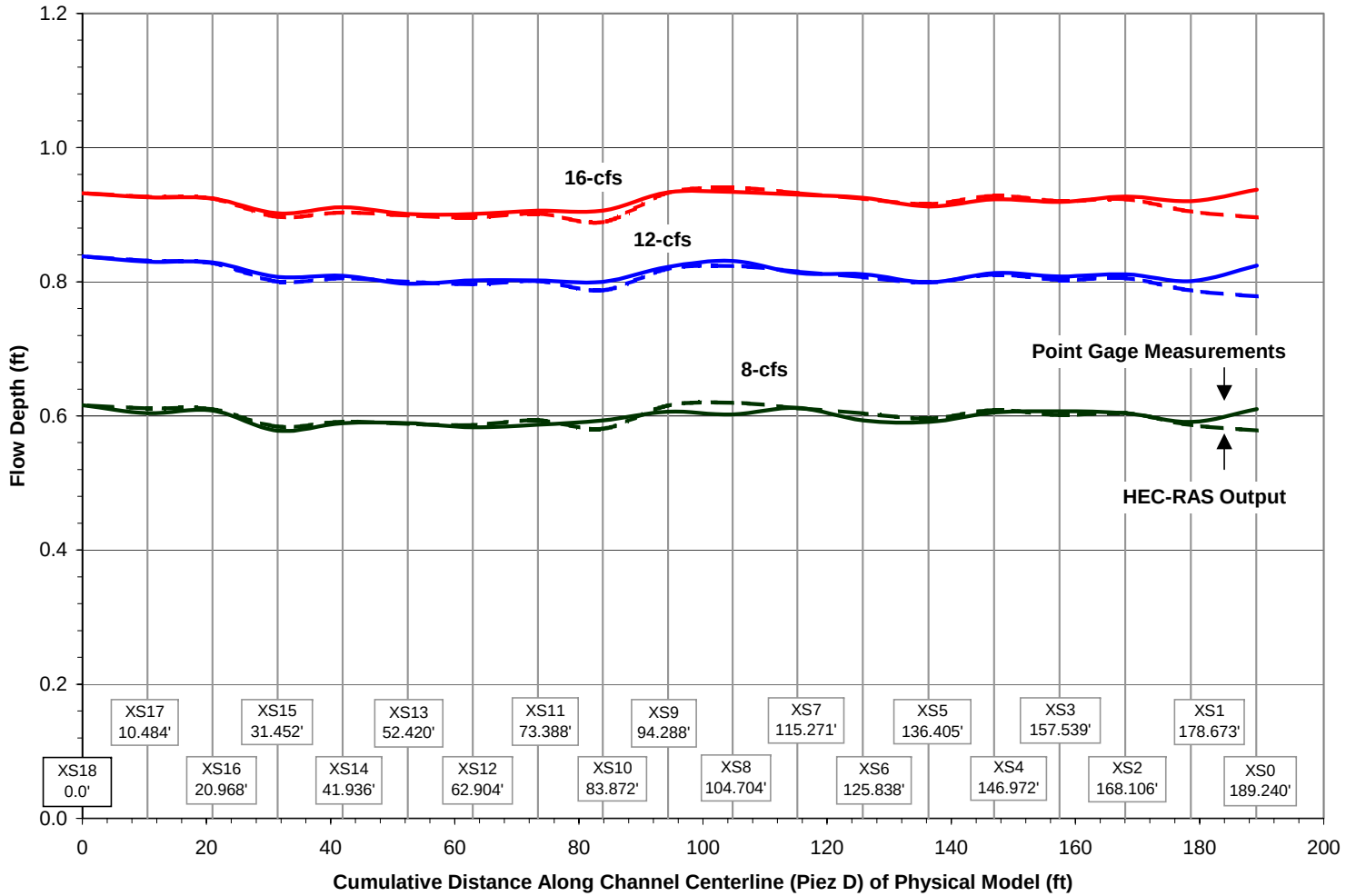

Figure 4.2. Comparison of Flow Depth Measured Along Physical Model and Flow Depth Estimated During the Modified Test

Table 4.6. Difference in Average Flow Depth Between HEC-RAS Output and Physical Model During the Modified Test

Bend	$y_{8\ cfs}$ (ft)	$y_{12\ cfs}$ (ft)	$y_{16\ cfs}$ (ft
Type I (U/S) Bend	0.0015	0.0053	0.0018
Type III (D/S) Bend	0.0038	0.0020	0.0034

4.4 BASE-LINE MODEL SELECTION

Selection of a base-line model focused on the project goal to determine a HEC-RAS model that matched flow depths in the physical model. Since flow depths estimated during the Modified Test resembled flow depths measured in the physical model, the Modified Test was selected. The Modified Test Base-line Model was considered the foundation model for bendway-weir analysis in HEC-RAS.

CHAPTER 5 BENDWAY-WEIR ANALYSIS

5.1 INTRODUCTION

Bendway-weir analysis was the process used to determine a HEC-RAS model that matched the flow depth and total energy loss in the physical model with bendway weirs. The HEC-RAS model was built using the Modified Test Base-line Model as a foundation.

5.2 TRIAL DEFINITIONS

A system needed to be developed in order to organize and define each variation of the bendway-weir model in HEC-RAS. Each variation of the HEC-RAS model was defined as a **Trial**. Sixteen trials were developed in an attempt to build an optimal HEC-RAS model. Trial definitions are listed in Table 5.1.

Table 5.1. Trial List

Trial Number	Description
Trial 1	Manning's n changed at all cross sections with bendway weirs, all flow rates looked at with same geometry file, **NOT** independently of each other.
Trial 2 (8 cfs)	Manning's n changed at all cross sections with bendway weirs. Flow rate, 8 cfs, has geometry file specific to the 8 cfs model run.
Trial 2 (12 cfs)	Manning's n changed at all cross sections with bendway weirs. Flow rate, 12 cfs, has geometry file specific to the 12 cfs model run.
Trial 2 (16 cfs)	Manning's n changed at all cross sections with bendway weirs. Flow rate, 16 cfs, has geometry file specific to the 16 cfs model run.
Trial 3	Contraction/Expansion coefficients only variables adjusted. Used the HEC-RAS base-line model to make adjustments to contraction and expansion coefficients for all cross sections which contained a bendway weir. Look at all flow rates with the same geometry file **NOT** independently from one another.
Trial 4 (8 cfs)	Adjust the Contraction/Expansion coefficients to the 8 cfs, Trial 2 (8 cfs) geometry file.
Trial 4 (12 cfs)	Adjust the Contraction/Expansion coefficients to the 12 cfs, Trial 2 (12 cfs) geometry file.
Trial 4 (16 cfs)	Adjust the Contraction/Expansion coefficients to the 16 cfs, Trial 2 (16 cfs) geometry file.
Trial 5 (8 cfs)	Adjust the contraction coefficients for transition section of physical model (XS8 through XS10) for the 8 cfs, Trial 4 geometry file.
Trial 5 (12 cfs)	Adjust the contraction coefficients for transition section of physical model (XS8 through XS10) for the 12 cfs, Trial 4 geometry file.
Trial 5 (16 cfs)	Adjust the contraction coefficients for transition section of physical model (XS8 through XS10) for the 16 cfs, Trial 4 geometry file.
Trial 6	Build block obstructions at each bendway-weir location in the Type III (D/S) bend. Look at all flow rates with same geometry file, **NOT** independently of one another.
Trial 7	Add ineffective flow lines to the Trial 6, HEC-RAS model upstream and downstream of each blocked structure (representing each bendway weir) to represent the dead zones and eddies between bendway weirs. Look at all flow rates with the same geometry file, **NOT** independently of one another.
Trial 8 (8 cfs)	Use Trial 7 geometry file and change Manning's n and Contraction/Expansion coefficients at all cross sections with bendway weirs. Change Manning's n specifically for 8 cfs model run.
Trial 8 (12 cfs)	Use Trial 7 geometry file and change Manning's n and Contraction/Expansion coefficients at all cross sections with bendway weirs. Change Manning's n specifically for 12 cfs model run.
Trial 8 (16 cfs)	Use Trial 7 geometry file and change Manning's n and Contraction/Expansion coefficients at all cross sections with bendway weirs. Change Manning's n specifically for 16 cfs model run.
Trial 9	Delete block obstructions from the Trial 7 geometry file and mark each weir by an ineffective flow line. Look at all flow rates with the same geometry file, **NOT** independently of one another.
Trial 10 (8 cfs)	Use Trial 8 (8 cfs) geometry file and adjust Manning's n by stations across each cross section with a bendway weir instead of adjusting Manning's n by left overbank, channel, and right overbank.

Trial Number	Description
Trial 10 (12 cfs)	Use Trial 8 (12 cfs) geometry file and adjust Manning's n by stations across each cross section with a bendway weir instead of adjusting Manning's n by left overbank, channel, and right overbank.
Trial 10 (16 cfs)	Use Trial 8 (16 cfs) geometry file and adjust Manning's n by stations across each cross section with a bendway weir instead of adjusting Manning's n by left overbank, channel, and right overbank.
Trial 11 (8 cfs)	Use Trial 8 (8 cfs) and add ineffective flow lines at the cross sections containing bendway weirs. The ineffective flow lines were added to show water passing over the high point of the bendway weir moved from the upstream eddy to the eddy downstream of the bendway weir. The flow that passes over this portion of the bendway weir is considered ineffective since it conforms to the downstream eddy.
Trial 11 (12 cfs)	Use Trial 8 (12 cfs) and add ineffective flow lines at the cross sections containing bendway weirs. The ineffective flow lines were added to show water passing over the high point of the bendway weir moved from the upstream eddy to the eddy downstream of the bendway weir. The flow that passes over this portion of the bendway weir is considered ineffective since it conforms to the downstream eddy.
Trial 11 (16 cfs)	Use Trial 8 (16 cfs) and add ineffective flow lines at the cross sections containing bendway weirs. The ineffective flow lines were added to show water passing over the high point of the bendway weir moved from the upstream eddy to the eddy downstream of the bendway weir. The flow that passes over this portion of the bendway weir is considered ineffective since it conforms to the downstream eddy.
Trial 12	Use base-line model to build bendway weirs by using the weir option in the HEC-RAS. Look at all flow rates with the same geometry file, **NOT** independently of one another.
Trial 13	Use Trial 12 and add ineffective flow lines upstream and downstream of bendway weirs as well as at the highest elevation of the bendway weir to locate areas influenced by the eddies.
Trial 14 (8 cfs)	Use Trial 13 and change Manning's n at all cross sections with bendway weirs. Change geometry specifically for 8 cfs, model run.
Trial 14 (12 cfs)	Use Trial 13 and change Manning's n at all cross sections with bendway weirs. Change geometry specifically for 12 cfs, model run.
Trial 14 (16 cfs)	Use Trial 13 and change Manning's n at all cross sections with bendway weirs. Change geometry specifically for 16 cfs, model run.
Trial 15 (8 cfs)	Use Trial 5 (8 cfs) model and adjust contraction/expansion coefficients at cross sections in the HEC-RAS model that helps shape profile. Change geometry specifically for 8 cfs, model run.
Trial 15 (12 cfs)	Use Trial 5 (12 cfs) model and adjust contraction/expansion coefficients at cross sections in the HEC-RAS model that helps shape profile. Change geometry specifically for 12 cfs, model run.
Trial 15 (16 cfs)	Use Trial 5 (16 cfs) model and adjust contraction/expansion coefficients at cross sections in the HEC-RAS model that helps shape profile. Change geometry specifically for 16 cfs, model run.
Trial 16 (8 cfs)	Use Trial 15 (8 cfs) and adjust Manning's n and contraction/expansion coefficients simultaneously at any cross section in the HEC-RAS model that helps shape profile. Change geometry specifically for 8 cfs, model run.
Trial 16 (12 cfs)	Use Trial 15 (12 cfs) and adjust Manning's n and contraction/expansion coefficients simultaneously at any cross section in the HEC-RAS model that helps shape profile. Change geometry specifically for 12 cfs, model run.
Trial 16 (16 cfs)	Use Trial 15 (16 cfs) and adjust Manning's n and contraction/expansion coefficients simultaneously at any cross section in the HEC-RAS model that helps shape profile. Change geometry specifically for 16 cfs, model run.

NOTE: Yellow shaded cells represent trials used in analysis.

5.3 LIMITATIONS TO ANALYSIS

Limitations were placed on the analysis in order to determine if basic HEC-RAS modeling features were feasible options in developing an optimal HEC-RAS model. Basic HEC-RAS features used in the analysis were:

1. Manning's *n*;
2. contraction coefficient; and
3. expansion coefficient.

Once limitations were established, trials defined in Section 5.2 were reevaluated for the initial bendway-weir analysis. From the trial list presented in Table 5.1, seven of the sixteen defined trials were selected for this analysis. Trials selected for this bendway-weir analysis were Trial 1, Trial 2, Trial 3, Trial 4, Trial 5, Trial 15, and Trial 16. These trials are highlighted in yellow in Table 5.1.

5.4 SELECTED HEC-RAS MODEL BASED ON LIMITATIONS TO ANALYSIS

In an attempt to achieve the bendway-weir analysis goal while abiding by the limitations outlined in Section 5.3, seven of the sixteen stated trials in Table 5.1 were developed into HEC-RAS models. Of the seven trials developed into HEC-RAS models, Trial 16 was selected as the best possible HEC-RAS model.

5.4.1 Trial 16 Input Tables

During Trial 16, Manning's *n* and the contraction and expansion coefficients were adjusted simultaneously until the flow depth calculated through the HEC-RAS model

reflected flow depths measured along the physical model. Input tables for Manning's *n* and the contraction and expansion coefficients are presented in Table 5.2 and Table 5.3, respectively. In Table 5.2 and Table 5.3, W1 through W5 are interpolated cross sections in HEC-RAS that represent five bendway-weir locations in the Type I bend. W6 through W8 are interpolated cross sections in HEC-RAS that represent three bendway-weir locations in the Type III bend. Values set for Manning's *n* and the contraction and expansion coefficients did not have to reflect what is typically considered "realistic" values for these variables. Manning's *n* and the contraction and expansion coefficients were the only variables used to represent a 3-D velocity profile in a 1-D model and, therefore, values used in HEC-RAS might be greater than values typically applied to 1-D HEC-RAS models.

Table 5.2. Trial 16 Manning's *n* Values

XS	$n_{8\ cfs}$	$n_{12\ cfs}$	$n_{16\ cfs}$
0 (U/S)	0.013	0.013	0.013
W1	0.013	0.013	0.100
1	0.038	0.013	0.025
2	0.013	0.038	0.025
W2	0.013	0.013	0.090
3	0.013	0.013	0.013
W3	0.013	0.013	0.013
4	0.013	0.013	0.013
5	0.013	0.013	0.013
W4	0.013	0.013	0.013
6	0.013	0.013	0.013
7	0.013	0.013	0.013
W5	0.013	0.013	0.013
8	0.013	0.013	0.013
9	0.013	0.013	0.013
10	0.013	0.013	0.020
11	0.036	0.036	0.035
W6	0.036	0.036	0.070
12	0.023	0.023	0.023
13	0.025	0.028	0.035
W7	0.025	0.028	0.035
14	0.013	0.013	0.013
15	0.013	0.013	0.013
16	0.035	0.030	0.013
W8	0.035	0.030	0.013
17	0.013	0.030	0.013
18 (D/S)	0.013	0.013	0.013

Table 5.3. Trial 16 Expansion and Contraction Coefficients

	8 cfs		12 cfs		16 cfs	
XS	C_c	C_e	C_c	C_e	C_c	C_e
0 (U/S)	0.1	0.3	0.1	0.3	0.1	0.3
W1	0.1	0.3	0.1	0.3	0.1	0.3
1	0.1	0.3	0.1	0.3	0.1	0.3
2	0.1	0.3	0.1	0.3	0.1	0.3
W2	0.1	0.3	0.1	0.3	0.1	0.3
3	0.1	0.3	0.1	0.3	0.1	0.3
W3	0.1	0.3	0.1	0.3	0.1	0.3
4	0.1	0.3	0.1	0.3	0.1	0.3
5	0.1	0.3	0.1	0.3	0.1	0.3
W4	0.1	0.3	0.1	0.3	0.1	0.3
6	0.1	0.3	0.1	0.3	0.1	0.3
7	0.1	0.3	0.1	0.3	0.1	0.3
W5	0.1	0.3	0.1	0.3	0.1	0.3
8	0.1	0.3	0.1	0.3	0.1	0.3
9	2.5	0.3	0.1	0.3	0.1	0.3
10	4	0.3	6.8	0.3	0.1	0.3
11	5.6	0.3	7.5	0.3	3.5	0.3
W6	0.1	0.3	0.1	0.3	0.3	0.3
12	0.1	0.3	0.1	0.3	0.1	0.3
13	0.1	0.3	1.8	0.3	0.1	0.3
W7	0.1	0.3	0.1	0.3	0.1	0.3
14	0.1	0.3	0.1	0.3	0.1	0.3
15	0.1	0.3	0.1	0.3	0.1	0.3
16	0.1	0.3	4.8	0.3	0.1	0.3
W8	0.1	0.3	5.0	0.3	0.1	0.3
17	0.1	0.3	0.1	0.3	0.1	0.3
18 (D/S)	0.1	0.3	0.1	0.3	0.1	0.3

5.4.2 Trial 16 Results

Trial 16 results used HEC-RAS output for computed water-surface elevations at all cross sections marked along the physical model. Flow depth and total energy loss estimates for Trial 16 were compared to measurements collected along the physical model.

5.4.2.1 Flow-depth Comparison

Water-surface elevations along the physical model were used to calculate flow depths at each marked cross section in the physical model. Flow-depth measurements were calculated at 8 cfs, 12 cfs, and 16 cfs with Equation 4.1. Results from Equation 4.1 are presented in Table 5.4.

Table 5.4. HEC-RAS Output Flow-depth Measurements

XS	$y_{8\ cfs}$ (ft)	$y_{12\ cfs}$ (ft)	$y_{16\ cfs}$ (ft)
0 (U/S)	0.693	0.880	1.001
W1	0.702	0.890	1.007
1	0.702	0.890	1.004
2	0.719	0.907	1.018
W2	0.718	0.906	1.013
3	0.717	0.905	1.010
W3	0.726	0.913	1.018
4	0.726	0.913	1.018
5	0.715	0.902	1.007
W4	0.714	0.901	1.006
6	0.723	0.911	1.015
7	0.732	0.920	1.024
W5	0.732	0.920	1.024
8	0.741	0.929	1.032
9	0.743	0.929	1.030
10	0.697	0.915	1.009
11	0.700	0.912	1.013
W6	0.656	0.873	0.969
12	0.643	0.862	0.949
13	0.632	0.856	0.932
W7	0.621	0.847	0.896
14	0.621	0.847	0.896
15	0.613	0.843	0.889
16	0.633	0.865	0.916
W8	0.609	0.844	0.913
17	0.609	0.802	0.919
18 (D/S)	0.614	0.802	0.924

Once flow-depth calculations were completed, results were compared to flow-depth measurements along the physical model. Figure 5.1 presents flow depths calculated by HEC-RAS and measured with the track-mounted point gage for each cross section along the physical model. As Figure 5.1 illustrates, there is an abrupt increase in flow depth between XS8 and XS9. An abrupt increase in flow depth is due to the contraction between the Type I and Type III bends. The contraction creates a backwater effect which advances into the Type I bend. The backwater effect becomes less significant as the flow rate increases from 8 cfs to 16 cfs and therein, HEC-RAS is able to produce more accurate estimates of flow depth.

Cross-sectional average flow depth ($\bar{y}$) estimates in the Type I and Type III bends were calculated using the measurements presented in Table 5.4 and Figure 5.1. When calculating cross-sectional average flow depth in each bend, XS1 through XS6 were taken into account for the Type I bend and XS11 through XS17 were taken into account for the Type III bend. Cross-sectional average flow-depth results are presented in Table 5.5. As Table 5.5 shows, the cross-sectional average flow depth estimated by HEC-RAS at 8 cfs is 0.718 ft in the Type I bend and cross-sectional average flow depth measured in the physical model is 0.698 ft, which is a difference of 0.020 ft. At 16 cfs, cross-sectional average flow depth estimated by HEC-RAS is 0.929 ft in the Type III bend and cross-sectional average flow depth measured in the physical model is 0.918 ft, which is a difference of 0.012 ft. Even though the flow-depth measurements estimated by HEC-RAS did not exactly match the flow-depth measurements in the physical model, Trial 16 was still selected as the best possible HEC-RAS model given the limitations to

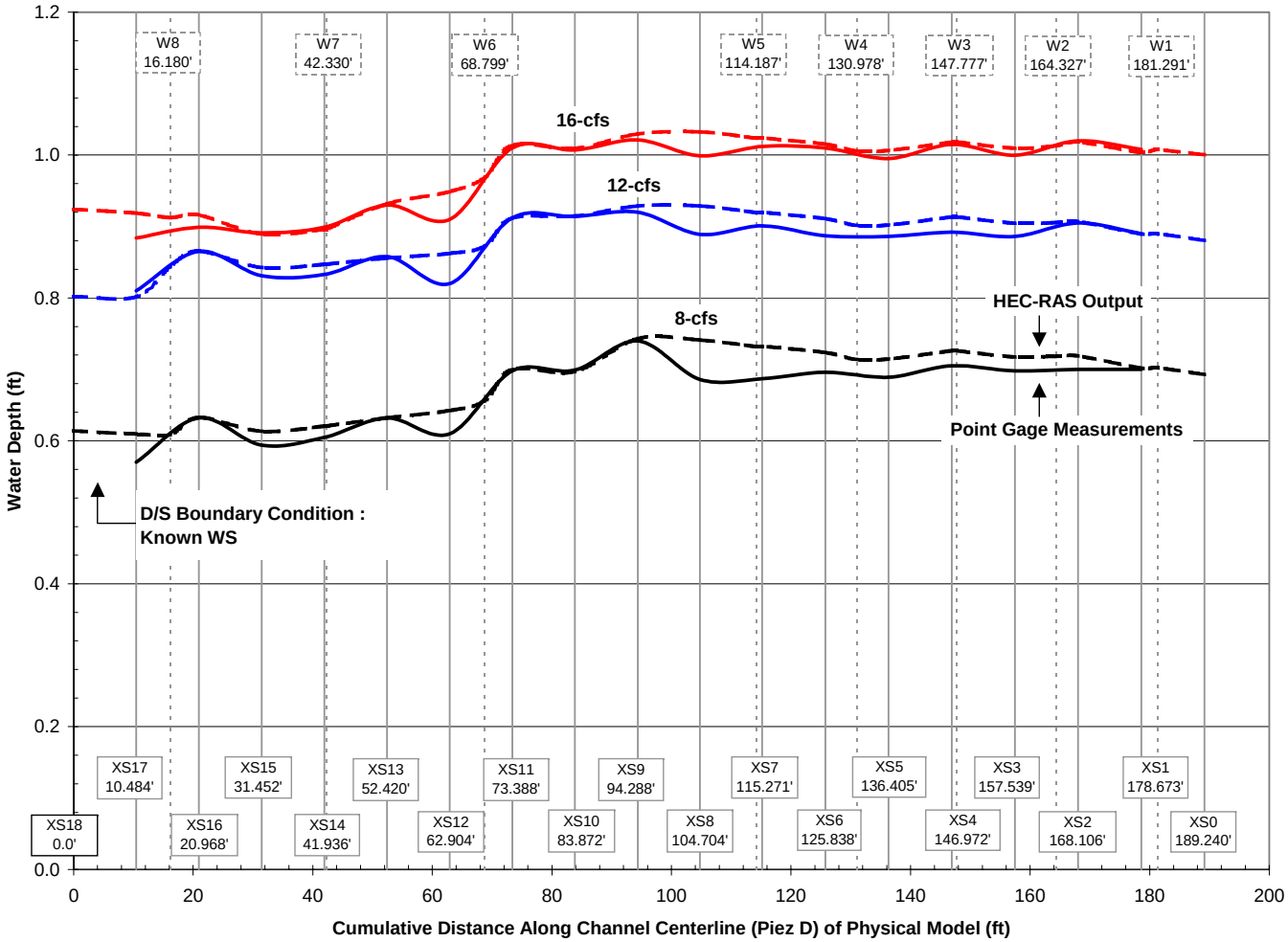

Figure 5.1. Comparison of Flow Depths Measured Along Physical Model and Estimated by HEC-RAS

the analysis. Once the flow depths were finalized, total energy and total energy loss were studied along the Type I and Type III bends.

Table 5.5. $\bar{y}$ in the Type I and Type III Bends

Bend	Physical Model Measurements			HEC-RAS Output		
	$\bar{y}_{8\ cfs}$ (ft)	$\bar{y}_{12\ cfs}$ (ft)	$\bar{y}_{16\ cfs}$ (ft)	$\bar{y}_{8\ cfs}$ (ft)	$\bar{y}_{12\ cfs}$ (ft)	$\bar{y}_{16\ cfs}$ (ft)
Type I (U/S) Bend	0.698	0.891	1.008	0.718	0.905	1.012
Type III (D/S) Bend	0.620	0.847	0.918	0.634	0.855	0.929

5.4.2.2 Trial 16 Total Energy Calculations

Total energy is calculated by summing the bed elevation, flow depth, and velocity head at a cross section. Equation 2.3 illustrated the equation used to calculate total energy at a cross section. In this analysis, total energy at each marked cross section along the physical model was calculated with physical model measurements and HEC-RAS output based on Equation 2.3. Table 5.6 presents the calculated total energy along the Type I and Type III bends using the physical model, flow-depth measurements.

Table 5.6. Total Energy Calculated With Physical Model Measurements

XS	$H_{8\ cfs}$ (ft)	$H_{12\ cfs}$ (ft)	$H_{16\ cfs}$ (ft)
0 (U/S)			
W1	97.990	98.190	98.318
1	97.953	98.147	98.270
2	97.933	98.141	98.262
W2	97.965	98.156	98.271
3	97.931	98.123	98.243
W3	97.926	98.113	98.230
4	97.928	98.119	98.247
5	97.923	98.123	98.238
W4	97.948	98.144	98.252
6	97.920	98.114	98.242
7	97.901	98.118	98.234
W5	97.916	98.128	98.240
8	97.890	98.096	98.212
9	97.937	98.123	98.232
10	97.910	98.129	98.235
11	97.889	98.107	98.217
W6	97.876	98.068	98.177
12	97.813	98.026	98.132
13	97.823	98.050	98.140
W7	97.849	98.045	98.135
14	97.789	98.017	98.103
15	97.780	98.015	98.097
16	97.783	98.016	98.075
W8	97.821	98.020	98.101
17	97.721	97.957	98.051
18 (D/S)			

Once total energy was calculated with physical model measurements, total energy was estimated with HEC-RAS output. Using the flow depths presented in Table 5.4, total energy was estimated along the physical model. Results are presented in Table 5.7. Total energy estimates throughout the physical model were used to estimate total energy loss along the Type I and Type III meander bends.

Table 5.7. Total Energy Calculated With HEC-RAS Output

XS	$H_{8\ cfs}$ (ft)	$H_{12\ cfs}$ (ft)	$H_{16\ cfs}$ (ft)
0 (U/S)	97.957	98.148	98.273
W1	97.956	98.147	98.269
1	97.955	98.146	98.266
2	97.952	98.143	98.260
W2	97.951	98.142	98.255
3	97.950	98.141	98.252
W3	97.949	98.140	98.251
4	97.949	98.140	98.251
5	97.947	98.139	98.249
W4	97.947	98.138	98.248
6	97.946	98.137	98.247
7	97.945	98.136	98.246
W5	97.945	98.136	98.245
8	97.943	98.134	98.244
9	97.941	98.132	98.241
10	97.907	98.129	98.236
11	97.892	98.108	98.222
W6	97.853	98.073	98.183
12	97.841	98.063	98.165
13	97.823	98.048	98.142
W7	97.804	98.031	98.103
14	97.803	98.030	98.102
15	97.797	98.026	98.096
16	97.784	98.017	98.090
W8	97.765	97.999	98.087
17	97.757	97.954	98.084
18 (D/S)			

5.4.2.3 Total Energy Loss Calculation

Total energy loss in an open channel system is defined as a loss of energy along a channel reach due to friction, contractions, expansions, eddies, spiral, and secondary currents. An exception to this definition is in 1-D, steady-state, gradually-varied flow analysis, where total energy loss is assumed to be due to friction, contraction, and expansion losses. Typically, contraction and expansion loss is small compared to the

friction loss and, therefore, the total energy loss is assumed approximately equal to the friction loss along a reach. In this analysis, total energy loss along the Type I and Type III bends is estimated with the EGL. The energy grade line is defined by Equation 5.1:

$$h_T = \frac{H_2 - H_1}{\Delta x} \qquad \textbf{Equation 5.1}$$

where:

Δx = distance along the centerline of the channel between cross sections (ft);

h_T = total energy loss through meander bend (ft);

H_1 = total energy at the downstream cross section (ft); and

H_2 = total energy at the upstream cross section (ft).

The EGL, also known as energy grade line slope, is used to estimate total energy loss by multiplying the EGL by the channel centerline distance. In this analysis, the EGL was calculated by plotting the total energy calculated along the Type I and Type III bends verses cumulative distance along the channel centerline and estimating the slope through linear interpolation. Using physical model measurements and HEC-RAS output, Figure 5.2 illustrates how the EGL was estimated through linear interpolation. Similar plots generated for 12 cfs and 16 cfs are presented in Appendix C.

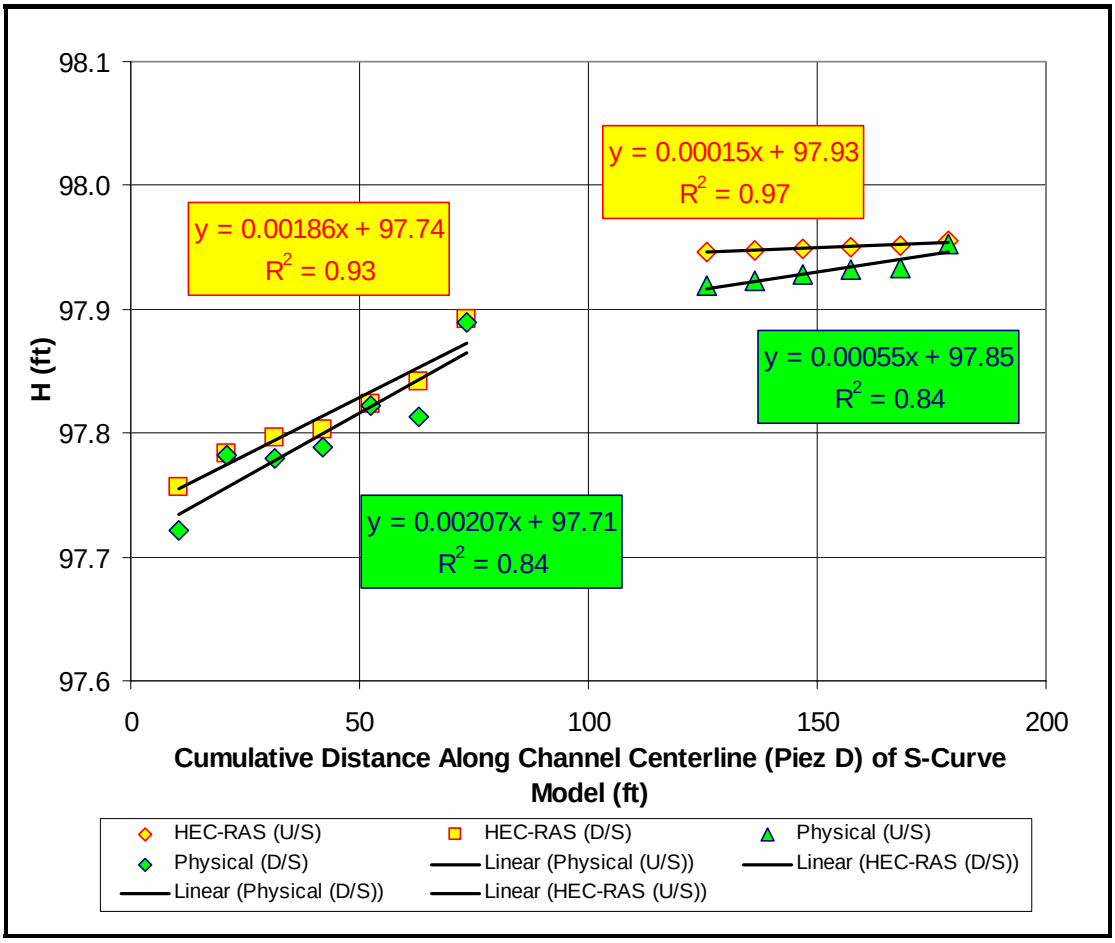

Figure 5.2. Linear Interpolation at 8 cfs

Total energy loss through a meander bend along the Type I and Type III bends was calculated with physical model measurements and HEC-RAS output. Results are presented in Table 5.8. As observed in Table 5.8, there is a significant discrepancy between total energy loss through a meander bend estimated from HEC-RAS output and the physical model measurements. The discrepancy is more significant in the Type I bend than in the Type III bend, with an average 60% difference between the actual total energy loss through a meander bend in the physical model and total energy loss through a meander bend estimated from HEC-RAS output. A possible reason for this discrepancy is the defined radius of curvature in the Type I and Type III bends. In the Type I bend,

the radius of curvature is equal to 38.75 ft and in the Type III bend, the radius of curvature is equal to 65.83 ft. As the radius of curvature tightens from the Type III bend to the Type I bend, the spiral and secondary currents become more significant and produce greater energy loss. This energy loss is evident by the comparison made in Table 5.8. Since spiral currents and secondary currents are neglected in 1-D flow computations such as HEC-RAS, additional analysis was performed to better estimate total energy loss through a meander bend through the Type I and Type III meander bends with HEC-RAS.

Table 5.8. h_T Comparison

Bend	Q (cfs)	h_T (ft)		Absolute Δ (%)
		Physical Model	HEC-RAS Model	
Type I	8	0.0291	0.0079	73
	12	0.0317	0.0085	73
	16	0.0296	0.0180	39
Type III	8	0.1302	0.1170	10
	12	0.1296	0.1233	5
	16	0.1573	0.1308	16

CHAPTER 6 MINOR LOSS CALCULATIONS

Minor losses represent sources of energy depletion along a reach that are not related to friction loss. For example, minor losses are energy losses related to expansions and contractions along a reach, secondary currents, spiral currents, and eddies.

6.1 PURPOSE OF ANALYSIS

As presented in Chapter 5, it was determined that HEC-RAS underestimated total energy loss through a meander bend in the Type I bend by an average 60% and in the Type III bend by approximately 7%. A possible reason for the discrepancy between calculations resulting from physical model measurements and HEC-RAS output is the possibility that HEC-RAS does not account for certain minor losses. HEC-RAS accounts for minor losses due to expansions and contractions along a reach but it does not account for minor losses due to eddies, spiral, and secondary currents. In order to study the significance of minor loss not accounted for in HEC-RAS, a study was completed for the base-line analysis. Minor losses not accounted for during the base-line analysis were secondary and spiral currents. Minor losses due to secondary and spiral currents are known as minor loss due to a meander bend through the rest of the analysis.

6.2 MINOR LOSS DUE TO MEANDER BEND CALCULATIONS

A procedure was developed to calculate minor losses due to a meander bend along the physical model at 8 cfs, 12 cfs, and 16 cfs. The procedure used a series of spreadsheets to determine average velocity, total energy, and friction loss at each cross section. After the average velocity, total energy, and friction loss were calculated at each cross section, total energy loss through each meander bend was calculated along the Type I and Type III bends. Total energy loss through each meander bend was the final variable needed to determine minor loss due to meander bend. The series of spreadsheets is presented later in more detail.

6.3 RESULTS FROM MINOR LOSS DUE TO MEANDER BEND CALCULATIONS

In order to calculate minor loss due to a meander bend, a series of spreadsheets was used to calculate average velocity, total energy, and friction loss at each cross section and total energy loss through each meander bend. This analysis was performed for discharges of 8 cfs, 12 cfs, and 16 cfs.

6.3.1 Average Velocity Results

Average velocity ($\bar{v}$) at each cross section was calculated using Equation 2.2. Results using Equation 2.2 are shown in Table 6.1 for discharges of 8 cfs, 12 cfs, and 16 cfs. Cross-sectional geometry in the Type I and Type III bends was assumed to be trapezoidal.

Table 6.1. $\bar{v}$ Results

XS	$\bar{v}_{8\ cfs}$ (ft/s)	$\bar{v}_{12\ cfs}$ (ft/s)	$\bar{v}_{16\ cfs}$ (ft/s)
0 (U/S)	1.10	1.15	1.32
1	1.13	1.18	1.34
2	1.10	1.17	1.32
3	1.09	1.17	1.34
4	1.10	1.16	1.33
5	1.13	1.19	1.35
6	1.12	1.17	1.33
7	1.09	1.17	1.33
8	1.11	1.14	1.32
9	1.34	1.39	1.58
10	1.73	1.78	2.01
11	1.75	1.77	2.01
12	1.76	1.77	2.03
13	1.76	1.81	2.05
14	1.74	1.75	2.00
15	1.78	1.76	2.03
16	1.70	1.72	1.99
17	1.69	1.69	1.96
18 (D/S)	1.63	1.65	1.92

6.3.2 Total Energy Loss Results

Once average velocity was calculated at each cross section, total energy at each cross section (*H*) was calculated with Equation 2.3. Table 6.2 presents total energy loss for discharges of 8 cfs, 12 cfs, and 16 cfs. Estimates of total energy at each cross section were used to determine the EGL along the Type I and Type III bends.

Table 6.2. *H* Results

XS	$H_{8\ cfs}$ (ft)	$H_{12\ cfs}$ (ft)	$H_{16\ cfs}$ (ft)
0 (U/S)	97.88	98.09	98.21
1	97.85	98.06	98.19
2	97.84	98.05	98.17
3	97.85	98.05	98.17
4	97.83	98.04	98.16
5	97.83	98.04	98.16
6	97.82	98.04	98.16
7	97.83	98.03	98.16
8	97.81	98.04	98.15
9	97.81	98.03	98.15
10	97.82	98.03	98.15
11	97.79	98.01	98.13
12	97.79	98.01	98.12
13	97.79	98.00	98.12
14	97.78	98.00	98.11
15	97.77	97.99	98.11
16	97.76	97.98	98.10
17	97.75	97.97	98.09
18 (D/S)	97.75	97.97	98.08

In order to determine the EGL along each bend, total energy at each cross section was plotted against the cumulative channel distance through the physical model starting at XS18. A linear trend line was interpolated for the plotted series and the slope of the linear trend line was equal to the EGL. Figure 6.1 through Figure 6.3 illustrate graphs used to calculate the EGL at discharges of 8 cfs, 12 cfs, and 16 cfs.

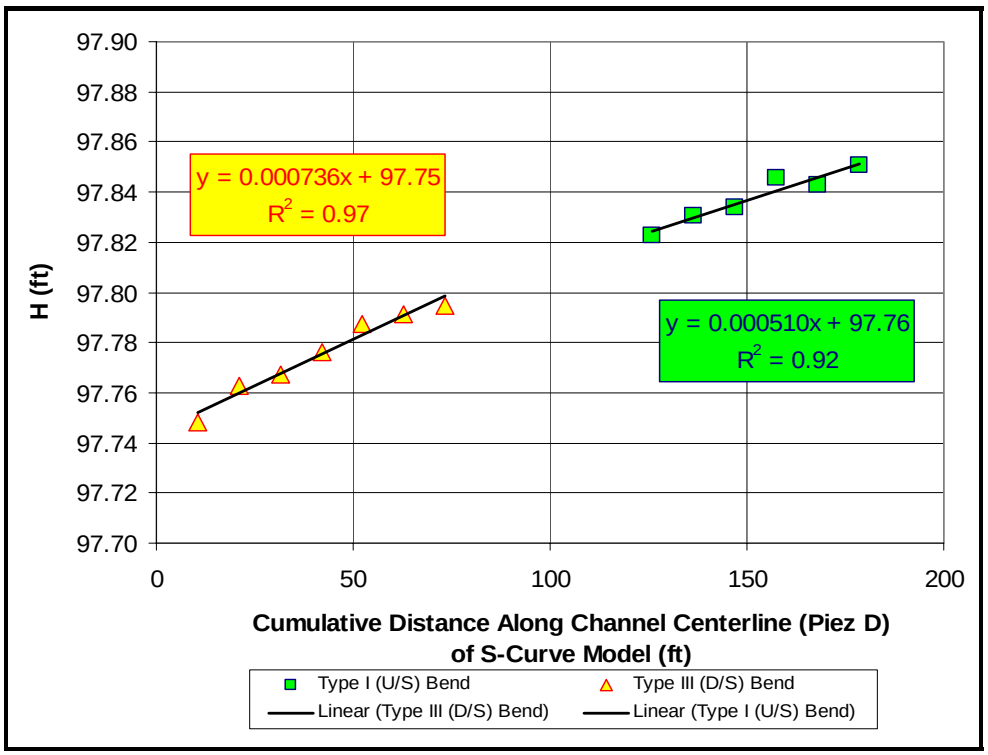

Figure 6.1. Linear Interpolation of Total Energy at 8 cfs

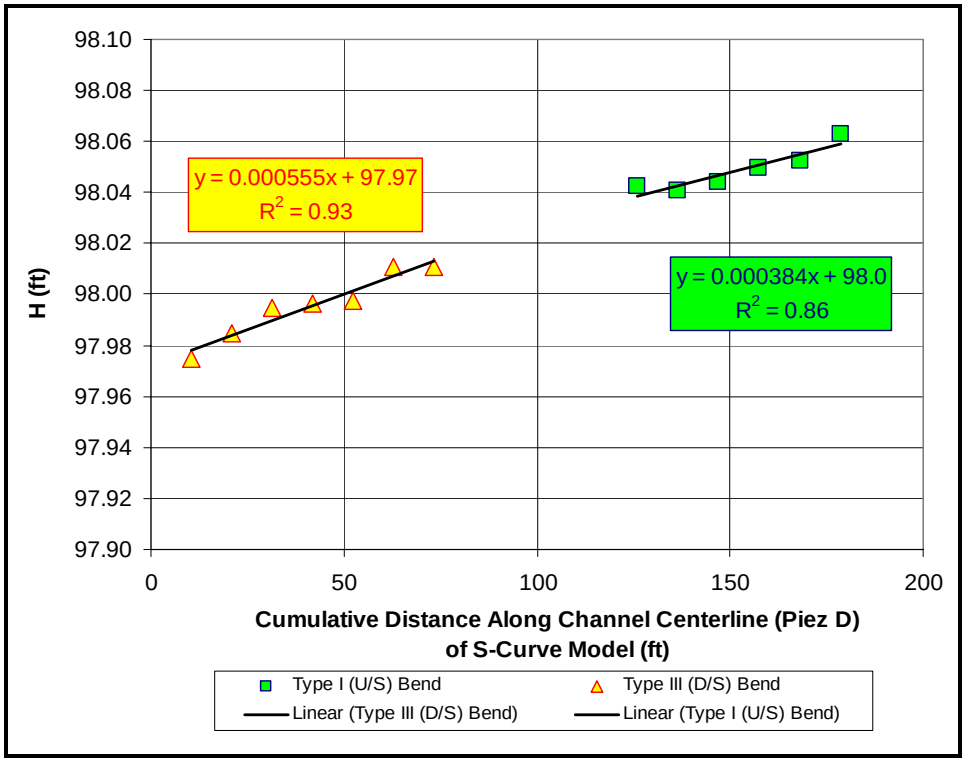

Figure 6.2. Linear Interpolation of Total Energy at 12 cfs

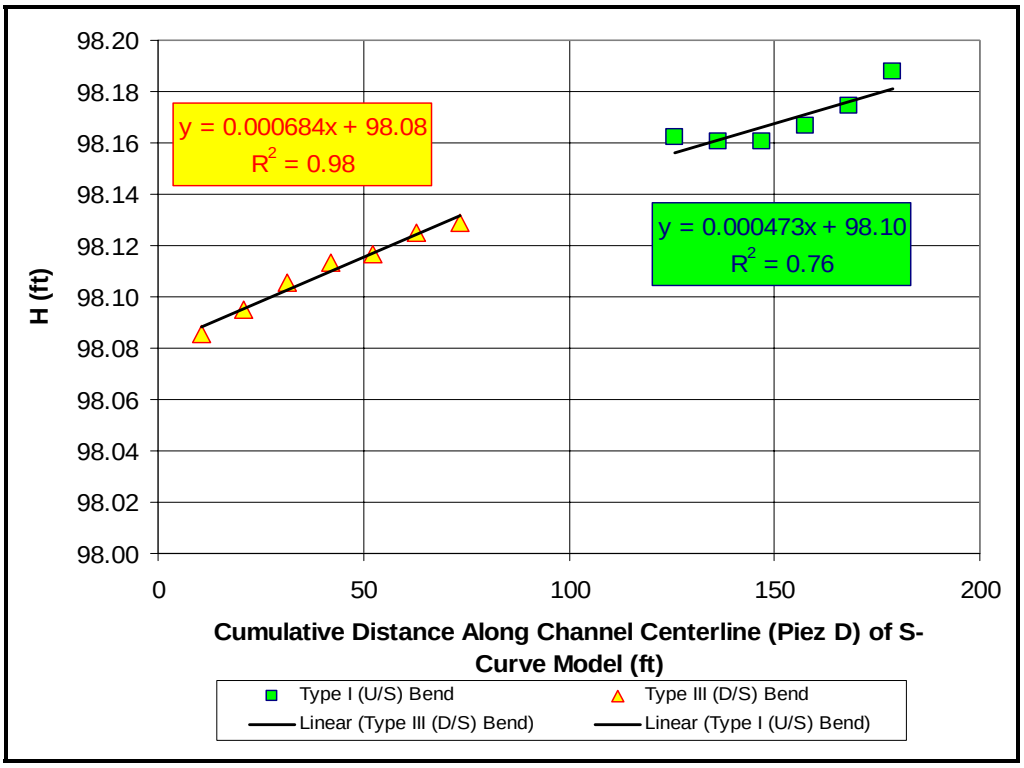

Figure 6.3. Linear Interpolation of Total Energy at 16 cfs

The EGL was used to calculate the average total energy loss between adjacent cross sections ($\bar{h}_t$) in the Type I and Type III bends. Average total energy loss between adjacent cross sections was calculated by multiplying the linear interpolated EGL by the distance between adjacent cross section in the Type I and Type III bends. Table 6.3 presents average total energy loss between adjacent cross sections for discharges of 8 cfs, 12 cfs, and 16 cfs. Average total energy loss between adjacent cross sections was used in the final computation for calculating minor loss due to the meander bends.

Table 6.3. $\bar{h}_t$ Results

Bend	Q (cfs)	Distance Between XS (ft)	EGL (ft/ft)	$\bar{h}_t$ (ft)
Type I (U/S) Bend	8	10.567	0.000510	0.0054
	12		0.000384	0.0041
	16		0.000473	0.0050
Type III (U/S) Bend	8	10.484	0.000736	0.0077
	12		0.000555	0.0058
	16		0.000684	0.0072

6.3.3 Friction Loss Results

Average friction loss between adjacent cross sections (h_{Sf}) was calculated by the average conveyance method. Average conveyance method, defined in Equation 2.10, was the equation used to calculate average friction loss between adjacent cross sections in this analysis since it is the default method in HEC-RAS. Results of average friction loss between adjacent cross sections are shown in Table 6.4 for discharges of 8 cfs, 12 cfs, and 16 cfs. Intuitively, average friction loss between adjacent cross sections in the Type I or Type III bends should be fairly uniform along a prismatic, concrete, rigid boundary, meander bend. This assumption is reflected by the average friction loss between adjacent cross sections calculated in the Type I and Type III bends. For instance, average friction losses between adjacent cross sections results presented in Table 6.4 show similar results for XS0 through XS7.

Table 6.4. h_{Sf} Results

XS	$h_{Sf\,8cfs}$ (ft)	$h_{Sf\,12cfs}$ (ft)	$h_{Sf\,16cfs}$ (ft)
0 (U/S)	0.0024	0.0019	0.0021
1	0.0024	0.0019	0.0021
2	0.0023	0.0019	0.0021
3	0.0023	0.0019	0.0021
4	0.0024	0.0019	0.0022
5	0.0025	0.0019	0.0022
6	0.0024	0.0019	0.0021
7	0.0024	0.0018	0.0021
8	0.0029	0.0022	0.0025
9	0.0047	0.0036	0.0040
10	0.0066	0.0049	0.0055
11	0.0068	0.0049	0.0056
12	0.0069	0.0050	0.0057
13	0.0068	0.0049	0.0056
14	0.0069	0.0048	0.0055
15	0.0066	0.0046	0.0055
16	0.0061	0.0044	0.0052
17	0.0058	0.0042	0.0050
18 (D/S)			

Since the average friction loss is fairly uniform in the Type I and Type III meander bends, a cross-sectional average, average friction loss ($\overline{h}_{Sf}$) was calculated for the Type I and Type III meander bends. Table 6.5 presents cross-sectional average, average friction loss for the Type I and Type III bends for discharges of 8 cfs, 12 cfs, and 16 cfs. Cross-sectional average, average friction loss was used in the final spreadsheet computation for calculating minor loss due to the meander bends.

Table 6.5. $\bar{h}_{Sf}$ Results

Bend	Q (cfs)	$\bar{h}_{Sf}$ (ft)
Type I (U/S) Bend	8	0.0024
	12	0.0019
	16	0.0021
Type III (U/S) Bend	8	0.0066
	12	0.0047
	16	0.0054

6.3.4 Minor Loss Due To Meander Bend Results

Once average total energy loss between adjacent cross sections and cross-sectional average, average friction loss were determined, a spreadsheet analysis was needed to calculate the cross-sectional average minor loss due to meander bends ($\bar{h}_{BEND}$). Cross-sectional average minor loss due to meander bends is calculated by the following equation:

$$\bar{h}_{BEND} = \bar{h}_t - \bar{h}_{Sf} \qquad \textbf{Equation 6.1}$$

where:

$\bar{h}_{BEND}$ = cross-sectional average minor loss due to meander bend (ft);

$\bar{h}_{Sf}$ = cross-sectional average, average friction loss (ft); and

$\bar{h}_t$ = cross-sectional average total energy loss (ft).

Equation 6.1 assumes that minor loss due to expansions and contractions is negligible compared to the energy loss due to friction and meander bends. Table 6.6 presents the calculations of cross-sectional average minor loss due to meander bends for the Type I and Type III bends at discharges of 8 cfs, 12 cfs, and 16 cfs.

Table 6.6. $\bar{h}_{BEND}$ Results

Bend	Q (cfs)	Distance Between XS (ft)	Energy Grade Line (ft/ft)	$\bar{h}_t$ (ft)	$\bar{h}_{Sf}$ (ft)	$\bar{h}_{BEND}$ (ft)
Type I (U/S) Bend	8	10.567	0.000510	0.0054	0.0024	**0.0030**
	12		0.000384	0.0041	0.0019	**0.0021**
	16		0.000473	0.0050	0.0021	**0.0029**
Type III (U/S) Bend	8	10.484	0.000736	0.0077	0.0066	**0.0012**
	12		0.000555	0.0058	0.0047	**0.0011**
	16		0.000684	0.0072	0.0054	**0.0017**

Once cross-sectional average minor loss due to meander bends was calculated, it was important to determine the average minor loss due to meander bends through the meander bend ($\bar{h}_{BEND-TOTAL}$); in this case, through the Type I and Type III bends. Average minor loss due to meander bends through a meander bend was calculated by the following equation:

$$\bar{h}_{BEND-TOTAL} = \bar{h}_{BEND} * \left(XS_{TOTAL} - 1\right) \qquad \textbf{Equation 6.2}$$

$\bar{h}_{BEND}$ = average minor loss due to a meander bend between adjacent cross sections (ft);

$\bar{h}_{BEND-TOTAL}$ = average minor loss due to the meander bend through the bend (ft); and

XS_{TOTAL} = number of significant cross sections used in analysis.

Six cross sections were used in the Type I bend and seven cross sections were used in the Type III bend to calculate Equation 6.2. In the Type I bend, eight cross sections are marked along the physical model but XS0, XS7, and XS8 were excluded from the calculation in order to eliminate the influence from the head box and transition section. In the Type III bend, eight cross sections are marked along the physical model but XS10 and XS18 were excluded from the calculation in order to eliminate the influence from the

transition section and the stop logs. Results of average minor loss due to meander bends through a meander bend is shown in Table 6.7 for discharges of 8 cfs, 12 cfs, and 16 cfs.

Table 6.7. $\bar{h}_{BEND\text{-}TOTAL}$ Results

Bend	Q (cfs)	$\bar{h}_{BEND}$ (ft)	Number of Cross Sections	$\bar{h}_{BEND-TOTAL}$ (ft)
Type I (U/S) Bend	8	0.0030	6	0.0149
	12	0.0021	6	0.0107
	16	0.0029	6	0.0143
Type III (U/S) Bend	8	0.0012	7	0.0069
	12	0.0011	7	0.0068
	16	0.0017	7	0.0104

This technique was also used to determine the average friction loss through the meander bend ($\bar{h}_{Sf-TOTAL}$) and the average total energy loss through the meander bend ($\bar{h}_T$). Once these values were calculated, it was important to determine how significant average minor loss due to a meander bend through each meander bend was to the average total energy loss through the bend computation. Percent energy loss due to average minor loss due to a meander bend through each meander bend is presented in Table 6.8. Table 6.8 shows that at 16 cfs, average minor loss due to a meander bend through each meander bend is 57% of average total energy loss through the meander bend in the Type I bend. In the Type III bend the percentage is not as high but it still estimates that 24% percent of average total energy loss through the meander bend in the Type III bend is due to average minor loss due to a meander bend through each bend. Since 57% of average total energy loss through the meander bend is due to average minor loss due to a meander bend through the bend in the Type I bend and 24% of average total energy loss through the meander bend is due to average minor loss due to a meander bend through the

meander bend in the Type III bend, it is evident that spiral and secondary currents are significant in total energy loss calculations. The difference between the percentage of energy loss due to the meander bend in the Type I bend versus the Type III bend demonstrates that the radius of curvature in each bend plays a significant role in determining average minor loss due to a meander bend through each meander bend.

Table 6.8. Percent Energy Loss Due to $\bar{h}_{BEND\text{-}TOTAL}$

Bend	Q (cfs)	$\bar{h}_T$ (ft)	$\bar{h}_{Sf-TOTAL}$ (ft)	$\bar{h}_{BEND-TOTAL}$ (ft)	% Energy Loss Due to $\bar{h}_{BEND-TOTAL}$
Type I (U/S) Bend	8	0.0269	0.0121	0.0149	**55**
	12	0.0203	0.0096	0.0107	**53**
	16	0.0250	0.0107	0.0143	**57**
Type III (U/S) Bend	8	0.0463	0.0394	0.0069	**15**
	12	0.0349	0.0281	0.0068	**20**
	16	0.0430	0.0326	0.0104	**24**

6.4 CONCLUSION

Since this analysis demonstrated that average minor loss due to meander bends through a meander bend was significant in the physical model, a technique needed to be developed in order to calculate average minor loss due to meander bends through a meander bend with HEC-RAS output. One such technique was developed in order to examine flow in a bend prior to adding structures. This technique is further discussed in Chapter 7.

CHAPTER 7 METHODS TO PREDICT MINOR LOSS DUE TO MEANDER BENDS

In order to better estimate cross-sectional average total energy loss ($\bar{h}_t$) given HEC-RAS output, a method needed to be developed to predict cross-sectional average minor loss due to a meander bend ($\bar{h}_{BEND}$). Predictor methods aid understanding of the relationship between geometry of a meander bend and discharge through a meander bend through an equation. During this analysis, a predictor method was developed to calculate cross-sectional average minor loss due to a meander bend. This method established a relationship between minor loss due to a meander bend and a pi term. The pi term was a dimensionless ratio relating external, material, and channel properties during the base-line analysis. Detailed methodology is discussed in the succeeding sections.

7.1 DEVELOPMENT OF THE METHOD

A method was established to calculate cross-sectional average minor loss due to a meander bend in order to estimate cross-sectional average total energy loss and, therefore, average total energy loss through a meander bend ($\bar{h}_T$) given HEC-RAS output. This method used a dimensionless pi term to establish a relationship with the ratio, $\bar{h}_{BEND}/\bar{h}_{Sf}$. A dimensionless relationship allowed the method developed with the

physical model to be used outside the laboratory and in natural river systems. Steps used to formulate a significant pi term are discussed in Section 7.1.1.

7.1.1 Development of a Pi Term

To develop a pi term demonstrating a significant relationship to the observed $\bar{h}_{BEND}/\bar{h}_{Sf}$, various pi terms were developed as a function of material, channel, and external properties. Variables that define material, channel, and external properties are outlined in Table 7.1.

Table 7.1. Variables Describing Dimensionless Pi Terms

Material Properties		
Symbol	Definition	Dimensions
υ	Kinematic Viscosity of Water	L^2/T
ρ	Density of Water	M/L^3
μ	Dynamic Viscosity of Water	$M\text{-}T/L^2$

Channel Properties		
Symbol	Definition	Dimensions
S_o	Bed Slope	
TW	Top Width	L
r_c	Radius of Curvature	L
L_b	Length of Channel Bend Along Centerline	L
y	Flow Depth	L
BW	Base Width	L
A	Cross-sectional Area	L^2
n	Manning's Roughness	

External Properties		
Symbol	Definition	Dimensions
Q	Discharge	L^3/T
g	Acceleration of Gravity	L/T^2

In this analysis, twenty-three pi terms were developed to determine a pi term that displayed a significant relationship with the observed $\bar{h}_{BEND}/\bar{h}_{Sf}$. Table 7.2 lists the twenty-three pi terms developed for this analysis.

Table 7.2. Relationships Describing Each Pi Term

Pi Term	Pi Term Relationship	Pi Term	Pi Term Relationship
π_1	$(r_c/TW)^2 / (Fr * 10)$	π_{13}	$(g * TW^2 * BW^2 * r_c / Q * \upsilon) * (S_o / 10^6)$
π_2	Fr	π_{14}	$(Q / (\upsilon * TW * BW)) * S_o$
π_3	$(TW / r_c) * S_o$	π_{15}	$(Q / (\upsilon * (TW - y_{PG}) * BW)) * S_o$
π_4	TW / y_{PG}	π_{16}	$(\upsilon * y_{PG} * r_c) / Q$
π_5	r_c / TW	π_{17}	π_6^{-1}
π_6	$(r_c / BW) * (y_{PG} / TW) * 100$	π_{18}	π_7^{-2}
π_7	$[(r_c / BW) * (y_{PG} / TW) * 100] * Fr$	π_{19}	π_9^{-1}
π_8	$(r_c / BW) * (S_o / Fr)$	π_{20}	$Q / (g^{1/2} * r_c^{1.5} * y_{PG})$
π_9	$(TW / BW) * S_o * 1000$	π_{21}	$(g^{1/2} * r_c^{1.5}) / v_{AVG}$
π_{10}	$(r_c / L_b) * (TW / BW)$	π_{22}	$\pi_2 * \pi_{20}$
π_{11}	r_c / y_{PG}	π_{23}	$\pi_{22} * (L_b / y_{PG})$
π_{12}	$(Q * \upsilon) / (g * TW^2 * BW^2 * r_c)$		

In order to compare the twenty-three pi terms outlined in Table 7.2, the subsequent methodology is followed:

1. Plot observed $\bar{h}_{BEND}/\bar{h}_{Sf}$ vs. π in Microsoft® Excel;
2. Determine a trend line using graphical functions in Microsoft® Excel that interpolates a significant relationship between observed $\bar{h}_{BEND}/\bar{h}_{Sf}$ and π;
3. Use equation defining interpolated trend line to calculate predicted $\bar{h}_{BEND}/\bar{h}_{Sf}$;

4. Calculate percent error and absolute percent error between predicted $\bar{h}_{BEND}/\bar{h}_{Sf}$ and observed $\bar{h}_{BEND}/\bar{h}_{Sf}$;
5. Plot observed $\bar{h}_{BEND}/\bar{h}_{Sf}$ vs. predicted $\bar{h}_{BEND}/\bar{h}_{Sf}$ to observe linear relationship;
6. Rank pi terms according to calculated percent error and absolute percent error; and
7. Select most significant π.

Appendix D illustrates Step 1 through Step 5 for π_5. From the list of 23 pi terms, π_5 demonstrated the most significant relationship to the observed $\bar{h}_{BEND}/\bar{h}_{Sf}$. Equation 7.1 notes the dimensionless relationship established in π_5:

$$\pi_5 = \frac{r_c}{\overline{TW}} \qquad \textbf{Equation 7.1}$$

where:

π_5 = dimensionless term;

r_c = radius of curvature (ft); and

$\overline{TW}$ = cross-sectional average top width (ft).

Once π_5 was selected as the most significant pi term, the graphical relationship was used to calculate the predicted cross-sectional average minor loss due to a meander bend. The graphical relationship established for π_5 is discussed in the succeeding section.

7.1.2 Graphical Relationship

A graphical relationship was established which showed a significant correlation between π_5 and observed $\bar{h}_{BEND}/\bar{h}_{Sf}$. This relationship is illustrated in Figure 7.1. As

Figure 7.1 illustrates, the graphical relationship between π_5 and observed $\bar{h}_{BEND}/\bar{h}_{Sf}$ was formulated by interpolating an exponential trend line in Microsoft® Excel. Equation 7.2 presents the numerical relationship of the exponential trend line:

$$\frac{\bar{h}_{BEND}}{\bar{h}_{Sf}} = 4.0e^{-0.45\pi_5} \qquad \textbf{Equation 7.2}$$

where:

$\bar{h}_{BEND}$ = cross-sectional average minor loss due to meander bend (ft);

$\bar{h}_{Sf}$ = cross-sectional average, average friction loss (ft); and

π_5 = dimensionless term.

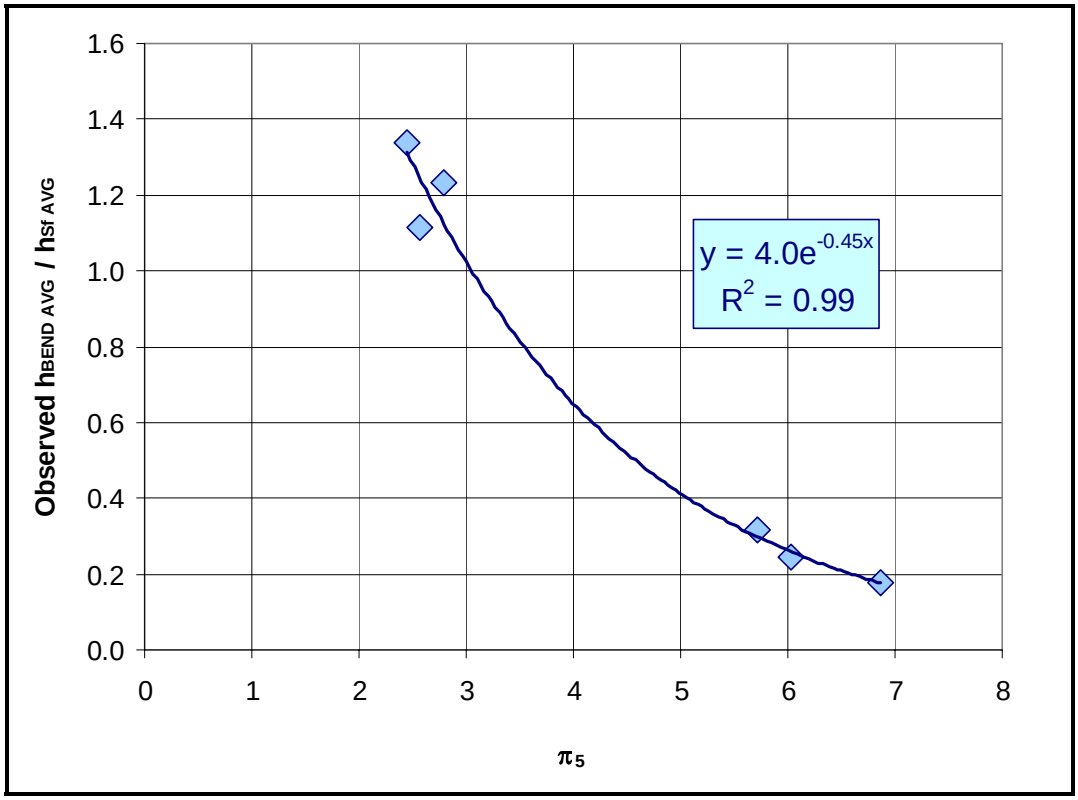

Figure 7.1. Graphical Relationship Between π_5 and Observed $\bar{h}_{BEND}/\bar{h}_{Sf}$

The relationship developed in Equation 7.2 was used to calculate cross-sectional average minor loss due to a meander bend with Equation 7.3:

$$\bar{h}_{BEND} = \bar{h}_{Sf}\left(\frac{\bar{h}_{BEND}}{\bar{h}_{Sf}}\right) \qquad \textbf{Equation 7.3}$$

where:

$\bar{h}_{BEND}$ = cross-sectional average minor loss due to meander bend (ft); and

$\bar{h}_{Sf}$ = cross-sectional average, average friction loss (ft).

Once Equation 7.1 through Equation 7.3 were established, a methodology was developed in order to outline the steps required to predict cross-sectional average minor loss due to a meander bend. This method was referred to as the π_5 method and is outlined in Section 7.1.3.

7.1.3 π_5 Method Used to Calculate Predicted $\bar{h}_{BEND}$

A method was needed to predict cross-sectional average minor loss due to a meander bend based on Equation 7.1 through Equation 7.3. The method is outlined as follows:

1. Define project area:
    a. location of study reach;
    b. type of river; and
    c. length of river.
2. Collect appropriate data during site assessment:
    a. Cross-sectional survey;
    b. Thalweg survey along meander bend;

c. Roughness coefficients:

   i. channel;

   ii. left overbank; and

   iii. right overbank.

d. Note channel contractions or expansions along meander bend.

e. Perform the following tasks **IF** time and equipment permits:

   i. record cross-sectional average discharge at each cross section;

   ii. flow-depth measurements along thalweg; and

   iii. flow-depth measurements downstream of meander bend.

3. If time and equipment **DID NOT** permit collecting data in Step 2, Part e:

   a. collect stage vs. discharge record for study reach.

4. Build HEC-RAS model with data collected during site assessment.

5. Run HEC-RAS model.

6. Use data collected during Step 2, Part e OR Step 3 to check that HEC-RAS accurately predicts flow depths through study reach.

7. Calculate $\overline{TW}$:

   a. copy top width estimates from HEC-RAS output table into Microsoft® Excel; and

   b. calculate $\overline{TW}$ through meander bend.

8. Estimate r_c with aerial photographs.

9. Calculate π_5.

10. Estimate $\overline{h}_{BEND} / \overline{h}_{Sf}$ with relationship presented in Equation 7.2.

11. Calculate $\overline{h}_{BEND}$:

a. copy h_{Sf} estimates from HEC-RAS output table into Microsoft® Excel;

b. calculate $\bar{h}_{Sf}$ through meander bend; and

c. calculate $\bar{h}_{BEND}$ with Equation 7.3.

Based on this methodology, results for predicted cross-sectional average minor loss due to a meander bend in the Type I and Type III bends are shown in Table 7.3 at discharges of 8 cfs, 12 cfs, and 16 cfs. Results of cross-sectional average minor loss due to a meander bend are used in Section 7.2 to determine cross-sectional average total energy loss.

Table 7.3. $\bar{h}_{BEND}$ Results Using π_5 Method

Bend	Q (cfs)	$\bar{h}_{BEND}$ (ft)
Type I (U/S) Bend	8	0.0028
	12	0.0025
	16	0.0029
Type III (D/S) Bend	8	0.0012
	12	0.0013
	16	0.0017

Steps used in the π_5 method determined cross-sectional average minor loss due to a meander bend. In order to calculate average minor loss due to a meander bend through a meander bend ($\bar{h}_{BEND-TOTAL}$), use Equation 6.2.

7.2 TOTAL ENERGY LOSS CALCULATION

Ultimately, the goal of this analysis is to accurately calculate the average total energy loss through a meander bend using HEC-RAS output. The π_5 method stated in Section 7.1.3 determined the predicted cross-sectional average minor loss due to a meander bend and these results are used in the calculation for cross-sectional average

total energy loss and average total energy loss through the meander bend ($\bar{h}_T$). Cross-sectional average total energy loss is calculated with Equation 7.4:

$$\bar{h}_t = \bar{h}_{BEND} + \bar{h}_{Sf} \qquad \textbf{Equation 7.4}$$

where:

$\bar{h}_{BEND}$ = cross-sectional average minor loss due to meander bend (ft);

$\bar{h}_{Sf}$ = cross-sectional average, average friction loss (ft); and

$\bar{h}_t$ = cross-sectional average total energy loss (ft).

Average total energy loss through a meander bend is calculated with Equation 7.5:

$$\bar{h}_T = \left(XS_{TOTAL} - 1\right)\bar{h}_t \qquad \textbf{Equation 7.5}$$

where:

$\bar{h}_t$ = cross-sectional average total energy loss (ft);

$\bar{h}_T$ = average total energy loss through meander bend (ft); and

XS_{TOTAL} = number of cross sections used in analysis.

Results for average total energy loss through a meander bend using the π_5 method were compared to average total energy loss through meander bend estimates using unmodified HEC-RAS output and physical model measurements. These results are shown for discharges of 8 cfs, 12 cfs, and 16 cfs in Table 7.4, Table 7.5, and Table 7.6, respectively. As Table 7.4 through Table 7.6 illustrate, the average total energy loss through a meander bend calculated with the π_5 method is more accurate than the average total energy loss through meander bend results estimated with unmodified HEC-RAS output in both the Type I and Type III bends.

Table 7.4. $\bar{h}_T$ Results at 8 cfs

Bend	$\bar{h}_T$ (ft)		
	Physical Model Measurements	Unmodified HEC-RAS Output	π_5 Method
Type I (U/S) Bend	0.0216	0.0104	0.0211
Type III (D/S) Bend	0.0386	0.0364	0.0395
Absolute Difference From Physical Model $\bar{h}_T$			
Type I (U/S) Bend		0.0112	0.0005
Type III (D/S) Bend		0.0022	0.0010

Table 7.5. $\bar{h}_T$ Results at 12 cfs

Bend	$\bar{h}_T$ (ft)		
	Physical Model Measurements	Unmodified HEC-RAS Output	π_5 Method
Type I (U/S) Bend	0.0162	0.0085	0.0180
Type III (D/S) Bend	0.0291	0.0272	0.0307
Absolute Difference From Physical Model $\bar{h}_T$			
Type I (U/S) Bend		0.0078	0.0018
Type III (D/S) Bend		0.0019	0.0017

Table 7.6. $\bar{h}_T$ Results at 16 cfs

Bend	$\bar{h}_T$ (ft)		
	Physical Model Measurements	Unmodified HEC-RAS Output	π_5 Method
Type I (U/S) Bend	0.0200	0.0092	0.0202
Type III (D/S) Bend	0.0359	0.0315	0.0369
Absolute Difference From Physical Model $\bar{h}_T$			
Type I (U/S) Bend		0.0108	0.0002
Type III (D/S) Bend		0.0044	0.0010

In the Type I bend at a discharge of 8 cfs, physical model measurements suggest that the average total energy loss through a meander bend in the Type I bend is 0.0216 ft. The π_5 method calculates an average total energy loss of 0.0211 ft, which is 2% different from the physical model measurements. At the same discharge in the Type I bend, the

average total energy loss through a meander bend is equal to 0.0104 ft for the unmodified HEC-RAS output, which is a difference of 52% from the physical model data set. This pattern is followed at discharges of 12 cfs and 16 cfs.

In the Type III bend, the π_5 method continues to estimate average total energy loss through a meander bend more accurately than the unmodified HEC-RAS data set. In the Type III bend at a discharge of 16 cfs, physical model measurements suggest that the average total energy loss through a meander bend in the Type III bend is 0.0359 ft. The π_5 method calculates an average total energy loss of 0.0369 ft, which is 3% different from the physical model measurements. At the same discharge in the Type III bend, the average total energy loss through a meander bend is 0.0315 ft for the unmodified HEC-RAS output, which is a difference of 12%. This pattern is followed at discharges of 8 cfs and 12 cfs.

A possible reason that HEC-RAS estimates average total energy loss through a meander bend more accurately in the Type III bend than in the Type I bend is due to the tightness of radius of curvature. The radius of curvature in the Type I bend is 38.75 ft and the radius of curvature in the Type III bend is 65.83 ft and, therefore, the Type III bend is approximately half as tight as the Type I bend. The wider radius of curvature in the Type III bend reduces the effect of spiral currents and secondary currents through the meander bend. By reducing the effect of spiral currents and secondary currents through the meander bend, the average minor loss due to meander bends through a bend is reduced, allowing HEC-RAS to estimate a more accurate average total energy loss through a meander bend.

7.3 EXAMPLE PROBLEM

The procedure presented herein may be applied to actual field projects for the purpose of calculating minor loss due to meander bends and, therefore, total energy loss through a meander bend and along a study reach. A design example is outlined in order to demonstrate how to calculate minor loss due to a meander bend using HEC-RAS output, total energy loss through a meander bend using HEC-RAS output and how to incorporate minor loss due to a meander bend in a HEC-RAS model.

7.3.1 $\bar{h}_{BEND}$ Calculation With HEC-RAS Output

Cross-sectional average minor loss due to a meander bend is calculated with the π_5 method outlined in Section 7.1.3. Using an example problem, descriptions of each step are shown below:

Step 1. Define project area

This example is an imaginary study reach along the Middle Rio Grande in New Mexico. As a result of dam placement, the study reach experienced a shift in channel morphology from a straight braided river to a meandering river. The study reach is a meandering river, 2.5 miles in length and there are ten meander bends along the study reach. The meander bends have altered geomorphic characteristics in the study reach. Geomorphic changes included bank erosion and bend migration.

Step 2. Collect appropriate data during site assessment

During the site assessment, data needed to be collected in order to build the most representative HEC-RAS model. Field data included a field survey, roughness

coefficients at all defined cross sections, and the location of significant expansions/contractions.

A field survey of the study reach included a cross-sectional survey of all relevant cross sections and a thalweg survey. Along the study reach, ninety-nine cross-sectional surveys were collected to define ten meander bends. The thalweg survey defined the bed slope through the study reach and downstream of the study reach. Bed slope through the study reach and downstream of the study reach was estimated as 0.000863 ft/ft. The downstream bed slope was used as the boundary condition in HEC-RAS.

Along with field surveying, roughness coefficients were observed for the ninety-nine defined cross sections. Roughness coefficients were identified for the left overbank, channel, and right overbank of each cross section. For the imaginary study reach, observed roughness coefficients for the left overbank and right overbank were uniformly 0.050 and the channel was uniformly 0.045.

Additional notes were needed to identify the location of significant contraction and expansion reaches. Contraction and expansion reaches, as illustrated in Figure 2.2, are defined facing downstream. During the site assessment, abrupt contraction reaches were observed along the study reach. Each abrupt contraction connected adjacent meander bends and, therefore, nine contraction reaches were noted. Abrupt contractions are indicated with a contraction coefficient of 0.6. Refer to Table 2.1 for a list of contraction and expansion coefficients.

Step 3. Build HEC-RAS model

Using field data collected in Step 2 in addition to other sources of data such as USGS stage vs. discharge records, build a HEC-RAS model representing the 2.5-mile

study reach. The HEC-RAS model includes one plan with a representative geometry data file and steady flow file of the study reach.

Cross-sectional survey data, roughness coefficients, and contraction coefficients are entered in the geometry data file. Use a planform view of the cross-sectional survey to calculate the distance between cross sections. Distances between cross sections are entered in the geometry data file. Figure 7.2 illustrates the HEC-RAS interface used to enter geometry data.

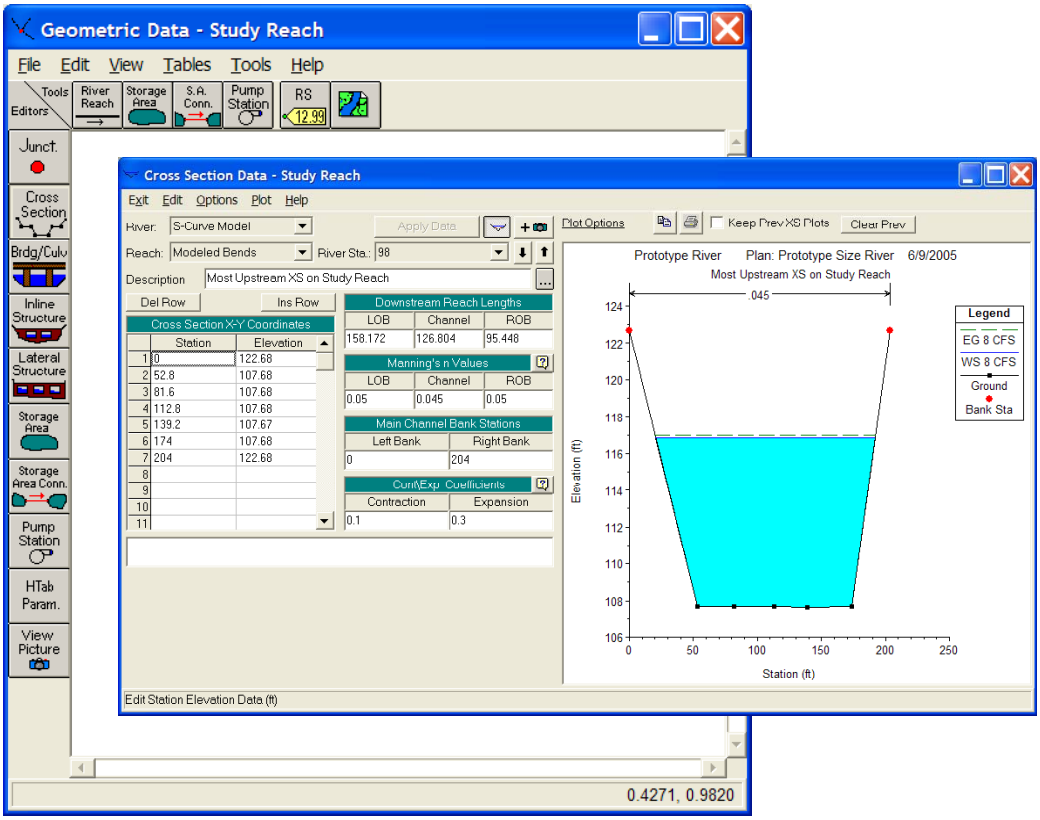

Figure 7.2. HEC-RAS Cross-section Interface

In addition to geometry information, flow data must be entered in a steady flow file in order to run the model. Steady flow data include flow rates of interest and a boundary condition. The flow rate of interest represents a flow condition present in the

study reach. For the study reach, 4,000 cfs was selected as the flow rate of interest and is defined at the most upstream cross section in HEC-RAS. Figure 7.3 presents the interface used to enter the flow rate in the HEC-RAS model. Assuming there are no tributaries, the flow rate remains constant along the 2.5-mile study reach.

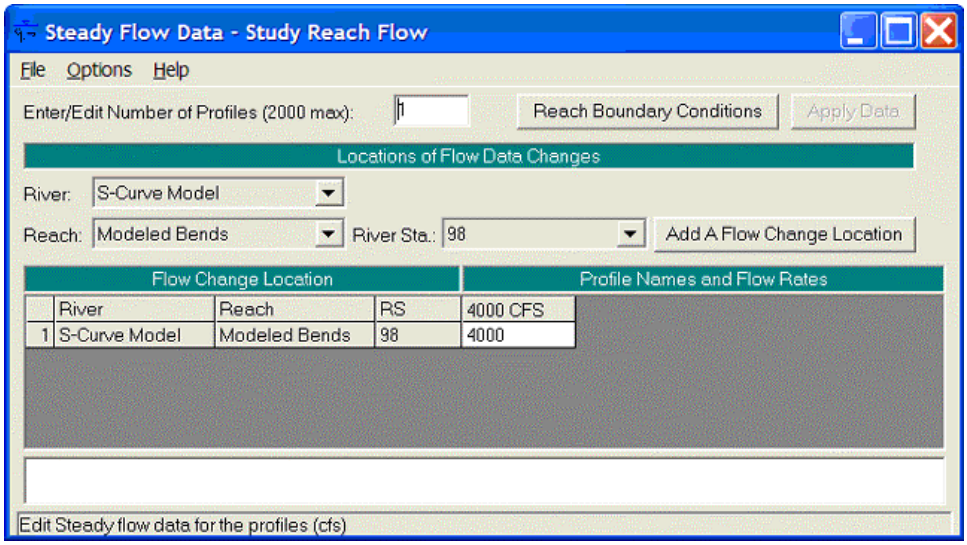

Figure 7.3. HEC-RAS Steady Flow Interface

Once the flow rate is entered in the steady flow file, a boundary condition must be specified. A downstream boundary condition is required since the flow is assumed subcritical. Using the defined HEC-RAS options, the downstream boundary condition is selected as "Normal Depth" and, therefore, the downstream bed slope is entered in HEC-RAS. Figure 7.4 shows the HEC-RAS interface used for entering the boundary condition.

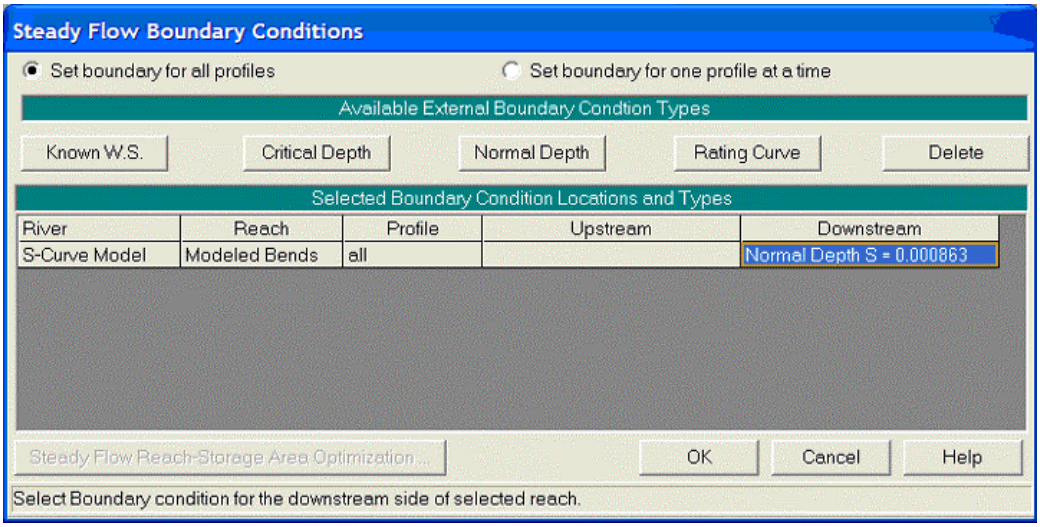

Figure 7.4. HEC-RAS Boundary Condition Interface

Step 4. Run HEC-RAS

Using the plan created in Step 3, run the HEC-RAS model. Create an output table in HEC-RAS including top width and friction loss. An example of the output table interface is shown in Figure 7.5.

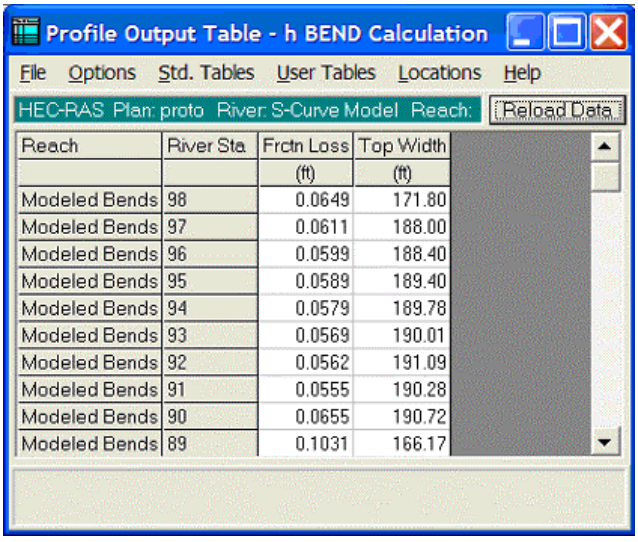

Reach	River Sta	Frctn Loss (ft)	Top Width (ft)
Modeled Bends	98	0.0649	171.80
Modeled Bends	97	0.0611	188.00
Modeled Bends	96	0.0599	188.40
Modeled Bends	95	0.0589	189.40
Modeled Bends	94	0.0579	189.78
Modeled Bends	93	0.0569	190.01
Modeled Bends	92	0.0562	191.09
Modeled Bends	91	0.0555	190.28
Modeled Bends	90	0.0655	190.72
Modeled Bends	89	0.1031	166.17

Figure 7.5. HEC-RAS Output Table Interface

Step 5. Calculate $\overline{TW}$

In order to calculate average top width, copy the top width column in the HEC-RAS output file into a Microsoft® Excel table. Use these data to estimate average top width in each meander bend. Average top width results are shown in Table 7.7.

Table 7.7. $\overline{TW}$ Results

Bend	$\overline{TW}$ (ft)
1 (U/S)	189.45
2	138.42
3	189.57
4	138.62
5	191.27
6	139.44
7	188.51
8	137.32
9	191.50
10 (D/S)	135.99

Step 6. Estimate r_c

Radius of curvature is estimated for each meander bend using aerial photographs of the study reach. For the imaginary study reach, radius of curvature estimates for each meander bend are shown in Table 7.8.

Table 7.8. r_c Measurements

Bend	r_c (ft)
1 (U/S)	465
2	790
3	465
4	790
5	465
6	790
7	465
8	790
9	465
10 (D/S)	790

Step 7. Calculate π_5

π_5 is defined in Equation 7.1. Calculate π_5 using average top width calculated in Step 5 and radius of curvature estimated in Step 6. Table 7.9 presents π_5 results.

Table 7.9. π_5 Results

Bend	$\overline{TW}$ (ft)	r_c (ft)	π_5
1 (U/S)	189.45	465	2.45
2	138.42	790	5.71
3	189.57	465	2.45
4	138.62	790	5.70
5	191.27	465	2.43
6	139.44	790	5.67
7	188.51	465	2.47
8	137.32	790	5.75
9	191.50	465	2.43
10 (D/S)	135.99	790	5.81

Step 8. Calculate $\bar{h}_{BEND}/\bar{h}_{Sf}$

Calculate $\bar{h}_{BEND}/\bar{h}_{Sf}$ using Equation 7.2, which illustrated the relationship between π_5 and $\bar{h}_{BEND}/\bar{h}_{Sf}$. π_5 was calculated in Step 7. $\bar{h}_{BEND}/\bar{h}_{Sf}$ results are presented in Table 7.10.

Table 7.10. $\bar{h}_{BEND}/\bar{h}_{Sf}$ Results

Bend	π_5	$\bar{h}_{BEND}/\bar{h}_{Sf}$
1 (U/S)	2.45	1.31
2	5.71	0.30
3	2.45	1.31
4	5.70	0.30
5	2.43	1.32
6	5.67	0.30
7	2.47	1.30
8	5.75	0.29
9	2.43	1.33
10 (D/S)	5.81	0.29

Step 9. Calculate $\bar{h}_{BEND}$

Calculate cross-sectional average minor loss due to a meander bend using Equation 7.3. In order to complete this calculation, copy the average friction loss (h_{Sf}) column in the HEC-RAS output table into a Microsoft® Excel table. Use these values to calculate cross-sectional average, average friction loss in each meander bend. Cross-sectional average, average friction loss is calculated by averaging the average friction loss estimates for an individual meander bend. Once cross-sectional average, average friction loss is calculated for each meander bend, calculate cross-sectional average minor loss due to a meander bend using Equation 7.3. Cross-sectional average minor loss due to meander bend results are shown in Table 7.11. Cross-sectional average minor loss due

to meander bend results are used to estimate the average total energy loss through a meander bend in Section 7.3.2.

Table 7.11. $\bar{h}_{BEND}$ Results

Bend	$\bar{h}_{BEND}$ (ft)
1 (U/S)	0.077
2	0.045
3	0.076
4	0.045
5	0.075
6	0.044
7	0.073
8	0.042
9	0.071
10 (D/S)	0.039

7.3.2 $\bar{h}_T$ Calculation With HEC-RAS Output

Previous analysis in Step 9 of the π_5 method provides all necessary data to compute average total energy loss through a meander bend. Average total energy loss through a meander bend is calculated with Equation 7.4 and Equation 7.5. Average total energy loss through a meander bend results are presented in Table 7.12.

Table 7.12. $\bar{h}_T$ Results

Bend	$\bar{h}_T$ (ft)
1 (U/S)	0.676
2	1.170
3	0.671
4	1.158
5	0.661
6	1.127
7	0.641
8	1.109
9	0.618
10 (D/S)	1.062
Σ	**8.894**

7.3.3 Comparison Between $\bar{h}_T$ Calculated With Modified HEC-RAS Data Set and Unmodified HEC-RAS Data Set

Analysis was completed in order to compare the average total energy loss through a meander bend using modified HEC-RAS data and unmodified HEC-RAS data. The modified HEC-RAS data set applies the π_5 method to HEC-RAS output. The unmodified HEC-RAS data set strictly uses HEC-RAS output tables to calculate total energy loss through a meander bend.

The modified HEC-RAS data set was used in Section 7.3.2 in order to estimate the average total energy loss through each meander bend and along the 2.5-mile study reach. From Table 7.12, the estimate of average total energy loss along the 2.5-mile study reach was 8.9 ft.

The unmodified HEC-RAS data set used HEC-RAS output from the same model to calculate the average total energy loss through a meander bend. Average total energy loss through a meander bend and along the 2.5-mile study reach was calculated using HEC-RAS output for friction loss. Friction loss is assumed to be equal to total energy

loss since the primary source of energy loss through a meander bend in a 1-D HEC-RAS model is friction. Table 7.13 presents the average total energy loss results through each meander bend and along the 2.5-mile study reach. The average total energy loss along the 2.5-mile study reach was 5.8 ft.

Using the two data sets, it is important to understand if the average total energy loss through a meander bend estimated with unmodified HEC-RAS output is more or less conservative than the average total energy loss estimated with modified HEC-RAS output. If the unmodified HEC-RAS data set underestimates the average total energy loss, errors can potentially occur in design projects, for instance, in bendway-weir design. The modified HEC-RAS data set calculated the average total energy loss along the 2.5-mile study reach as 8.9 ft. The unmodified HEC-RAS data set calculated the average total energy loss to be 5.8 ft along the 2.5-mile study reach, which is 35% less than the modified HEC-RAS data set. Such an alarming difference between the two estimates of average total energy loss suggests how significant minor loss due to a meander bend is in determining total energy loss. Since minor loss due to a meander bend is significant, further analysis needs to be completed to incorporate minor loss due to a meander bend in HEC-RAS iterations.

Table 7.13. $\bar{h}_T$ Results for Unmodified HEC-RAS Output

Bend	$\bar{h}_T$ (ft)
1 (U/S)	0.292
2	0.901
3	0.290
4	0.890
5	0.284
6	0.864
7	0.278
8	0.858
9	0.266
10 (D/S)	0.826
Σ	**5.750**

7.3.4 n_{EFF} Calculation

In order to incorporate minor loss due to a meander bend into HEC-RAS, a selected term was modified in the model. The term used to incorporate minor loss due to a meander bend was the roughness coefficient (n). The modified roughness coefficient was termed effective roughness coefficient (n_{EFF}). In order to calculate the effective roughness coefficient for each meander bend, the following steps were executed:

Step 1. Create a table in Microsoft® Excel

A table needed to be created in Microsoft® Excel in order to organize necessary data for the effective roughness coefficient calculation. Table 7.14 shows an example of the Microsoft® Excel table for Bend 2. Cross-sectional average total energy loss was calculated with Equation 7.4 in Section 7.3.2 and is used in Column 1 of the table. Energy grade line (EGL_{CALC}) is calculated with the following equation:

$$EGL_{CALC} = \frac{\bar{h}_t}{\Delta x} \qquad \textbf{Equation 7.6}$$

where:

Δx = distance along the centerline of the channel between cross sections (ft);

EGL_{CALC} = energy grade line (ft/ft); and

$\bar{h}_t$ = cross-sectional average total energy loss (ft).

Discharge (Q), cross-sectional area (A), hydraulic radius (R), and the roughness coefficient (n) are copied from the HEC-RAS output table into a Microsoft® Excel table. Meander bend averages for each term are calculated in the final row of the table. Friction slope ($S_{f\ MANNING}$) is calculated using a version of Manning's equation and is calculated for the final row in the table. The version of Manning's equation used in this analysis is illustrated in Equation 2.9.

Table 7.14. Table Required for n_{EFF} Calculation

Bend	XS	$\bar{h}_t$ (ft)	EGL_{CALC} (ft/ft)	Q (cfs)	A (ft^2)	R (ft)	n	$S_{f\ MANNING}$ (ft/ft)
2	87	0.195	0.00155	4000	991.82	6.98	0.0450	
	86	0.195	0.00155	4000	982.32	6.97	0.0450	
	85	0.195	0.00155	4000	971.91	6.90	0.0450	
	84	0.195	0.00155	4000	974.60	6.91	0.0450	
	83	0.195	0.00155	4000	968.06	6.88	0.0450	
	82	0.195	0.00155	4000	955.08	6.82	0.0450	
	81	0.195	0.00155	4000	959.11	6.81	0.0450	
		0.195	**0.00155**	**4000**	**971.84**	**6.90**	**0.0450**	**0.00118**

Step 2. Calculate n_{EFF}

Use a Solver routine to change the calculated meander bend average roughness coefficient until the energy grade line is equal to friction slope. The solution found from the Solver routine is the effective roughness coefficient. Table 7.15 illustrates the cells required for the Solver routine. The yellow-shaded cell is effective roughness coefficient

and is set as the "cell to change" in the Solver routine. The light green-shaded cell is selected as the "target cell" in the Solver routine. One constraint is set in the Solver routine for $EGL_{CALC} = S_{f\,MANNING}$.

Table 7.15. Selected Cells for Solver Routine

Bend	XS	$\bar{h}_T$ (ft)	EGL_{CALC} (ft/ft)	Q (cfs)	A (ft^2)	R (ft)	n	$S_{f\,MANNING}$ (ft/ft)
2	87	0.195	0.00155	4000	991.82	6.98	0.0450	
	86	0.195	0.00155	4000	982.32	6.97	0.0450	
	85	0.195	0.00155	4000	971.91	6.90	0.0450	
	84	0.195	0.00155	4000	974.60	6.91	0.0450	
	83	0.195	0.00155	4000	968.06	6.88	0.0450	
	82	0.195	0.00155	4000	955.08	6.82	0.0450	
	81	0.195	0.00155	4000	959.11	6.81	0.0450	
		0.195	**0.00155**	**4000**	**971.84**	**6.90**	**0.0515**	**0.00155**

Step 3. Check n_{EFF}

In HEC-RAS, the average conveyance method for friction slope is used in place of Manning's equation for friction slope used in Step 2 to calculate average friction slope ($\bar{S}_{f-CONV}$). Average friction slope calculated with the average conveyance method is shown in Equation 2.10. The analysis goal is to modify the roughness coefficient in order to match the average friction slope calculated through HEC-RAS to the energy grade line using the π_5 method. Since this is the analysis goal, the effective roughness coefficients calculated in Step 2 needed to be substituted into the equation for average friction slope in order to determine if the effective roughness coefficient predicts the same slope. If $EGL_{CALC} = \bar{S}_{f-CONV}$, then the effective roughness coefficient calculated during Step 2 is the final value for the meander bend. If $EGL_{CALC} \neq \bar{S}_{f-CONV}$, then proceed to Step 4.

In order to complete this portion of the analysis, a table is set up as the example in Table 7.16. Energy grade line, flow rate, flow area, and hydraulic radius are equal to values used in Table 7.15. Effective roughness coefficient is the same at each cross section in an individual meander bend and is the value computed during the Solver routine in Step 2. Average friction slope is calculated at each cross section using Equation 2.10. In the last row of the table, average the values for energy grade line and average friction slope. The average values for energy grade line and average friction slope are used in the comparison.

Table 7.16. Comparison of EGL_{CALC} and $\overline{S}_{f\text{-}CONV}$

Bend	XS	EGL_{CALC} (ft/ft)	Q (cfs)	A (ft^2)	R (ft)	n_{EFF}	$\overline{S}_{f-CONV}$ (ft/ft)
2	87	0.00155	4000	991.82	6.98	0.05151	0.00148
	86	0.00155	4000	982.32	6.97	0.05151	0.00152
	85	0.00155	4000	971.91	6.9	0.05151	0.00154
	84	0.00155	4000	974.60	6.91	0.05151	0.00155
	83	0.00155	4000	968.06	6.88	0.05151	0.00160
	82	0.00155	4000	955.08	6.82	0.05151	0.00162
	81	0.00155	4000	959.11	6.81	0.05151	
		0.00155					**0.00157**

Step 4. Modify n_{EFF}

If it was determined in Step 3 that $EGL_{CALC} \neq \overline{S}_{f-CONV}$, then Step 4 is used to modify the effective roughness coefficient. By modifying the effective roughness coefficient, the goal of $EGL_{CALC} = \overline{S}_{f-CONV}$ is achieved. Table 7.17 presents the table required to proceed with Step 4. Initially, Table 7.17 is a copy of Table 7.16 but as Table 7.17 demonstrates, the effective roughness coefficient is modified at all cross sections

until $EGL_{CALC} = \overline{S}_{f-CONV}$. When average $EGL_{CALC} = \overline{S}_{f-CONV}$, record effective roughness coefficient.

Table 7.17. Modified n_{EFF} for $EGL_{CALC} = \overline{S}_{f\text{-}CONV}$

Bend	XS	EGL_{CALC} (ft/ft)	Q (cfs)	A (ft^2)	R (ft)	n_{EFF}	$\overline{S}_{f-CONV}$ (ft/ft)
2	87	0.00155	4000	991.82	6.98	0.05145	0.00148
	86	0.00155	4000	982.32	6.97	0.05145	0.00152
	85	0.00155	4000	971.91	6.9	0.05145	0.00154
	84	0.00155	4000	974.60	6.91	0.05145	0.00155
	83	0.00155	4000	968.06	6.88	0.05145	0.00159
	82	0.00155	4000	955.08	6.82	0.05145	0.00162
	81	0.00155	4000	959.11	6.81	0.05145	
		0.00155					**0.00155**

Step 5. Organize final list of n_{EFF}

In order to continue with the analysis, a final list of all effective roughness coefficients is required. The final list for the imaginary study reach is shown in Table 7.18.

Table 7.18. n_{EFF} for Each Meander Bend

Bend	n_{EFF}
1 (U/S)	0.06820
2	0.05145
3	0.06810
4	0.05145
5	0.06836
6	0.05150
7	0.06795
8	0.05110
9	0.06840
10 (D/S)	0.05016

7.3.5 Implementation of n_{EFF} in HEC-RAS

Once the effective roughness coefficient is calculated for each meander bend, the value must be used in the HEC-RAS analysis. Effective roughness coefficient replaces the observed roughness coefficient at all cross sections in a meander bend. For instance, Bend 1 is represented by river stations 92 to 97 and, therefore, the effective roughness coefficient of 0.0682 replaces the observed roughness coefficient of 0.045 at river stations 92 to 97. This process is completed for the entire study reach.

7.3.6 n_{EFF} Significance

Significance of the effective roughness coefficient is observed along the study reach once HEC-RAS iteratively calculated the water-surface profile and energy grade line using the effective roughness coefficient. Table 7.19 presents the results from implementing an effective roughness coefficient in HEC-RAS. Table 7.19 shows that the effective roughness coefficient increases the average total energy loss through the study reach to 6.9 ft, which is an increase of 1.1 ft. The purpose of implementing the effective roughness coefficient in HEC-RAS was to increase friction loss from 5.8 ft to 8.9 ft, which is a difference of 3.1 ft. The HEC-RAS output of friction loss was 65% less than the desired output for friction loss using the π_5 method.

In order to understand why HEC-RAS output of average total energy loss through the study reach was 65% less than the desired output for average total energy loss through the study reach using the π_5 method, further analysis was completed. Patterns were observed between meander bends to note changes in flow depth, flow area, conveyance, and friction loss for the HEC-RAS output considering the effective

roughness coefficient and the π_5 method. From this analysis, it was observed that the π_5 method calculated average total energy loss for each meander bend independent of the other bends while HEC-RAS calculated average total energy loss given a series of meander bends. When average total energy loss was calculated for an individual bend, the average total energy loss estimate was greater than the average total energy loss calculated for a series of meander bends. Hydraulic calculations of meander bends in a series, such as in HEC-RAS, influence the calculation of the upstream bend. For instance, flow depth from the downstream bend influences the flow depth in the upstream bend through backwater calculations. Therefore, the average total energy loss calculated from meander bends in a series does not necessarily increase with the same magnitude as average total energy loss calculated from individual meander bends in the π_5 method. Comparing Table 7.13 and Table 7.19, in some cases, average total energy loss decreases once the effective roughness coefficient is implemented in HEC-RAS. Further analysis needs to be completed in order to fully understand the influence of meander bends in series on average total energy loss calculations along the study reach.

Table 7.19. $\bar{h}_T$ for HEC-RAS Output With n_{EFF}

Bend	$\bar{h}_T$ (ft)
1 (U/S)	0.477
2	0.845
3	0.474
4	0.852
5	0.479
6	0.855
7	0.485
8	0.893
9	0.543
10 (D/S)	0.962
Σ	**6.864**

CHAPTER 8 CONCLUSION AND RECOMMENDATIONS

8.1 OVERVIEW

Research presented herein explored the accuracy of HEC-RAS to calculate flow depths and total energy loss through a meander bend with and without bendway weirs. HEC-RAS is a 1-D hydraulic model that is commonly used during 2-D and 3-D analysis. Since HEC-RAS is often used in 2-D and 3-D analysis, research was needed to determine the accuracy of HEC-RAS during such analysis. In this study, analysis of HEC-RAS was limited to a gradually-varied, steady-flow situation. Exploration of HEC-RAS extended through the base-line analysis and the bendway-weir analysis. Conclusions for the base-line analysis are the following:

1. Modified Test reduced the assumed Manning's *n* of 0.015 for concrete in HEC-RAS to 0.013;
2. At 8 cfs, the Modified Test exhibited 0.25% difference in cross-sectional average flow depth from the physical model in the Type I bend;
3. At 8 cfs, the Modified Test exhibited 0.64% difference in cross-sectional average flow depth from the physical model in the Type III bend; and
4. The Modified Test was the foundation model for trial analysis in the bendway-weir testing program.

Conclusions for the bendway-weir analysis are the following:

1. Trial 16 was selected to be the best possible HEC-RAS model;
2. Trial 16 simultaneously adjusted Manning's *n*, and contraction and expansion coefficients at all necessary cross sections to achieve results;
3. At 8 cfs, Trial 16 results displayed a 3% difference in cross-sectional average flow depth from the physical model in the Type I bend and at 16 cfs, Trial 16 results displayed a 1% difference in cross-sectional average flow depth from the physical model in the Type III bend;
4. Trial 16 results displayed a 60% difference in total energy loss from the physical model in the Type I bend and a difference of 7% in the Type III bend; and
5. Based on total energy results, additional research is needed to note the effect of spiral currents and secondary currents on the total energy loss.

As stated as part of the bendway-weir analysis conclusions, additional research was completed to observe the effect of spiral currents and secondary currents on the total energy loss through a meander bend. Spiral currents and secondary currents are collectively referred to as minor loss due to a meander bend. Using the data from the base-line analysis, research was completed to determine the effect of minor loss due to meander bends. Conclusions of this research are the following:

1. At 16 cfs, average minor loss due to a meander bend was 57% of total energy loss in Type I bend;
2. At 16 cfs, average minor loss due to a meander bend was 24% of total energy loss in Type III bend; and

3. Minor loss due to a meander bend is significant and, therefore, methodology is needed to aid calculating more accurate total energy loss through a meander bend.

Conclusions from methodology development are as follows:

1. Twenty-three dimensionless π terms were developed based on significant external, material, and channel properties;
2. Twenty-three dimensionless π terms were regressed against $\bar{h}_{BEND}/\bar{h}_{Sf}$;
3. π_5, shown in Equation 7.1, was selected as the most significant pi term;
4. Predictor equation shown in Equation 7.2 was used to calculate cross-sectional average minor loss due to a meander bend;
5. Equation 7.3 was used to calculate cross-sectional average minor loss due to a meander bend;
6. Equation 7.5 was used to calculate average total energy loss through a meander bend;
7. Methodology was developed to incorporate the π_5 method into HEC-RAS output, which is stated in Chapter 7, Section 7.1.3; and
8. Example problem was used to incorporate the π_5 method into natural river systems shown in Chapter 7, Section 7.3.

8.2 RECOMMENDATIONS FOR FURTHER RESEARCH

Research completed in this study started the process to accurately calculate total energy loss along meander bends. Further research needs to be completed to determine

the limitations to the π_5 methodology and to extend this methodology to the bendway-weir analysis.

During the study, the bendway-weir analysis had limited options. Limitations such as only adjusting Manning's *n*, and contraction and expansion coefficients prohibited investigation of various trials stated in this analysis. The trial list is shown in Table 5.1. By increasing the scope of the analysis, additional HEC-RAS features can be investigated to conclude if HEC-RAS accurately predicts flow depths and total energy loss through meander bends with bendway weirs. Suggested HEC-RAS features for future analysis are the following:

1. bridge options including skewing options for angled bendway weirs;
2. blocked obstructions;
3. ineffective flow lines (Eom, 2004); and
4. weir options.

Creative exploration is needed to use these options in order to define a bendway weir in HEC-RAS. Exploring and exhausting the additional options can conclusively determine whether HEC-RAS is able to accurately calculate flow depths and total energy loss through meander bends with bendway weirs.

CHAPTER 9 REFERENCES

Benson, T. (2004). Conservation of Energy. NASA Glenn Learning Technologies Home Page, NASA, documented March 2005, http://www.grc.nasa.gov/WWW/K-12/airplane/thermo1f.html.

Bitner, C. J. (2003). Selection and Design of Porous Low Drop Grade Control Structures. M.S. Thesis, Department of Civil Engineering, Colorado State University, Fort Collins, CO.

Brater, E. F. and H. W. King (1976). Handbook of Hydraulics. McGraw-Hill Book Company, New York, NY.

Breck, D. G. (2000). Modeling Water Surface Profiles Over A Bendway Weir Using HEC-RAS 2.2. Montana University System Water Resource Center Report No. 203.

Chow, V. T. (1959). Open-Channel Hydraulics. McGraw-Hill Book Company, New York, NY.

Darrow, J. D. (2004). Effects of Bendway Weir Characteristics on Resulting Flow Conditions. M.S. Thesis, Department of Civil Engineering, Colorado State University, Fort Collins, CO.

Eom, M. (2004). Environmental Dike Design Considerations for the Lower Mississippi River. PhD Dissertation, Department of Civil Engineering, Colorado State University, Fort Collins, CO.

Heintz, M. L. (2002). Investigation of Bendway Weir Spacing. M.S. Thesis, Department of Civil Engineering, Colorado State University, Fort Collins, CO.

Mockmore, C. A. (1944). Flow Around Bends in Stable Channels. *American Society of Civil Engineering Paper No. 2217*, 109:601-621.

Rosgen, D. (1996). Applied River Morphology. Wildland Hydrology, Pagosa Springs, CO.

U.S. Corps of Engineers (2001a). HEC-RAS River Analysis System Hydraulic Reference Manual Version 3.0.

U.S. Corps of Engineers (2001b). HEC-RAS River Analysis System Users Manual Version 3.0.

Yarnell, D. L. and S. M. Woodward (1936). Flow of Water Around 180-Degree Bends. United States Department of Agriculture Technical Bulletin No. 526, October.

APPENDIX A

TOTAL STATION SURVEY

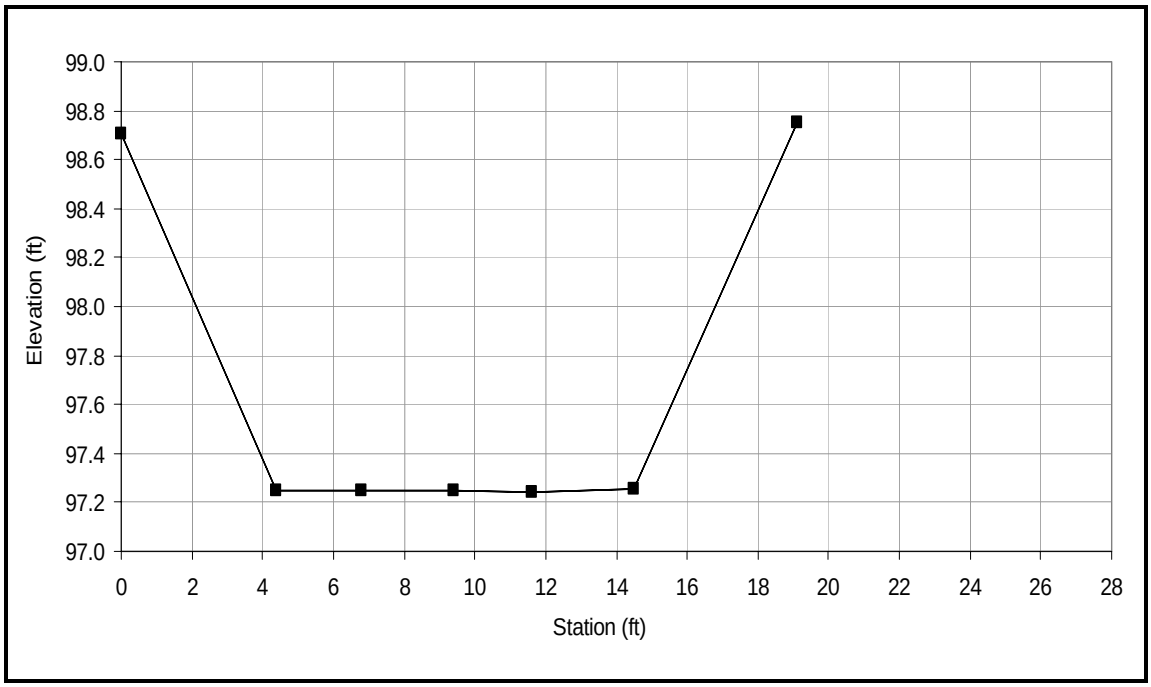

Figure A.1. XS0 Cross-sectional Profile

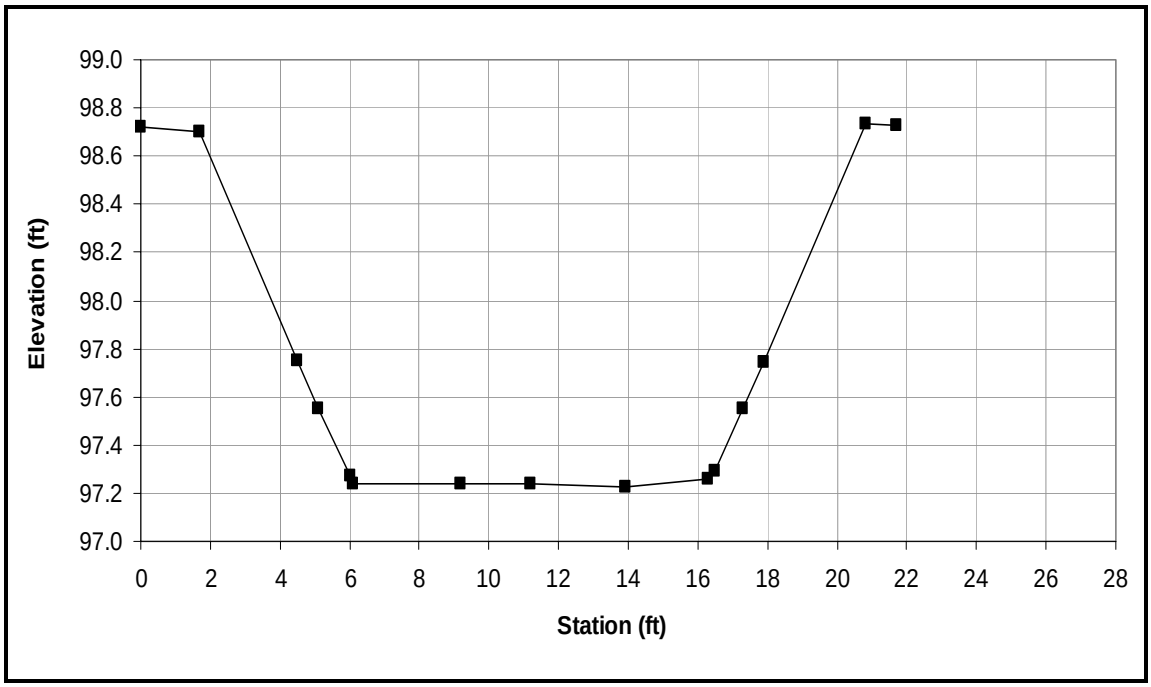

Figure A.2. XS1 Cross-sectional Profile

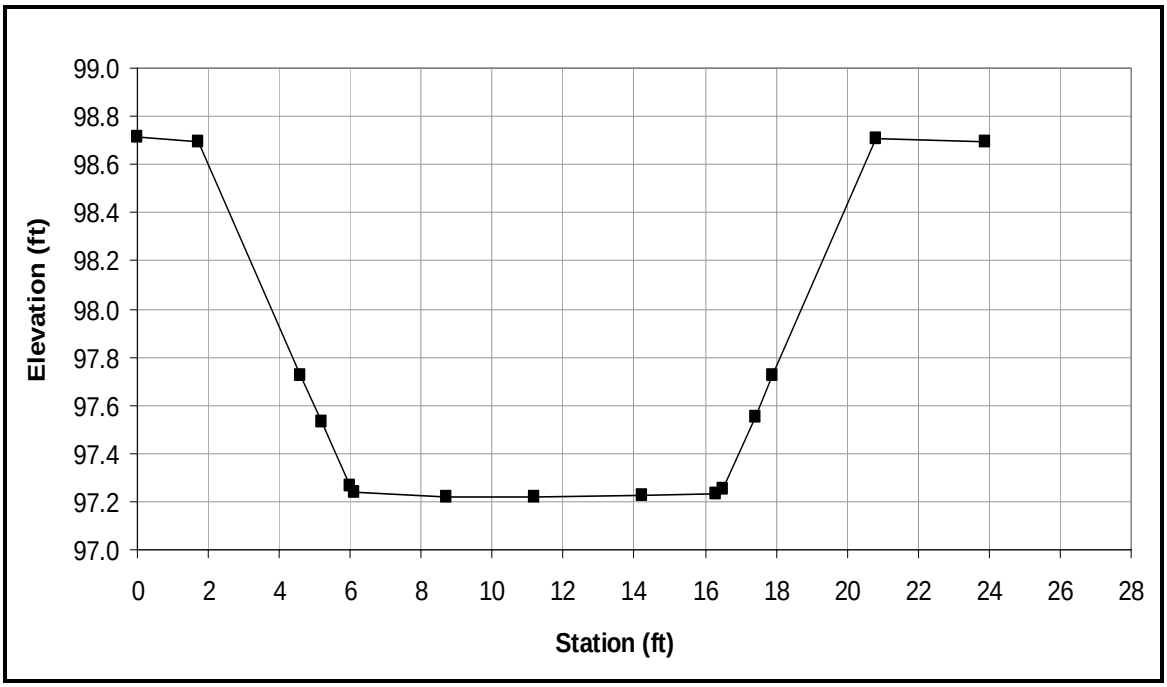

Figure A.3. XS2 Cross-sectional Profile

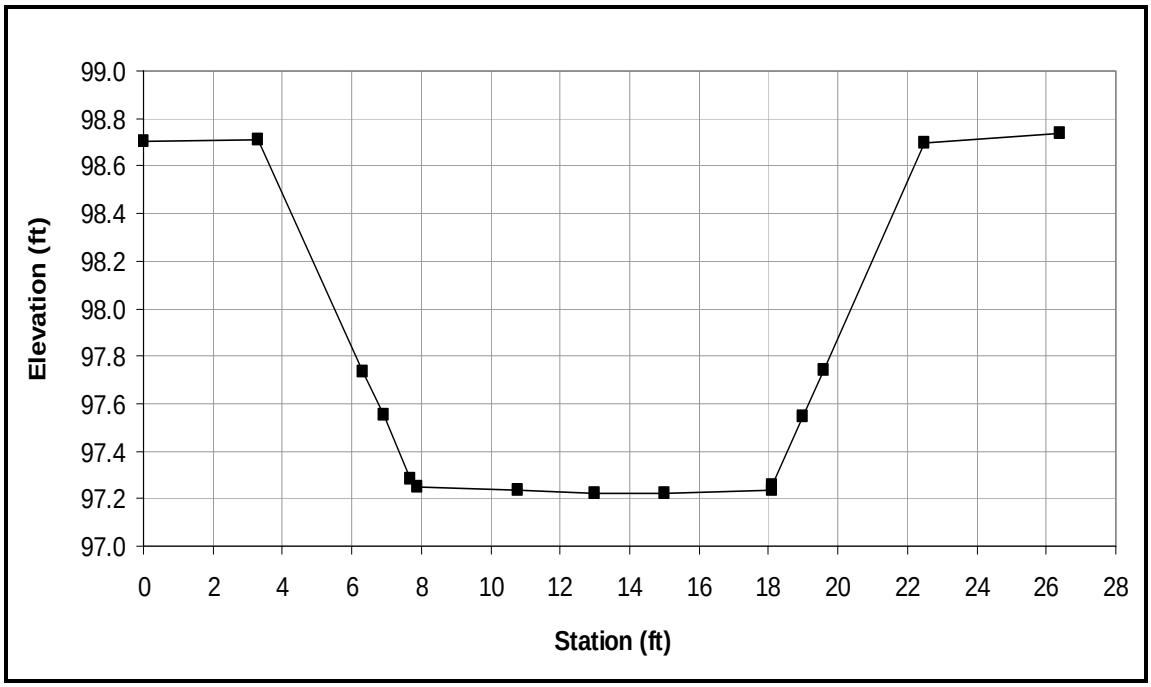

Figure A.4. XS3 Cross-sectional Profile

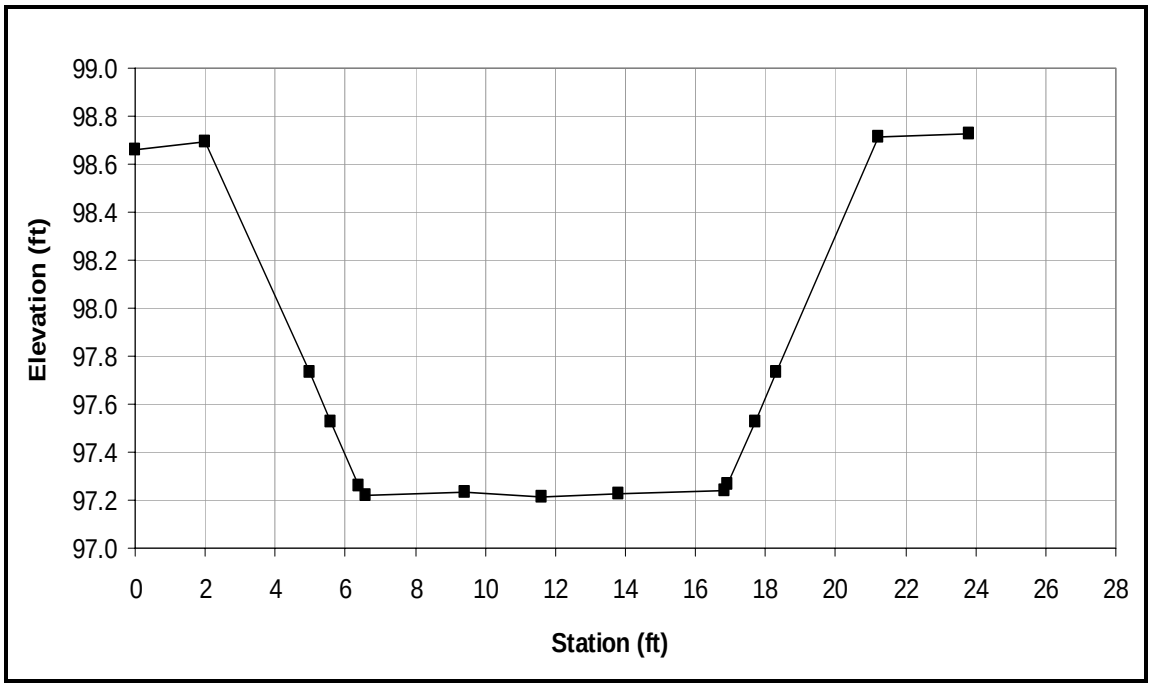

Figure A.5. XS4 Cross-sectional Profile

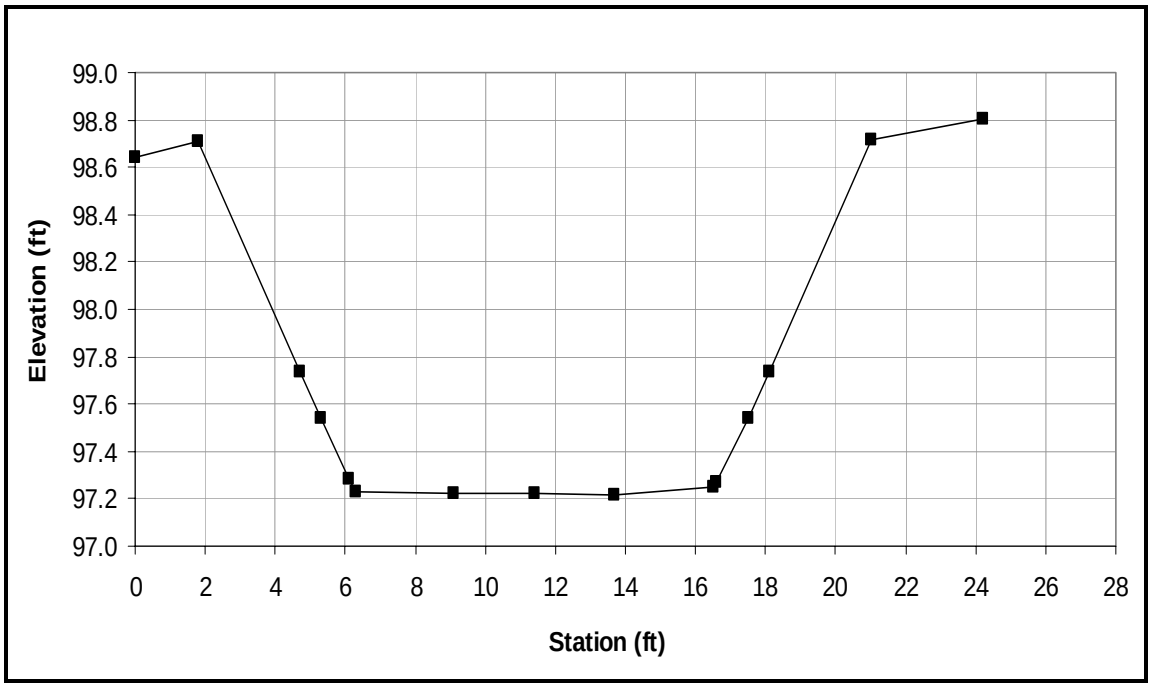

Figure A.6. XS5 Cross-sectional Profile

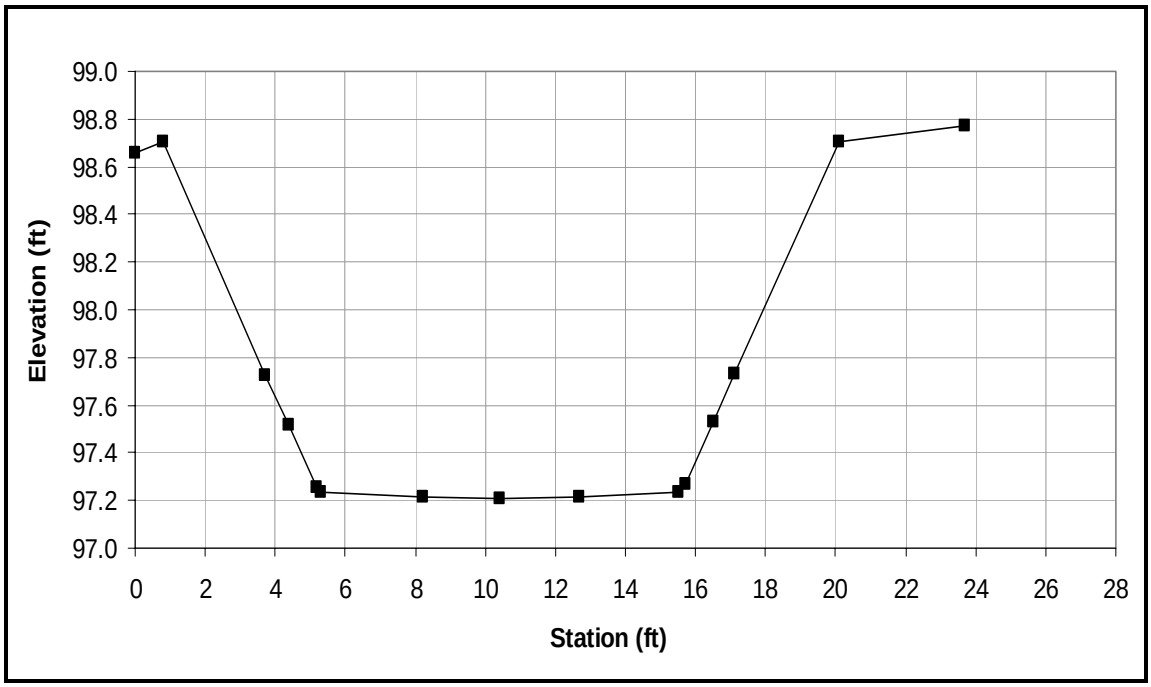

Figure A.7. XS6 Cross-sectional Profile

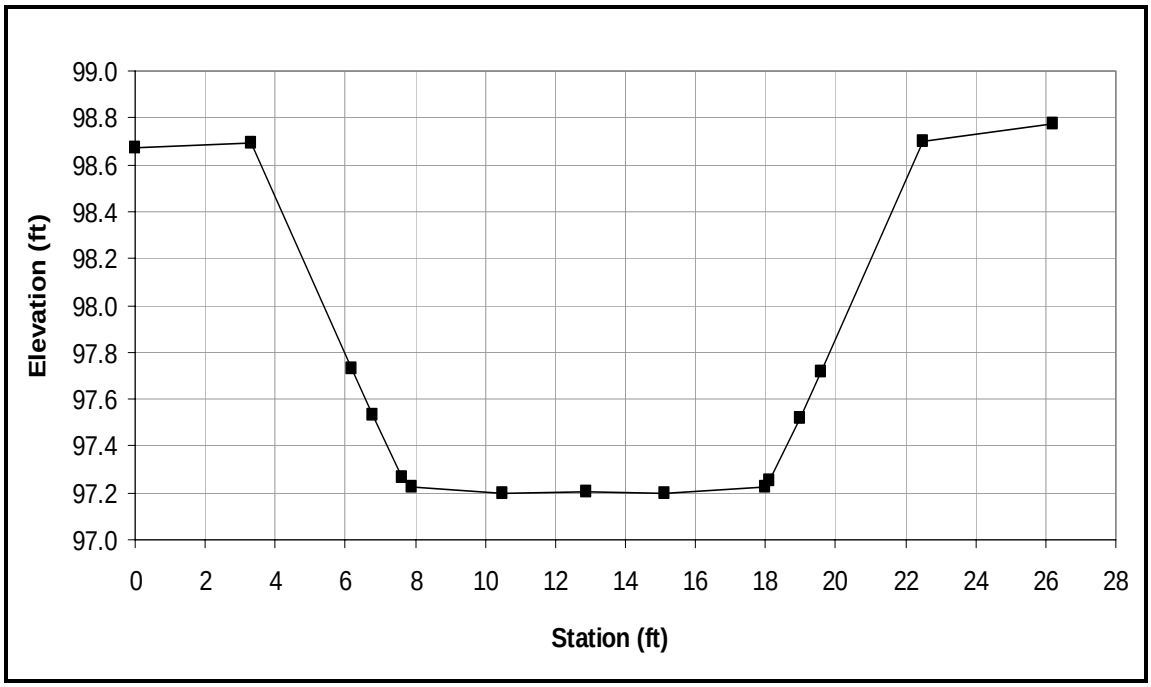

Figure A.8. XS7 Cross-sectional Profile

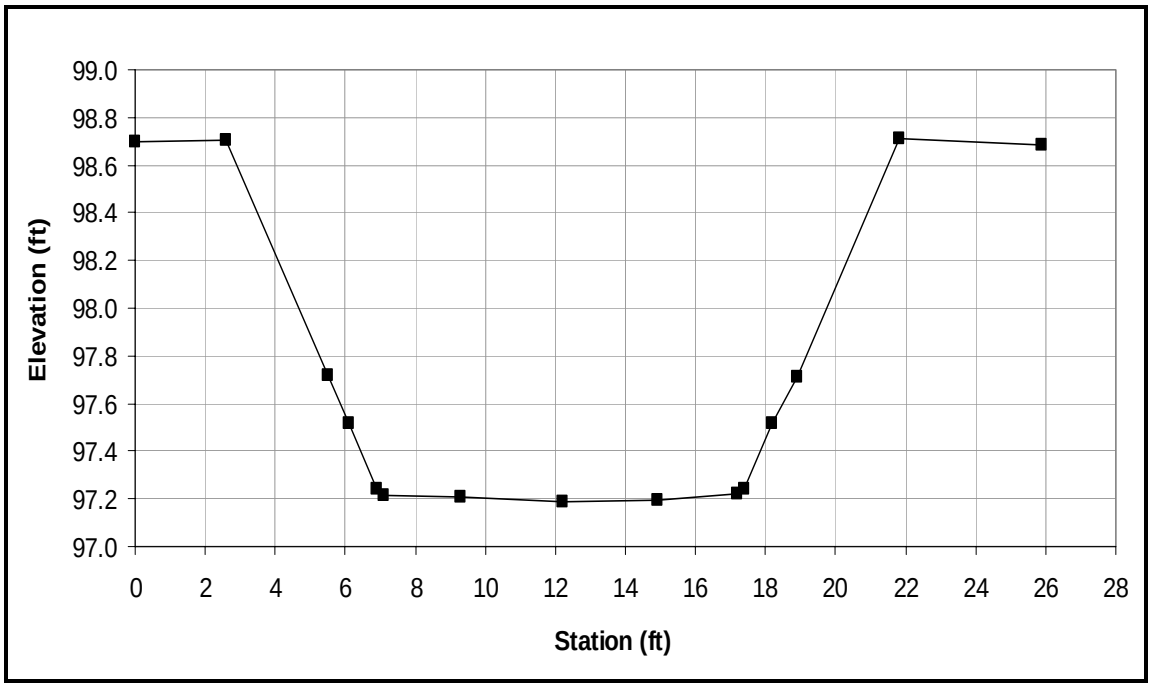

Figure A.9. XS8 Cross-sectional Profile

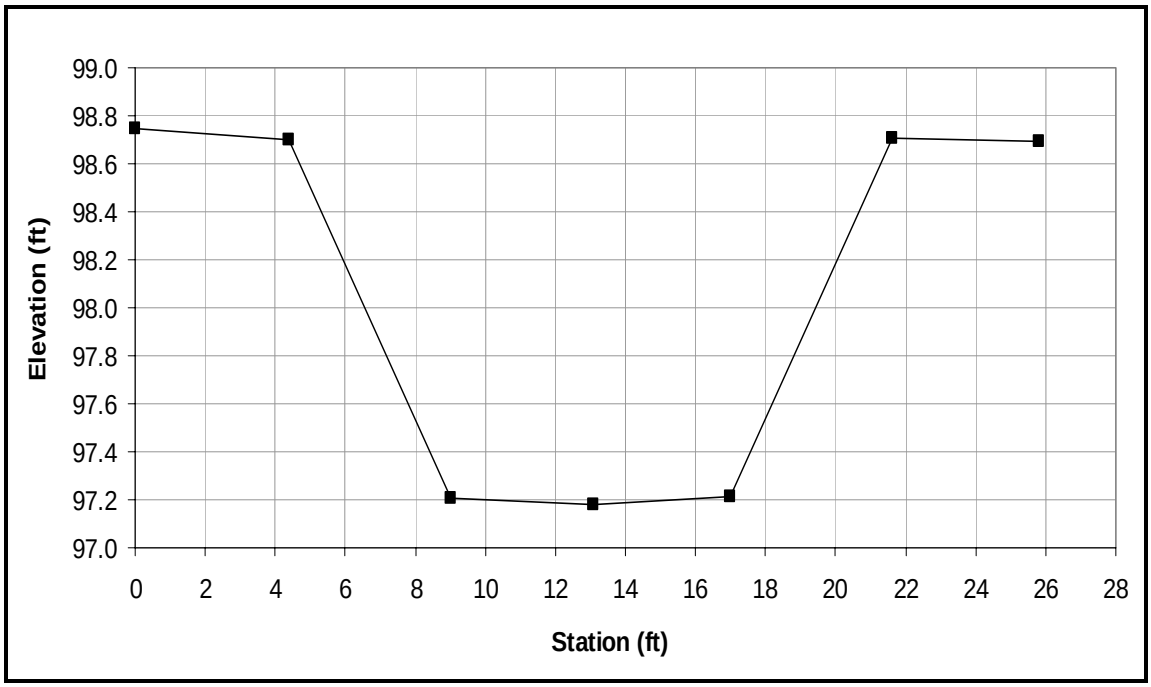

Figure A.10. XS9 Cross-sectional Profile

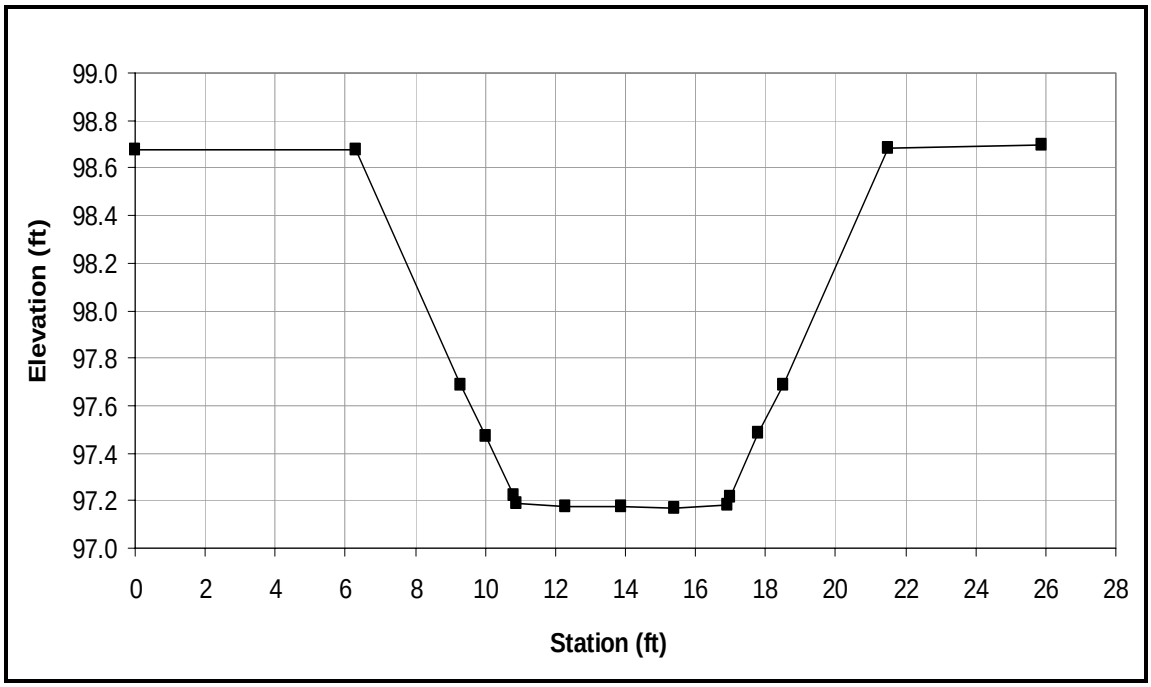

Figure A.11. XS10 Cross-sectional Profile

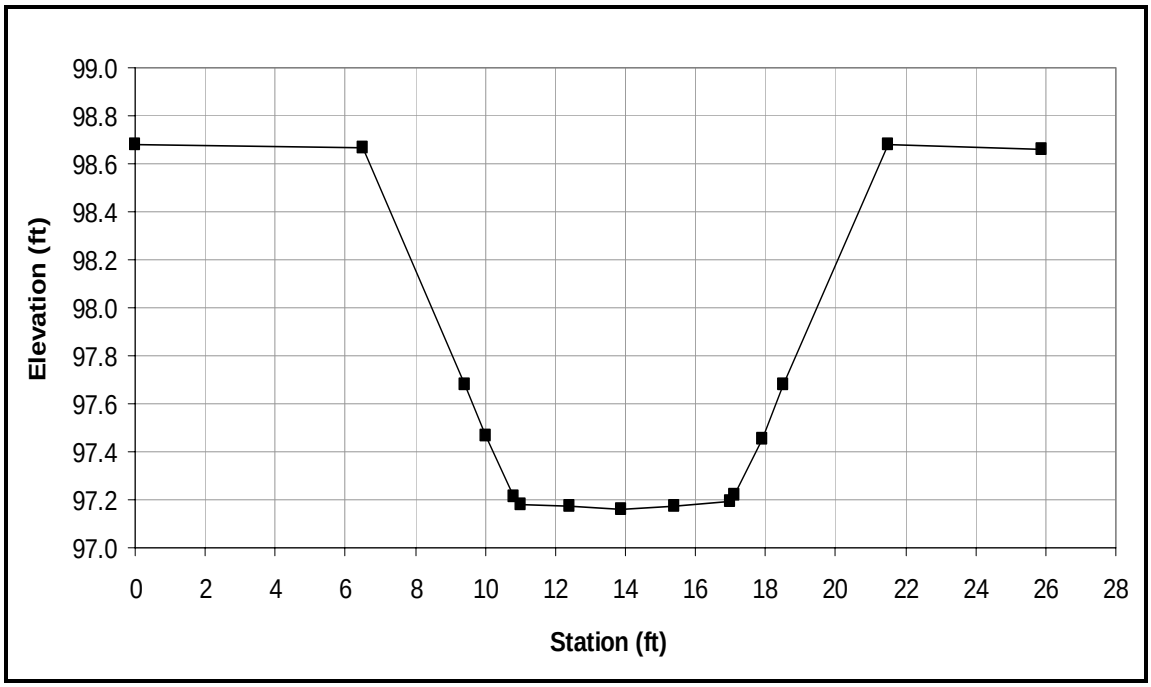

Figure A.12. XS11 Cross-sectional Profile

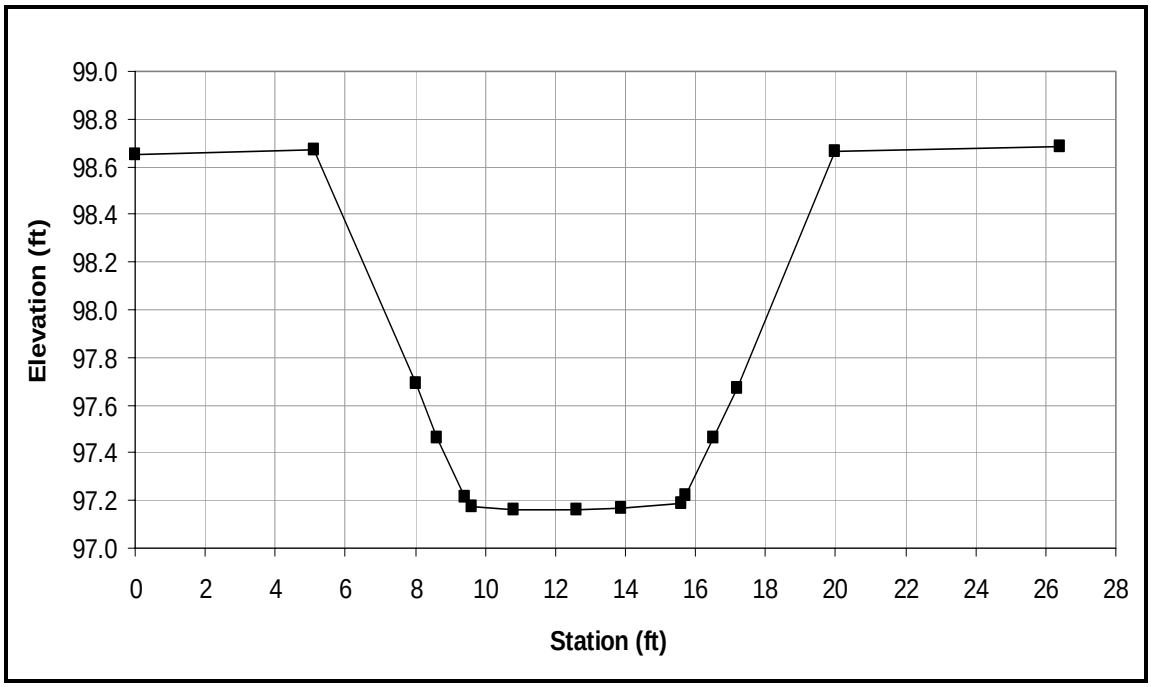

Figure A.13. XS12 Cross-sectional Profile

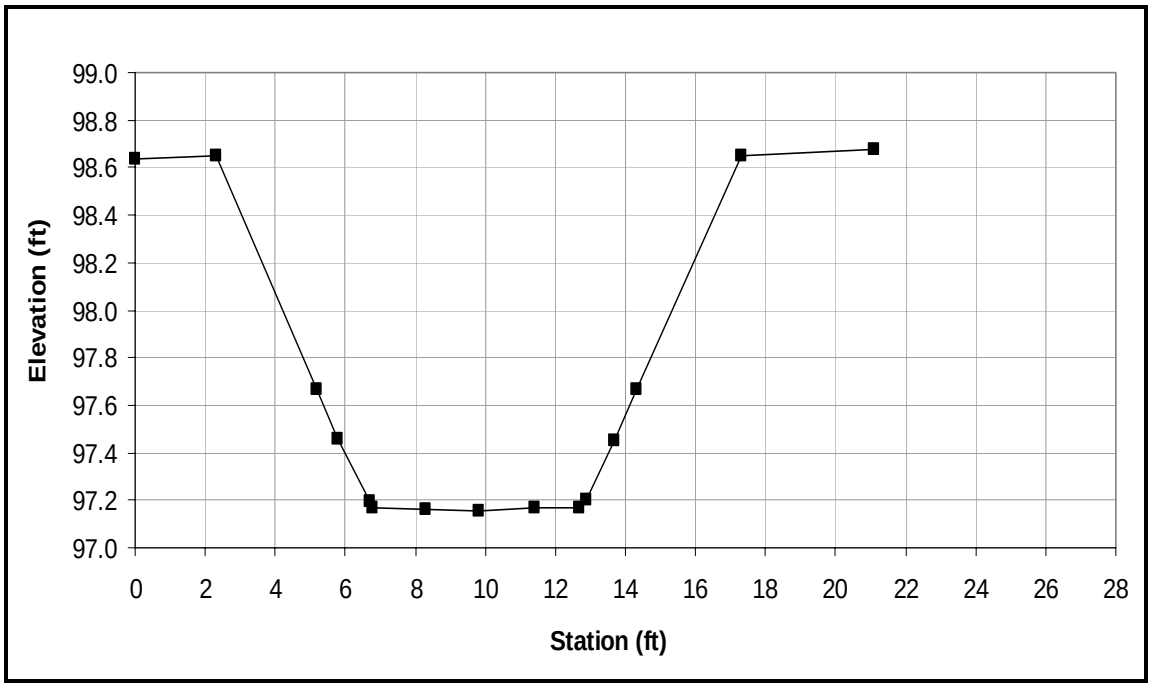

Figure A.14. XS13 Cross-sectional Profile

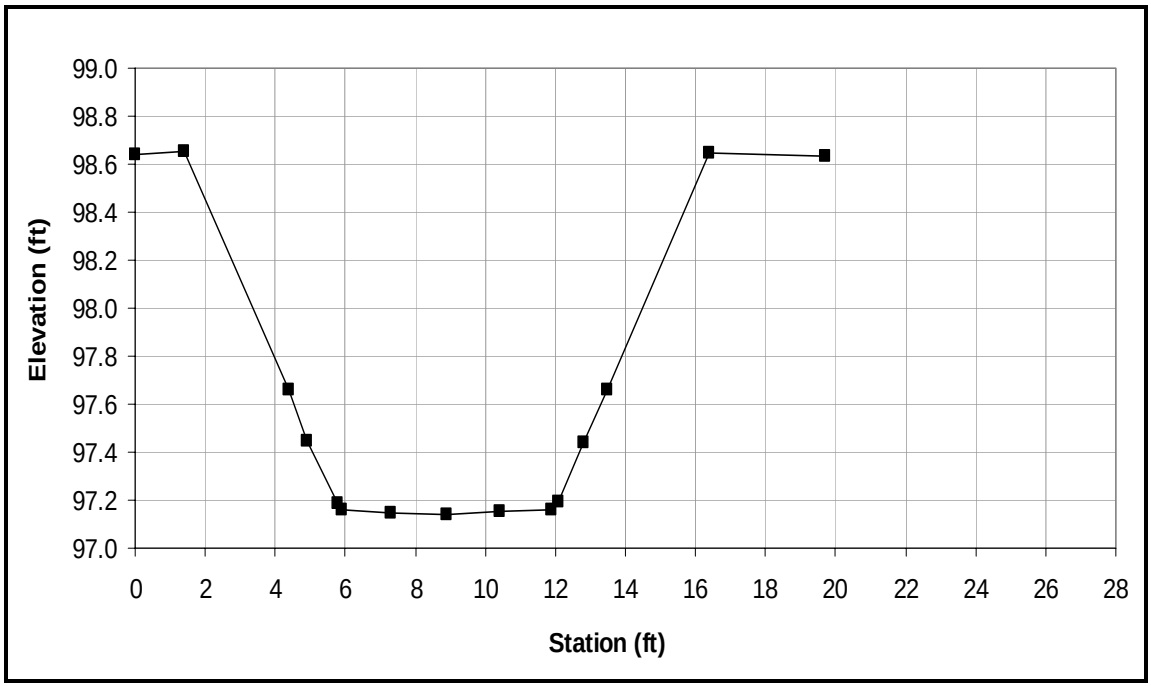

Figure A.15. XS14 Cross-sectional Profile

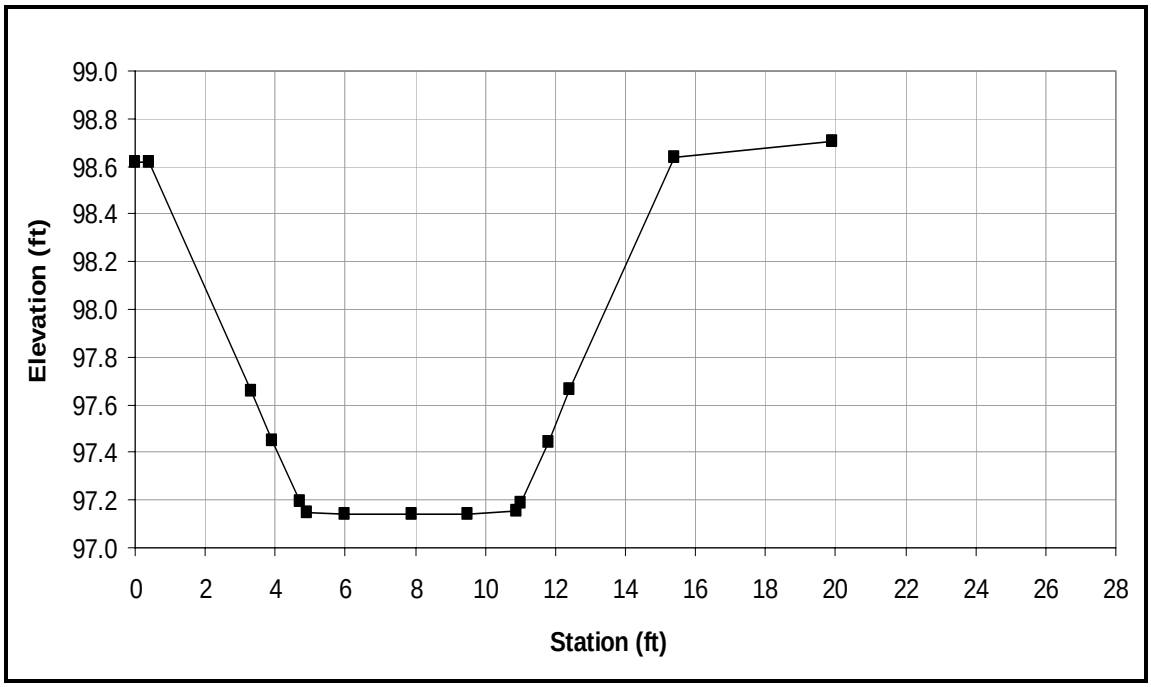

Figure A.16. XS15 Cross-sectional Profile

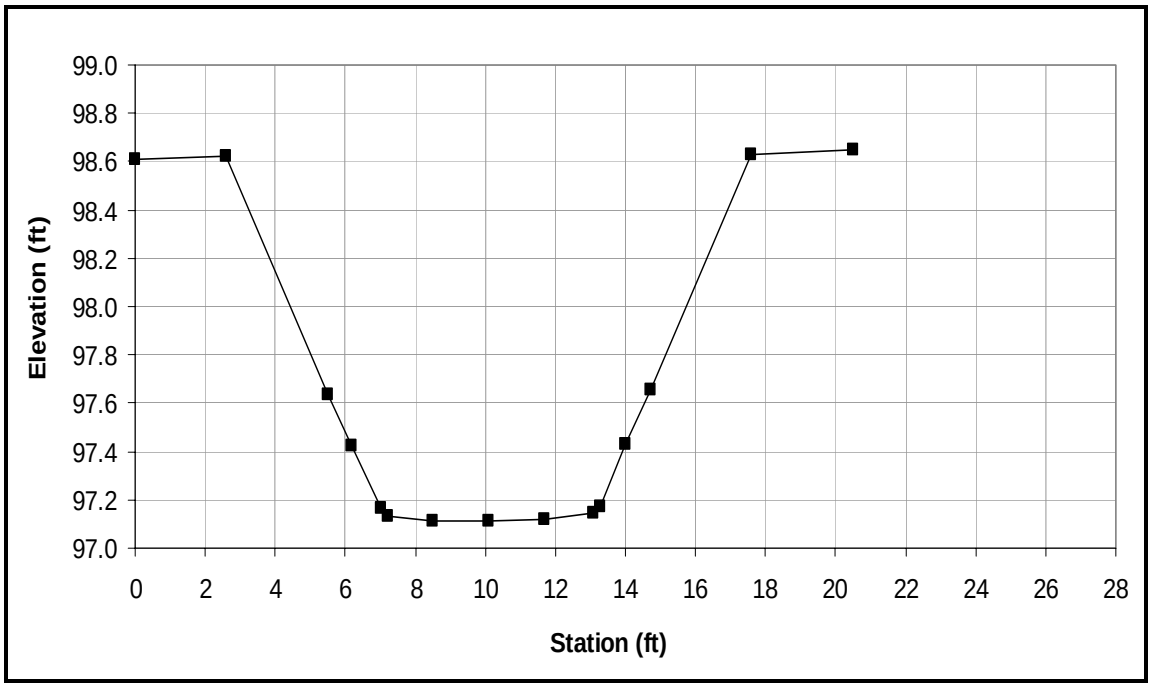

Figure A.17. XS16 Cross-sectional Profile

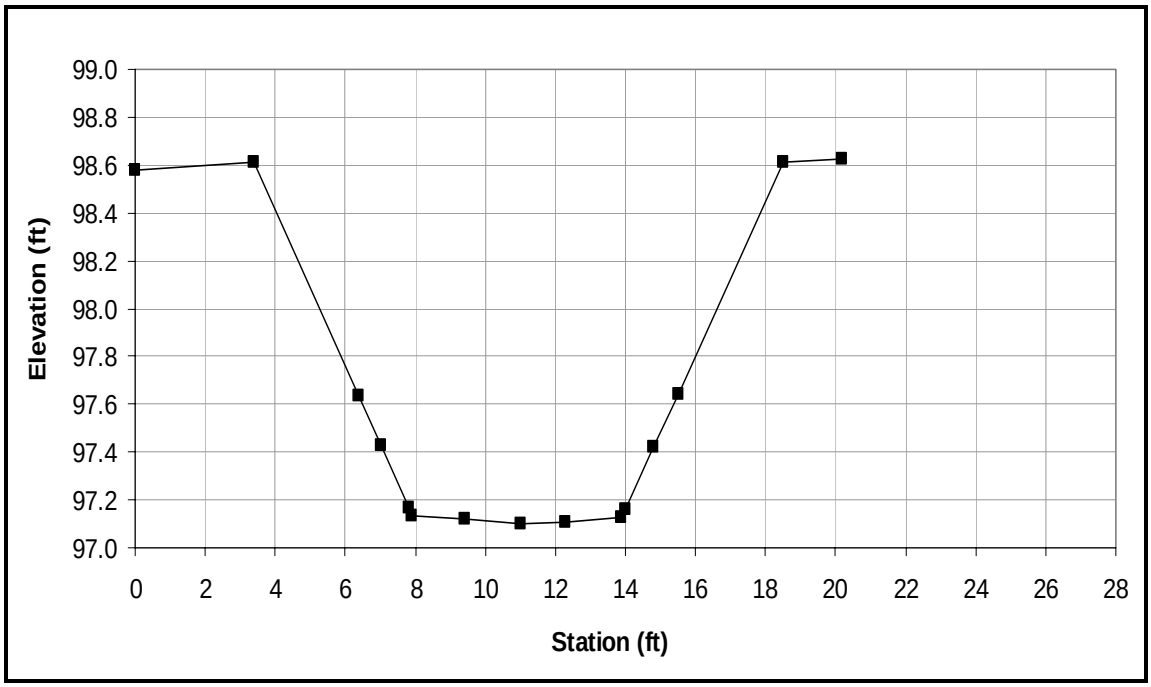

Figure A.18. XS17 Cross-sectional Profile

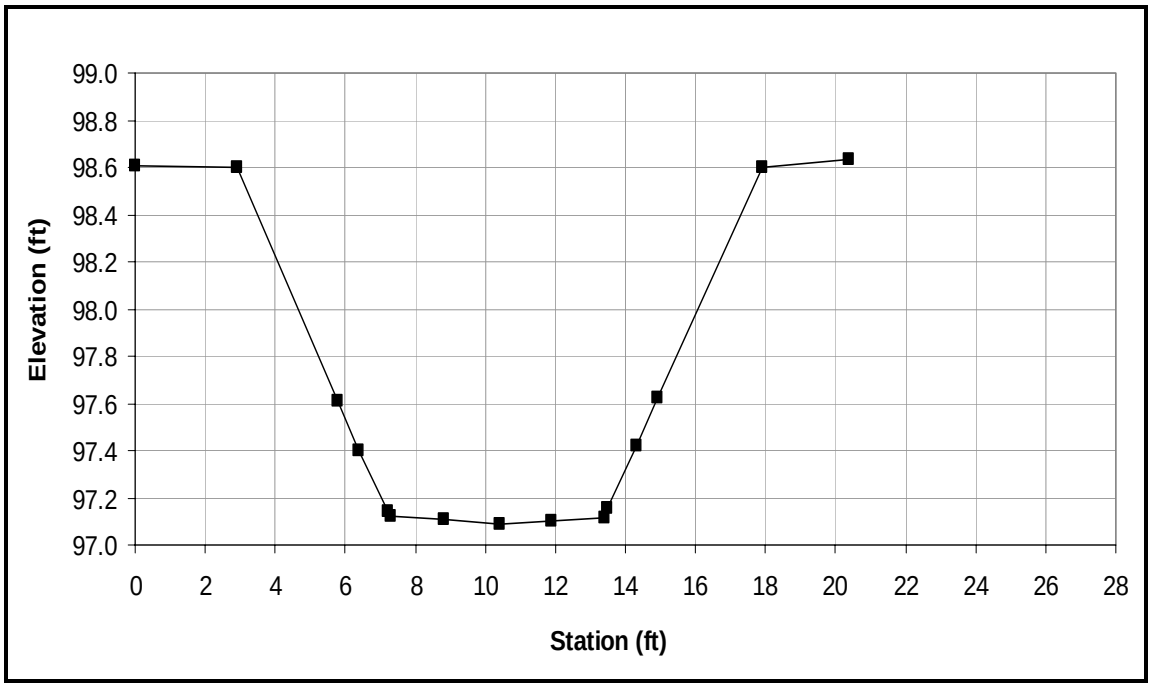

Figure A.19. XS18 Cross-sectional Profile

APPENDIX B

BASE-LINE AND BENDWAY-WEIR TESTING PROGRAM RESULTS

Table B.1. 8-cfs Base-line Data Sheet

	Initials
Point Gage Reader	KK
Recorder	JH

DATE: 2/24/2004

8 cfs WITH STOP LOGS				
Cross Section	**Point**	**Bed Reading**	**Water-surface Reading**	**Point Gage Position Along Cart**
0	D_{CART}	0.396	1.006	18.80
1	D_{CART}	0.397	0.988	16.53
2	D_{CART}	0.338	0.942	17.02
3	D_{CART}	0.337	0.944	15.88
4	D_{CART}	0.346	0.951	16.59
5	D_{CART}	0.373	0.964	17.45
6	D_{CART}	0.376	0.969	17.80
7	D_{CART}	0.354	0.966	15.89
8	D_{CART}	0.348	0.950	16.08
9	D_{CART}	0.320	0.926	15.13
10	D_{CART}	0.307	0.900	14.12
11	D_{CART}	0.320	0.907	14.56
12	D_{CART}	0.331	0.914	16.24
13	D_{CART}	0.311	0.900	19.38
14	D_{CART}	0.295	0.884	19.54
15	D_{CART}	0.292	0.870	19.77
16	D_{CART}	0.230	0.838	17.80
17	D_{CART}	0.208	0.812	17.39
18	D_{CART}	0.945	1.561	39.53

Table B.2. 12-cfs Base-line Data Sheet

	Initials
Point Gage Reader	KEK
Recorder	CW

DATE: 6/3/2004

12 cfs WITH STOP LOGS				
Cross Section	**Point**	**Bed Reading**	**Water-surface Reading**	**Point Gage Position Along Cart**
18	D_{CART}	0.928	1.766	0.838
17	D_{CART}	0.187	1.017	0.830
16	D_{CART}	0.204	1.033	0.829
15	D_{CART}	0.255	1.062	0.807
14	D_{CART}	0.271	1.080	0.809
13	D_{CART}	0.287	1.084	0.797
12	D_{CART}	0.299	1.101	0.802
11	D_{CART}	0.289	1.091	0.802
10	D_{CART}	0.282	1.082	0.800
9	D_{CART}	0.286	1.108	0.822
8	D_{CART}	0.303	1.134	0.831
7	D_{CART}	0.336	1.149	0.813
6	D_{CART}	0.346	1.157	0.811
5	D_{CART}	0.351	1.150	0.799
4	D_{CART}	0.322	1.135	0.813
3	D_{CART}	0.303	1.111	0.808
2	D_{CART}	0.312	1.123	0.811
1	D_{CART}	0.374	1.175	0.801
0	D_{CART}	0.370	1.194	0.824

Δ WS Reading and Bed Reading

Table B.3. 16-cfs Base-line Data Sheet

	Initials
Point Gage Reader	KEK
Recorder	CW

DATE: 6/3/2004

16 cfs WITH STOP LOGS				
Cross Section	**Point**	**Bed Reading**	**Water-surface Reading**	**Point Gage Position Along Cart**
0	D_{CART}	0.372	1.309	0.937
1	D_{CART}	0.368	1.288	0.920
2	D_{CART}	0.312	1.239	0.927
3	D_{CART}	0.307	1.226	0.919
4	D_{CART}	0.327	1.250	0.923
5	D_{CART}	0.350	1.262	0.912
6	D_{CART}	0.344	1.269	0.925
7	D_{CART}	0.331	1.261	0.930
8	D_{CART}	0.310	1.244	0.934
9	D_{CART}	0.286	1.219	0.933
10	D_{CART}	0.283	1.189	0.906
11	D_{CART}	0.291	1.197	0.906
12	D_{CART}	0.303	1.204	0.901
13	D_{CART}	0.282	1.183	0.901
14	D_{CART}	0.267	1.178	0.911
15	D_{CART}	0.262	1.164	0.902
16	D_{CART}	0.204	1.128	0.924
17	D_{CART}	0.190	1.116	0.926
18	D_{CART}	0.935	1.867	0.932

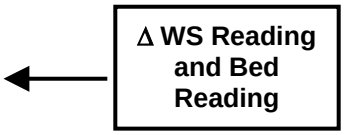

Table B.4. 8-cfs Bendway-weir Testing Data Sheet

Date: 6/10/04
Initials: PS, SG
Discharge (cfs): 8 - mod.
Test ID: test 19

Cross Section Indicated by:	# (1-18)	Piezo Letter (A-G)	0.5b, 0.25b, toe
Weir Indicated by:	W#U or W#C or W#D	LB or RB or TIP	0.5ft, 1.5ft (US Bend)
Position Between Weirs Indicated by:	W# / W#	LB or RB	0.3ft, 0.9ft (DS Bend)

Velocity File Name	Mark #	XS #/ Weir #	Pizo / Weir Pos	Between Weir Point	Percent Depth (%)	Total Depth
test 19a1	1	W1 U			60	0.768
	3	W1 C	weir			0.733
	5	W1 C	tip			0.734
	7	W1 C	RB			0.707
	9	XS1	E			0.645
	11	XS1	D		→	0.705
	13	XS1	C			0.654
	15	W1 D				0.689
	17	W1/W2	RB			0.647
	19	W1/W2	LB			0.664
	21	XS2	D		→	0.700
	23	XS2	C			0.660
	25	XS2	E			0.658
	27	W2 U	LB			0.689
test 19a2	1	W2 C	weir			0.726
	3	W2 C	tip			0.736
	5	W2 C	RB			0.708
	7	W2 D	LB			0.713
	9	XS3	C			0.668
	11	XS3	D		→	0.698
	13	XS3	E			0.654
	15	W2/W3	RD			0.691
	17	W2/W3	LB			0.673
	19	W3 U				0.685
	21	W3 C	RB			0.677

Table B.4. (Continue)

Date: _____
Initials: _____
Discharge (cfs): _____
Test ID: _____

Cross Section Indicated by: # (1-18) Piezo Letter (A-G) 0.5b, 0.25b, toe
Weir Indicated by: W#U or W#C or W#D LB or RB or TIP 0.5ft, 1.5ft (US Bend)
Position Between Weirs Indicated by: W# / W# LB or RB 0.3ft, 0.9ft (DS Bend)

Velocity File Name	Mark #	XS #/ Weir #	Pizo / Weir Pos	Between Weir Point	Percent Depth (%)	Total Depth
	23	W3 C	weir		60	0.693
XS4 C	25	W3 C	tip			0.693
blocked	27	XS 4	D			0.705
	29	XS 4	E			0.641
	31	W3 D				0.752
	33	W3/W4	LB			0.714
	35	W3/W4	RB			0.670
	37	XS 5	E			0.626
	39	XS 5	D			0.689
	41	XS 5	C			0.655
	43	W4 U				0.694
	45	W4 C	RB			0.672
	47	W4 C	weir			0.715
	49	W4 C	tip			0.715
	51	W4 D				0.685
	53	XS 6	D			0.696
	55	XS 6	E			0.619
	57	XS 6	C			0.666
	59	W4/W5	LB			0.660
	61	W4/W5	RB			0.675
	63	W5 U				0.689
XS7C	65	XS 7	D			0.687
blocked	67	XS 7	E			0.633
	69	W5 C	RB			0.657
	71	W5 C	weir			0.698

Table B.4. (Continue)

Date: 6/11/04
Initials: SG PS
Discharge (cfs): 8
Test ID: Test 19

Cross Section Indicated by: # (1-18) | Piezo Letter (A-G) | 0.5b, 0.25b, toe
Weir Indicated by: W#U or W#C or W#D | LB or RB or TIP | 0.5ft, 1.5ft (US Bend)
Position Between Weirs Indicated by: W# / W# | LB or RB | 0.3ft, 0.9ft (DS Bend)

Velocity File Name	Mark #	XS # / Weir #	Pizo / Weir Pos	Between Weir Point	Percent Depth (%)	Total depth
test19a2 (cont.)	73	WSC	tip		60	0.698
	75	WS D				0.687
	77	XS 8	D			0.686
	79	XS 8	E			0.615
	81	XS 8	C			0.634
	83	XS 9	D			0.640
	85	XS 10	C			~~0.714~~ 0.636
	87	XS 10	D			0.699
	89	XS 10	E			0.642
	91	XS 11	E			0.646
	93	XS 11	D			0.698
	95	XS 11	C			0.640
	97	WGU				0.673
	99	WG C	weir			0.616
	101	WG C	tip			0.616
	103	WG C	LB			0.614
	105	WG D				0.604
	107	XS 12	E			0.564
	109	XS 12	D			0.610
	111	XS 12	C			0.559
	113	W6/W7	LB			0.586
	115	W6/W7	RB			0.612
	117	XS 13	E			0.569
	119	XS 13	D			0.632
	121	XS 13	C			0.576

Table B.4. (Continue)

Date: _____
Initials: _____
Discharge (cfs): _____
Test ID: _____

	Cross Section Indicated by:	# (1-18)	Piezo Letter (A-G)	0.5b, 0.25b, toe		
	Weir Indicated by:	W#U or W#C or W#D	LB or RB or TIP	0.5ft, 1.5ft (US Bend)		
	Position Between Weirs Indicated by:	W# / W#	LB or RB	0.3ft, 0.9ft (DS Bend)		

Velocity File Name	Mark #	XS #/ Weir #	Pizo / Weir Pos	Between Weir Point	Percent Depth (%)	Total depth
	123	W7 U			60	0.668
	125	W7 C	weir			0.588
XS 14	127	W7 C	tip			0.588
= blocked	129	W7 C	LB			0.604
	131	XS 14	C			0.564
	133	XS 14	D		→	0.605
	135	W7 D				0.565
	137	XS 15	D		→	0.594
	139	XS 15	E			0.526
	141	XS 15	C			0.544
	143	W7/W8	LB			0.575
	145	W7/W8	RB			0.577
	147	XS 16	E			0.595
	149	XS 16	D		→	0.632
	151	XS 16	C			0.570
	153	W8 U				0.630
	155	W8 C	weir			0.588
	157	W8 C	tip			0.588
	159	W8 C	LB			0.598
	161	W8 D				0.558
	163	XS 17	E			0.513
	165	XS 17	D		→	0.570
	167	XS 17	C			0.512

Table B.5. 12-cfs Bendway-weir Testing Data Sheet

Date: 6/15/04
Initials: PS, SG, AC
Discharge (cfs): 12
Test ID: test 19

ADV

Cross Section Indicated by: # (1-18) Piezo Letter (A-G) 0.5b, 0.25b, toe
Weir Indicated by: W#U or W#C or W#D LB or RB or TIP 0.5ft, 1.5ft (US Bend)
Position Between Weirs Indicated by: W# / W# LB or RB 0.3ft, 0.9ft (DS Bend)

Velocity File Name	Mark #	XS #/ Weir #	Pizo / Weir Pos	Between Weir Point	Percent Depth (%)	Total Depth
test1961	1	W1 U			60	0.940
	3	W1 C	weir			0.933
	5	W1 C	tip			0.935
	7	W1 C	RB			0.902
	9	XS1	E			0.840
	11	XS1	D			0.890
	13	XS1	C			0.828
	15	W1 D				0.868
	17	W1/W2	RB			0.853
	19	W1/W2	LB			0.862
	21	XS2	C			0.857
	23	XS2	D			0.905
	25	XS2	E			0.856
	27	W2 U				0.888
	29	W2 C	weir			0.97
	31	W2 C	tip			0.920
	33	W2 C	RB			0.891
	35	W2 D				0.905
	37	XS3	C			0.848
	39	XS3	D			0.886
	41	XS3	E			0.835
	43	W2/W3	RB			0.867
	45	W2/W3	LB			0.858
	47	W3 U				0.86
	49	W3 C	weir			0.88

Table B.5. (Continue)

Date: 06/15/04
Initials: AC, PS
Discharge (cfs): 12
Test ID: TEST 19

ADV

Cross Section Indicated by:	# (1-18)	Piezo Letter (A-G)	0.5b, 0.25b, toe
Weir Indicated by:	W#U or W#C or W#D	LB or RB or TIP	0.5ft, 1.5ft (US Bend)
Position Between Weirs Indicated by:	W# / W#	LB or RB	0.3ft, 0.9ft (DS Bend)

Velocity File Name	Mark #	XS # / Weir #	Pizo / Weir Pos	Between Weir Point	Percent Depth (%)	Total depth
TEST19b1	51	W3 C	TIP		60	0.88
	53	W3 C	RB			0.86
X4 C BLOCKED*	55	XS 4	D			0.892
	57	XS 4	E			0.816
	59	W3 DS				0.941
	61	W3/W4	LB			0.889
	63	W3/W4	RB			0.853
	65	XS 5	E			0.804
	67	XS 5	D			0.886
	69	XS 5	C			0.847
	71	W4	U			0.879
	73	W4 C	weir			0.915
	75		tip			0.915
	77		RB			0.861
	79	W4 DS				0.882
	81	XS 6	C			0.84
	83	XS 6	D			0.887
	85	XS 6	E			0.805
	87	W4/W5	RB			0.863
	89	W4/W5	LB			0.853
	91	W5 U				0.885
* XS 7C BLOCKED*	93	XS 7	D			0.901
	95	XS 7	E			0.827
	97	W5 C	RB			0.871
	99	W5 C	weir			0.912

Table B.5. (Continue)

Date: 06/15/04
Initials: AC, PS
Discharge (cfs): 12
Test ID: Test 19

Cross Section Indicated by: # (1-18) Piezo Letter (A-G) 0.5b, 0.25b, toe
Weir Indicated by: W#U or W#C or W#D LB or RB or TIP 0.5ft, 1.5ft (US Bend)
Position Between Weirs Indicated by: W# / W# LB or RB 0.3ft, 0.9ft (DS Bend)

Velocity File Name	Mark #	XS # / Weir #	Pizo / Weir Pos	Between Weir Point	Percent Depth (%)	Total depth
Test1961	101	WS C	~~main~~ tip		60%	0.912
	103	WS ds				0.899
	105	XS 8	d			0.889
	107	XS 8	E			0.839
	109	XS 8	C			0.852
	111	~~XS 8~~	~~WR~~			
	113					
	115					
	117					
	119					
	121					
	123					
	125					
	127					
	129					
	131					
	133					
	135					
	137					
	139					
	141					
	143					
	145					
	147					
	149					

Table B.5. (Continue)

Date: 06/16/04
Initials: AC, PS
Discharge (cfs): 12
Test ID: test19

ADV

Cross Section Indicated by:	# (1-18)	Piezo Letter (A-G)	0.5b, 0.25b, toe
Weir Indicated by:	W#U or W#C or W#D	LB or RB or TIP	0.5ft, 1.5ft (US Bend)
Position Between Weirs Indicated by:	W# / W#	LB or RB	0.3ft, 0.9ft (DS Bend)

Velocity File Name	Mark #	XS #/ Weir #	Pizo / Weir Pos	Between Weir Point	Percent Depth (%)	Total Depth
test19b2 ignore	1	XS 9D			60%	0.92
	3	XS 9D				0.92
	5	XS 10	C			0.886
	7	XS 10	D			0.914
	9	XS 10	E			0.86
	11	XS 11	E			0.865
	13	XS 11	D			0.912
	15	XS 11	C			0.862
	17	W6 U				0.848
	19	W6 C	weir			0.849
	21	W6 C	tip			0.849
	23	W6 C	LB			0.793
	25	W6 DS				0.82
	27	XS 12	E			0.784
	29	XS 12	D			0.82
	31	XS 12	C			0.791
	33	W6/W7	LB			0.814
	35	W6/W7	RB			0.825
	37	XS 13	E			0.806
	39	XS 13	D			0.858
	41	XS 13	C			0.808
	43	W7 U				0.884
	45	W7 C	weir			0.832
	47	W7 C	tip			0.832
	49	W7 C	LB			0.815

Table B.5. (Continue)

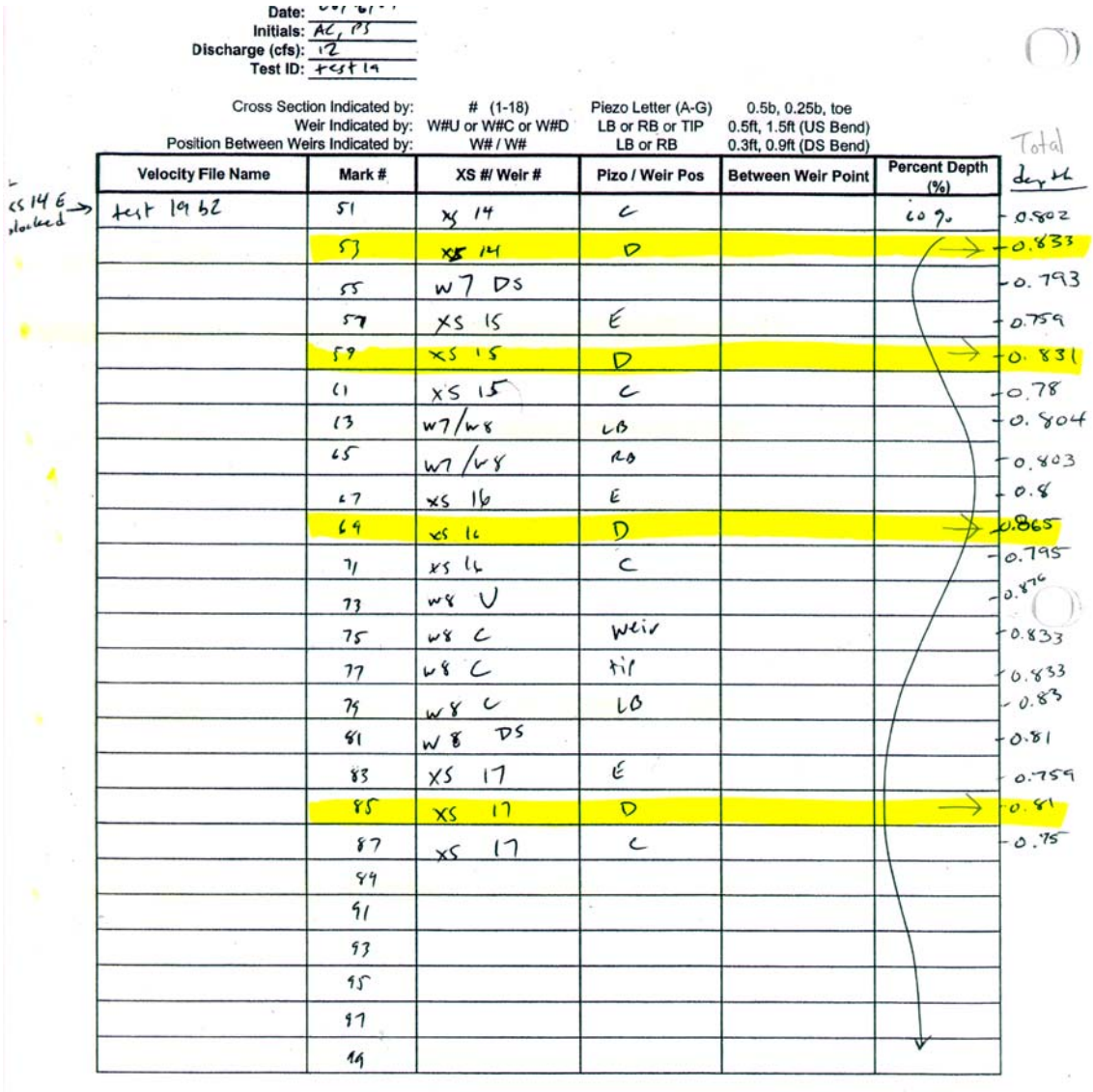

Date:
Initials: AC, PS
Discharge (cfs): 12
Test ID: test 19

Cross Section Indicated by: # (1-18) Piezo Letter (A-G) 0.5b, 0.25b, toe
Weir Indicated by: W#U or W#C or W#D LB or RB or TIP 0.5ft, 1.5ft (US Bend)
Position Between Weirs Indicated by: W# / W# LB or RB 0.3ft, 0.9ft (DS Bend)

Velocity File Name	Mark #	XS #/ Weir #	Pizo / Weir Pos	Between Weir Point	Percent Depth (%)	Total depth
XS 14 E blocked → test 19 b2	51	XS 14	C		60 %	0.802
	53	XS 14	D		→	0.833
	55	W7 DS				0.793
	57	XS 15	E			0.759
	59	XS 15	D		→	0.831
	61	XS 15	C			0.78
	63	W7/W8	LB			0.804
	65	W7/W8	RB			0.803
	67	XS 16	E			0.8
	69	XS 16	D		→	0.865
	71	XS 16	C			0.795
	73	W8 U				0.876
	75	W8 C	Weir			0.833
	77	W8 C	Tip			0.833
	79	W8 C	LB			0.83
	81	W8 DS				0.81
	83	XS 17	E			0.759
	85	XS 17	D		→	0.81
	87	XS 17	C			0.75
	89					
	91					
	93					
	95					
	97					
	99					

Table B.6. 16-cfs Bendway-weir Test Data Sheet

Date: 6/21/2004
Testers: PS,AC
Discharge (cfs): 16 - modified
Test ID: test19c2

Point #	Theoretical Flowrate	Spacing Ratio	% Depth	Total Depth	XSEC	Piezo	Weir #	Weir Pos.	Bank Pos.	% Top Width	Theta	Notes:
1	16	4.1	60	1.017			5	center	weir	28	75	
3	16	4.1	60	1.017			5	center	tip	28	75	
5	16	4.1	60	0.974			5	center	inner	28	75	
7	16	4.1	60	1.021			5	ds	outer	28	75	
9	16	4.1	60	0.691	8	c				28	75	
11	16	4.1	60	0.999	8	d				28	75	
13	16	4.1	60	0.946	8	e				28	75	
15	16		60	1.021	9	d				28	75	
17	16	7.62	60	0.965	10	e				28	75	
19	16	7.62	60	1.007	10	d				28	75	
21	16	7.62	60	0.955	10	c				28	75	
23	16	7.62	60	0.946	11	c				28	75	
25	16	7.62	60	1.01	11	d				28	75	
27	16	7.62	60	0.967	11	e				28	75	
29	16	7.62	60	0.995			6	us	outer	28	75	
31	16	7.62	60	0.913			6	center	weir	28	75	
33	16	7.62	60	0.913			6	center	tip	28	75	
35	16	7.62	60	0.933			6	center	inner	28	75	
37	16	7.62	60	0.894			6	ds	outer	28	75	
39	16	7.62	60	0.859	12	e				28	75	
41	16	7.62	60	0.91	12	d				28	75	
43	16	7.62	60	0.866	12	c				28	75	
45	16	7.62	60	0.91			b6/7	between	inner	28	75	
47	16	7.62	60	0.927			b6/7	between	outer	28	75	
49	16	7.62	60	0.882	13	e				28	75	
51	16	7.62	60	0.93	13	d				28	75	
53	16	7.62	60	0.877	13	c				28	75	
55	16	7.62	60	0.955			7	us	outer	28	75	
57	16	7.62	60	0.88			7	center	weir	28	75	
59	16	7.62	60	0.88			7	center	tip	28	75	
61	16	7.62	60	0.89			7	center	inner	28	75	
63	16	7.62	60	0.861	14	c				28	75	XSEC 14 e blocked by weir
65	16	7.62	60	0.899	14	d				28	75	
67	16	7.62	60	0.852			7	ds	outer	28	75	
69	16	7.62	60	0.845	15	e				28	75	
71	16	7.62	60	0.891	15	d				28	75	
73	16	7.62	60	0.836	15	c				28	75	
75	16	7.62	60	0.867			b7/8		inner	28	75	
77	16	7.62	60	0.883			b7/8		outer	28	75	
79	16	7.62	60	0.878	16	e				28	75	
81	16	7.62	60	0.899	16	d				28	75	
83	16	7.62	60	0.837	16	c				28	75	
85	16	7.62	60	0.934			8	us	outer	28	75	
87	16	7.62	60	0.865			8	center	weir	28	75	
89	16	7.62	60	0.865			8	center	tip	28	75	
91	16	7.62	60	0.89			8	center	inner	28	75	
93	16	7.62	60	0.864			8	ds	outer	28	75	
95	16	7.62	60	0.819	17	e				28	75	
97	16	7.62	60	0.884	17	d				28	75	
99	16	7.62	60	0.791	17	c				28	75	

Table B.6. (Continue)

Date: 6/18/2004
Testers: PS, AC
Discharge (cfs): 16 - modified
Test ID: test19c1

Point #	Theoretical Flowrate	Spacing Ratio	% Depth	Total Depth	XSEC	Piezo	Weir #	Weir Pos.	Bank Pos.	% Top Width	Theta	Notes:
1	16	4.1	60	1.08			1	us	outer	28	75	
3	16	4.1	60	1.03			1	center	inner	28	75	
5	16	4.1	60	1.052			1	center	weir	28	75	
7	16	4.1	60	1.057			1	center	tip	28	75	
9	16	4.1	60	1.008	1	d				28	75	
11	16	4.1	60	0.931	1	c				28	75	
13	16	4.1	60	0.945	1	e				28	75	
15	16	4.1	60	0.981			1	ds	outer	28	75	
17	16	4.1	60	0.989			b1/2	between	outer	28	75	
19	16	4.1	60	0.959			b1/2	between	inner	28	75	
21	16	4.1	60	0.968	2	e				28	75	
23	16	4.1	60	1.02	2	d				28	75	
25	16	4.1	60	0.966	2	c				28	75	
27	16	4.1	60	1.001			2	us	outer	28	75	
29	16	4.1	60	1.009			2	center	inner	28	75	
31	16	4.1	60	1.022			2	center	weir	28	75	
33	16	4.1	60	1.023			2	center	tip	28	75	
35	16	4.1	60	1.016			2	ds	outer	28	75	
37	16	4.1	60	0.86	3	e				28	75	
39	16	4.1	60	1	3	d				28	75	
41	16	4.1	60	0.969	3	c				28	75	
43	16	4.1	60	0.976			b2/3	between	outer	28	75	
45	16	4.1	60	0.995			b2/3	between	inner	28	75	
47	16	4.1	60	0.986			3	us	outer	28	75	
49	16	4.1	60	0.986			3	center	weir	28	75	
51	16	4.1	60	0.99			3	center	tip	28	75	
53	16	4.1	60	0.974			3	center	inner	28	75	
55	16	4.1	60	1.015	4	d				28	75	xsec 4 c blocked by weir
57	16	4.1	60	0.941	4	e				28	75	
59	16	4.1	60	1.065			3	ds	outer	28	75	
61	16	4.1	60	0.991			b3/4	between	outer	28	75	
63	16	4.1	60	0.958			b3/4	between	inner	28	75	
65	16	4.1	60	0.91	5	e				28	75	
67	16	4.1	60	0.995	5	d				28	75	
69	16	4.1	60	0.945	5	c				28	75	
71	16	4.1	60	0.93			4	us	outer	28	75	
73	16	4.1	60	1.014			4	center	weir	28	75	
75	16	4.1	60	1.016			4	center	tip	28	75	
77	16	4.1	60	0.961			4	center	inner	28	75	
79	16	4.1	60	0.884			4	ds		28	75	
81	16	4.1	60	0.958	6	c				28	75	
83	16	4.1	60	1.01	6	d				28	75	
85	16	4.1	60	0.916	6	e				28	75	
87	16	4.1	60	0.98			b4/5	between	inner	28	75	
89	16	4.1	60	0.972			b4/5	between	outer	28	75	
91	16	4.1	60	1.005			5	us	outer	28	75	
93	16	4.1	60	1.012	7	d				28	75	xsec 7 c blocked by weir
95	16	4.1	60	0.936	7	e				28	75	

APPENDIX C

LINEAR INTERPOLATION OF TOTAL ENERGY LOSS AT 12 CFS AND 16 CFS

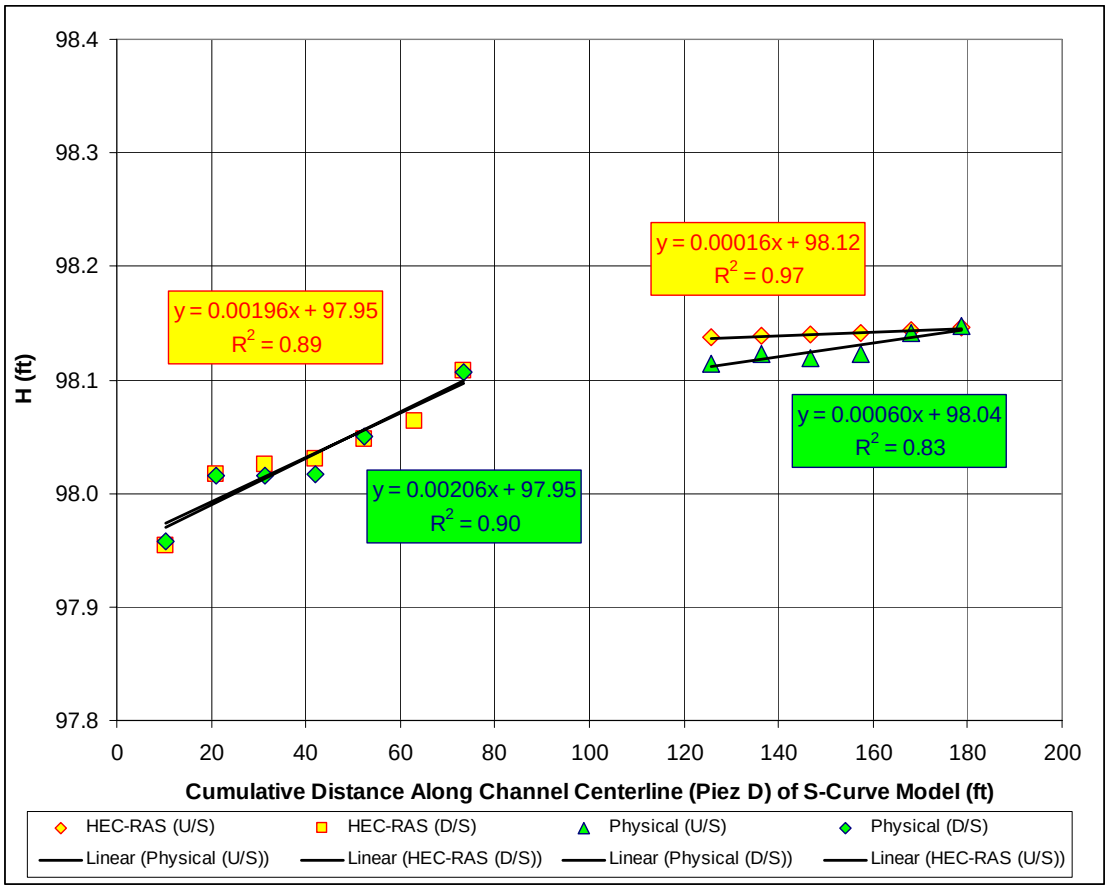

Figure C.1. Linear Interpolation at 12 cfs

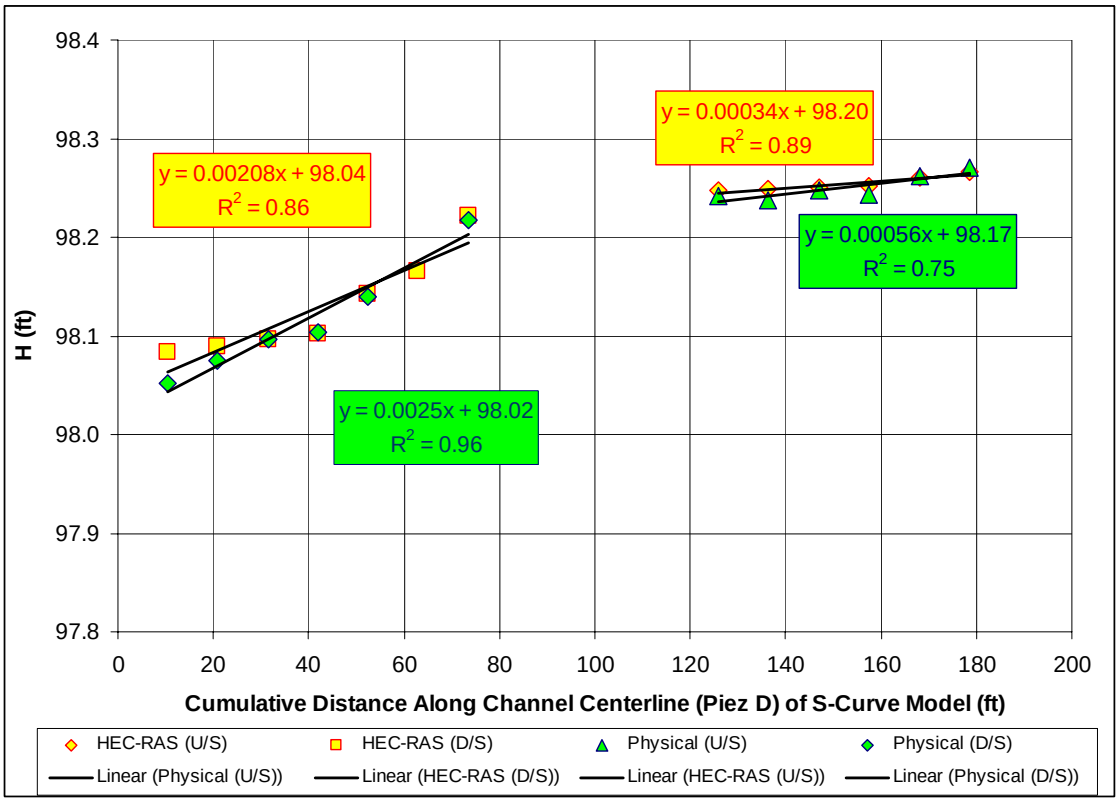

Figure C.2. Linear Interpolation at 16 cfs

APPENDIX D

ACCURACY OF π_5 PREDICTOR EQUATION

1. Plot observed $\bar{h}_{BEND}/\bar{h}_{Sf}$ vs. π_5.

Table D.1. Data Required to Estimate Trend Line

Q (cfs)	Bend	$\bar{h}_{BEND}/\bar{h}_{Sf}$	π_5
8	Type I	1.23	2.80
8	Type III	0.18	6.87
12	Type I	1.12	2.56
12	Type III	0.24	6.03
16	Type I	1.34	2.45
16	Type III	0.32	5.71

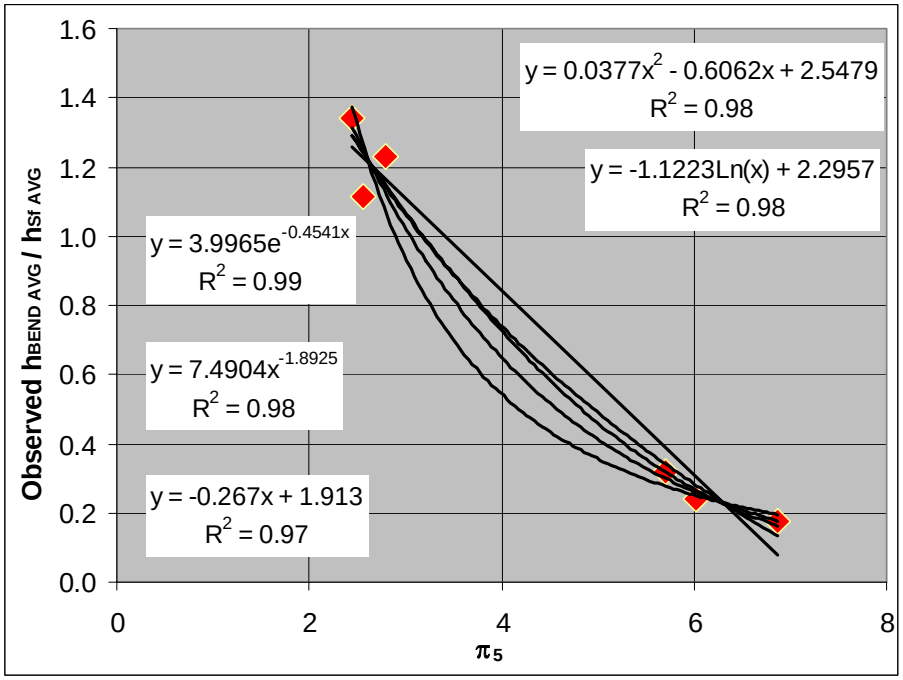

Figure D.1. Observed Trend Lines

2. Determine a trend line that interpolates a significant relationship between $\bar{h}_{BEND}/\bar{h}_{Sf}$ vs. π_5.

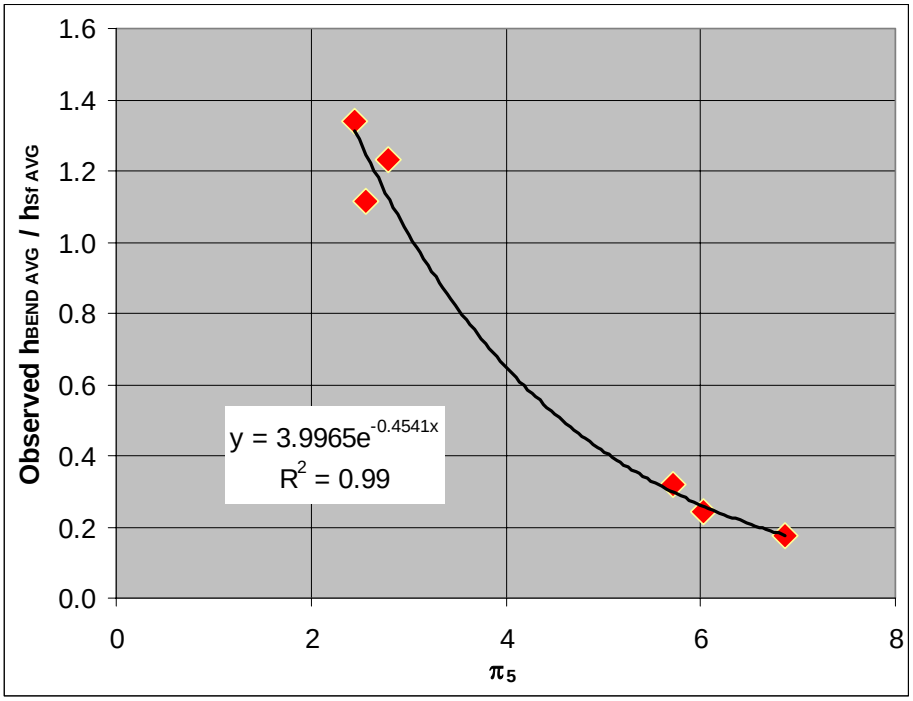

Figure D.2. Trend Line with Significant Relationship

3. Use equation defining interpolated trend line to calculate predicted $\bar{h}_{BEND}/\bar{h}_{Sf}$.

Predictor Equation for π_5

$$y = 3.9965e^{-0.4541x}$$

where:

$y = \bar{h}_{BEND}/\bar{h}_{Sf}$; and

$x = \pi_5$.

Table D.2. Predicted $\bar{h}_{BEND}/\bar{h}_{Sf}$ Results

Q (cfs)	Bend	$\bar{h}_{BEND}/\bar{h}_{Sf}$	π_5	Predicted $\bar{h}_{BEND}/\bar{h}_{Sf}$
8	Type I	1.23	2.80	1.12
8	Type III	0.18	6.87	0.18
12	Type I	1.12	2.56	1.25
12	Type III	0.24	6.03	0.26
16	Type I	1.34	2.45	1.31
16	Type III	0.32	5.71	0.30

4. Calculate percent error and absolute percent error between predicted $\bar{h}_{BEND}/\bar{h}_{Sf}$ and observed $\bar{h}_{BEND}/\bar{h}_{Sf}$.

Table D.3. Percent Error and Absolute Percent Error Results

Q (cfs)	Bend	$\bar{h}_{BEND}/\bar{h}_{Sf}$	π_5	Predicted $\bar{h}_{BEND}/\bar{h}_{Sf}$	Percent Error (%)	Abs. Percent Error (%)
8	Type I	1.23	2.80	1.12	-8.83	8.83
8	Type III	0.18	6.87	0.18	0.09	0.09
12	Type I	1.12	2.56	1.25	11.84	11.84
12	Type III	0.24	6.03	0.26	6.55	6.55
16	Type I	1.34	2.45	1.31	-1.86	1.86
16	Type III	0.32	5.71	0.30	-6.20	6.20
				Average Error	0.26	5.90

5. Plot observed $\bar{h}_{BEND}/\bar{h}_{Sf}$ and predicted $\bar{h}_{BEND}/\bar{h}_{Sf}$ to observe linear relationship.

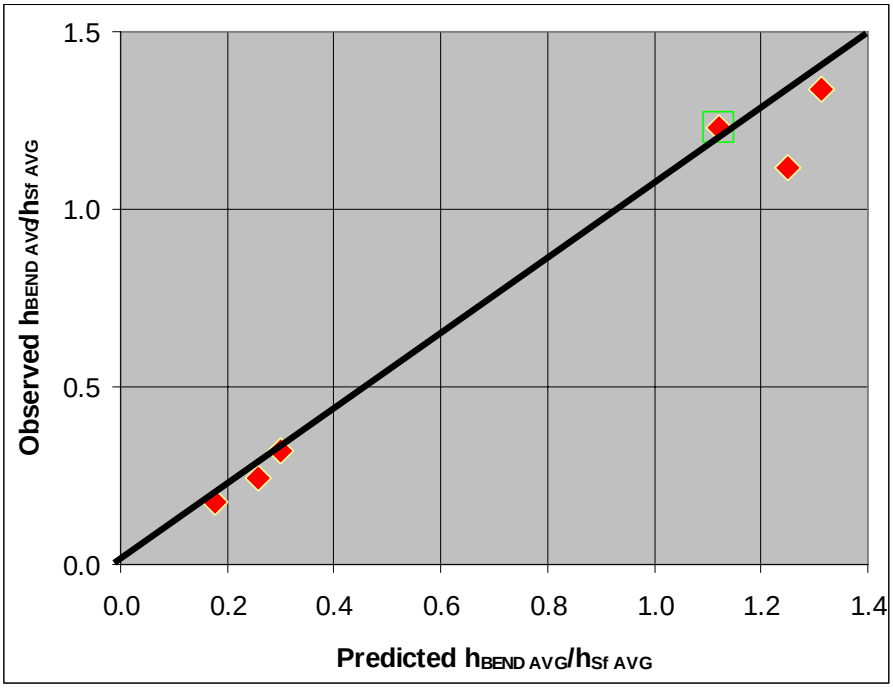

Figure D.3. Observed Linear Relationship